Titre: Title:	Polariton Nonlinearities in High Exciton Binding Energy Semiconductors
Auteur: Author:	Louis Haeberlé
Date:	2025
Type:	Mémoire ou thèse / Dissertation or Thesis
Référence: Citation:	Haeberlé, L. (2025). Polariton Nonlinearities in High Exciton Binding Energy Semiconductors [Thèse de doctorat, Polytechnique Montréal]. PolyPublie. https://publications.polymtl.ca/70615/

POLYTECHNIQUE MONTRÉAL
affiliée à l'Université de Montréal

Polariton nonlinearities in high exciton binding energy semiconductors

LOUIS HAEBERLÉ
Département de génie physique

Thèse présentée en vue de l'obtention du diplôme de *Philosophiæ Doctor*
Génie physique

Novembre 2025

POLYTECHNIQUE MONTRÉAL
affiliée à l'Université de Montréal

Cette thèse intitulée :

Polariton nonlinearities in high exciton binding energy semiconductors

présentée par **Louis HAEBERLÉ**
en vue de l'obtention du diplôme de *Philosophiæ Doctor*
a été dûment acceptée par le jury d'examen constitué de :

Sébastien FRANCOEUR, président
Stéphane KÉNA-COHEN, membre et directeur de recherche
Sébastien LORANGER, membre
Philippe ST-JEAN, membre externe

DEDICATION

To my parents, Albéric and Viviane.

ACKNOWLEDGEMENTS

First and foremost, I wish to thank my advisor Dr. Stéphane Kéna-Cohen for his advice, support and encouragement throughout the project. I learned a lot during my time in the Light-Matter Group, because he offered me many opportunities to collaborate on projects touching a variety of fields ranging from organic semiconductors to strained photonic crystals. Most of it didn't end up in this dissertation, but the experience of learning new experimental techniques and applying them to different materials and structures was invaluable.

I also want to express my gratitude towards Dr. Michael S. Arnold and his group at the University of Wisconsin-Madison, and particularly Dr. Abitha Dhavamani who worked tirelessly to improve the quality of the samples throughout the entire project. She consistently went above and beyond to deliver us better thin films and microcavities up until the very last week before her thesis defence. My project could not have moved forward without her numerous contributions, and she taught me much about materials science.

I am thankful to all of the members of the Light-Matter Group, and I especially want to mention Julien Brodeur, Tomohiro Ishii, Alexandre Malinge, Pierre-Luc Thériault and Félix Thouin both for their help in the lab, and for the many spirited discussions we had in the office after hours. I am also grateful to Julien for introducing me to rock climbing, along with Isabelle Largillière.

My friends Guillaume Allain and Jeck Borne offered key advice on optical system design and numerical modelling respectively.

Finally, I wish to thank my parents Albéric and Viviane as well as my wife Chloé for their continued moral and material support; I couldn't have done it without you.

RÉSUMÉ

Les exciton-polaritons sont des quasiparticules hybrides possédant à la fois des propriétés associées à la lumière et à la matière. Ils sont formés dans les microcavités optiques contenant un matériau semiconducteur, lorsque l'échange cohérent d'énergie entre le matériau et le mode de cavité surpasse les pertes intrinsèques de ceux-ci. Cette condition définit le régime de fort couplage lumière-matière, observable par une modification importante du spectre d'absorption dû à l'émergence des polaritons comme nouveaux états propres du système couplé. Les propriétés uniques des polaritons (entre autres, leur caractère bosonique, leur faible masse effective, et leurs interactions nonlinéaires) en font un système particulièrement intéressant à la fois pour la recherche fondamentale sur l'interaction lumière-matière et l'optique quantique, et pour le développement de nouveaux dispositifs photoniques. Une importante application potentielle est l'utilisation de condensats de polaritons comme source de lumière cohérente avec un seuil d'émission beaucoup plus bas qu'un laser conventionnel.

Dans ce travail, nous nous concentrons sur les polaritons utilisant des matériaux semiconducteurs à haute énergie de liaison excitonique : les nanotubes de carbone et les perovskites inorganiques. Ceux-ci possèdent des propriétés avantageuses pour le couplage fort lumière-matière, car leurs excitons sont stables à température ambiante et ont une grande force d'oscillateur et une longue durée de vie. De plus, ils peuvent être fabriqués par des méthodes de traitement en solution plutôt que par la croissance de couche minces sous ultravide.

Nous utilisons des méthodes de spectroscopie résolue en angle (phololuminescence, réflection et transmission) pour caractériser les propriétés des polaritons dans des microcavités optiques de haute qualité incorporant des couches minces de canotubes de carbone fortement concentrées, fabriquées selon un nouveau procédé développé par nos collaborateurs à l'Université du Wisconsin(Madison). Les propriétés des polaritons obtenus (taux de couplage lumière-matière, largeur de raie spectrale) surpassent les valeurs publiées jusqu'à présent dans la littérature scientifique pour les microcavités à base de nanotubes de carbone. Par des mesures de photoluminescence sous excitation continue et ultrarapide des couches minces de nanotubes (en cavité et hors-cavité), nous identifions l'annihilation exciton-exciton et la faible efficacité quantique de photoluminescence comme causes principales empêchant la formation d'un condensat de polaritons dans nos échantillons (même à des températures cryogéniques).

La réponse optique non-linéaire du mode polaritonique est caractérisée par des mesures de transmission résolue en angle sous excitation résonante ultrarapide, et un modèle numérique dans le domaine temporel est développé pour analyser les résultats.

Finalement, nous développons un modèle numérique à éléments finis implémentant l'équation de Gross-Pitaevskii pour modéliser les phénomènes hydrodynamiques observés par nos collaborateurs à l'Université du Nebraska(Lincoln) dans des microcavités optiques utilisant le perovskite inorganique $CsPbBr_3$. Nous observons une bonne correspondance qualitative et quantitative entre le modèle et les résultats expérimentaux.

ABSTRACT

Exciton-polaritons are hybrid light-matter quasiparticles. They are formed in optical microcavities containing a semiconductor material, when the rate of coherent energy exchange between the material and the cavity mode overcomes their combined intrinsic decay rate. This defines the strong light-matter coupling regime, evidenced by drastic changes in the absorption spectrum from the emergence of polaritons as the new eigenstates of the coupled system. The unique properties of polaritons (including boson statistics, low effective mass, and nonlinear interactions) make them a particularly interesting system for studying light-matter interaction and quantum optics, and could enable the development of new photonic devices. An important potential technological application is the use of polariton condensate states as coherent light sources with a much lower emission threshold than conventional lasers.

In this work, we focus on polaritons using semiconductor materials with high exciton binding energy : carbon nanotube and inorganic perovskites. These materials posses attractive properties for strong light-matter coupling experiments : the excitons are stable at room temperature, with a large oscillator strength and long lifetime. Furthermore, good quality thin films can be fabricated from solution processes rather than epitaxial growth.

We use angle-resolved photoluminescence, reflectance and transmission spectroscopy to characterize the properties of polaritons in high-quality optical microcavities containing dense carbon nanotube thin films, fabricated by a novel method developed by collaborators at the University of Wisconsin-Madison. The measured polariton properties (light-matter coupling rate, polariton linewidth) surpass the best values reported in the literature for carbon nanotube exciton-polaritons. By photoluminescence measurements of thin films and microcavities under continuous and ultrafast nonresonant excitation, we show that exciton-exciton annihilation and low photoluminescence quantum yield are the two dominant factors which prevent the formation of a polariton condensate in our samples even at low temperatures.

The subthreshold nonlinear optical response of the polariton microcavities is characterized by angle-resolved transmission measurements under ultrafast resonant excitation, and a time-domain numerical model is developed to analyze the results.

Finally, we develop a numerical model using a finite-element method implementation of the Gross-Pitaevskii equation to model hydrodynamic phenomena observed by collaborators at the University of Nebraska-Lincoln in optical microcavities using the inorganic perovskite semiconductor $CsPbBr_3$, and find good qualitative and quantitative agreement between the model and the experimental results.

TABLE OF CONTENTS

LIST OF TABLES

LIST OF FIGURES

LIST OF SYMBOLS AND ACRONYMS

CNT Carbon Nanotube

PL Photoluminescence

PFO-BPy Polyfluorene-Bipyridine

GPE Gross-Pitaevskii Equation

UP Upper Polariton

LP Lower Polariton

EEA Exciton-Exciton Annihilation

FWHM Full Width at Half-Maximum

DBR Distributed Bragg Reflector

PLQY Photoluminescence Quantum Yield

2PA Two-Photon Absorption

UWM University of Wisconsin-Madison

PTFE Polytetrafluoroethylene

THF Tetrahydrofuran

ODCB o-Dichlorobenzene

MCE Mixed Cellulose Ester

SEM Scanning Electron Microscope

PVAc Polyvinyl Acetate

TMM Transfer-Matrix Method

TE Transverse Electric

TM Transverse Magnetic

OA Open Aperture

CA Closed Aperture

MP Middle Polariton

SNR Signal-to-Noise Ratio

CW Continuous-Wave

SC Supercontinuum

YAG Yttrium-Aluminium Garnet

PFO Polyfluorene

CTE Coefficient of Thermal Expansion

FEM Finite Element Method

SBC Scattering Boundary Condition

FDTD Finite Difference Time Domain

CFL Courant-Friedrich-Lévy

FROG Frequency-Resolved Optical Gating

GDD Group Delay Dispersion

DMSO Dimethyl Sulfoxide

AFM Atomic Force Microscopy

PDE Partial Differential Equation

LIST OF APPENDICES

CHAPTER 1 INTRODUCTION

1.1 General introduction

Polaritons are hybrid quasiparticles formed in the strong light-matter coupling regime, when the rate of coherent energy exchange between a matter excitation and a mode of the electromagnetic field is sufficiently high to overcome the intrinsic decay rate of both states. They possess properties inherited both from their light and matter components, enabling various nonlinear quantum phenomena to be observed, the most famous of which is the formation of a polariton condensate state. The strong light-matter coupling regime has been demonstrated using many materials and resonator geometries, each with advantages and drawbacks, and not all of which allow polariton condensation. Carbon nanotubes (CNTs) are a semiconductor material with attractive properties including a large exciton binding energy, large oscillator strength, and fabrication by solution processing. There have been some reports of polariton microcavities using CNTs, showing that the light-matter coupling strength can be very high, but that low cavity quality factor causing short polariton lifetime is a major issue.

1.2 Research Objectives

The aim of the research project was to exploit the opportunities enabled by a fabrication process recently developed in the Arnold group at the University of Wisconsin-Madison. This process allows them to produce high-quality optical microcavities with very high concentration films of purified carbon nanotubes.

Using these microcavity samples, we set out to achieve the following research objectives :

1. Achieve higher light-matter coupling strength and longer polariton lifetime than was previously possible with CNTs.
2. Investigate the linear and nonlinear optical response of CNT polariton microcavities, using angle-resolved reflection and photoluminescence spectroscopy.
3. Attempt to form a polariton condensate at room temperature, which has never been achieved in CNT polariton microcavities.

1.3 Thesis Outline

This thesis comprises five chapters, excluding introduction and conclusion.

Chapter 2 is a review of the fundamental concepts underpinning the work. First, we introduce the concept of exciton-polaritons, and the phenomena that arise from polariton-polariton interactions. We then describe the photophysics of semiconducting carbon nanotubes, the material used in all the experiments discussed in Chapters 3-5. A discussion of nonlinear optics follows, which is essential to understand the experiments and numerical modelling in Chapter 5. Finally, we present a short literature review of carbon nanotube microcavities.

In Chapter 3, we describe the process of microcavity design and fabrication, as well as the various characterization techniques that were used to tune fabrication parameters in order to obtain the desired cavity properties. We then describe the experimental setup used for angle-resolved reflection and photoluminescence (PL) spectroscopy, which was the main experimental technique used throughout the project. We conclude this chapter by discussing the measurements of CNT polaritons in the ultrastrong coupling regime, as well as the design of cavities with a very narrow-linewidth polariton state.

In Chapter 4, we discuss photoluminescence measurements of CNT bare films and microcavities, in the steady-state and short-pulse optical pumping regimes. We observe properties of high-concentration CNT films that are detrimental to their use in polariton devices; namely, a rapid photoinduced degradation, and a strongly suppressed PL emission intensity under pulsed excitation compared to continuous-wave pumping. We calculate the exciton-exciton annihilation (EEA) coefficient from these experiments, and find that EEA explains the observed reduction in polariton PL intensity. Finally, we find that even for the highest quality-factor microcavities fabricated, we are unable to observe polariton condensation, even at cryogenic temperatures.

In Chapter 5, we discuss the measurement and numerical modelling of the optical third-order nonlinearity of exciton-polaritons. We first describe the measurement, using a modified version of the Fourier imaging microscope described in Chapter 3. Then, we show the results of measured polariton mode blueshift for two microcavities with different detunings. Finally, we discuss the implementation of a time-domain finite-element numerical model to simulate the response of a polariton cavity to a femtosecond resonant pump pulse, including a third-order nonlinear polarization term. We show that the model is robust with respect to variations in the pump pulse duration, spectral shape, or chirp, and that it correctly reproduces the measured blueshift in the case of a purely refractive nonlinearity, but fails when saturable absorption is present. We also examine a discrepancy between the model and experimental results relating to the transmitted intensity at zero angle, and show with additional simulations that it is caused by the modulation of refractive index in the in-plane direction.

Chapter 6 is dedicated to a different but related research project, where we developed a finite-element time-domain numerical model implementing the driven-dissipative Gross-Pitaevskii equation (GPE). This was done in order to model experiments performed by our collaborators on polariton microcavities using not carbon nanotubes, but a different semiconductor with strongly-bound excitons : lead halide perovskite crystals. We explain how the model was implemented, how the available experimental parameters were used to calculate the appropriate coefficients of the GPE, and show that the model reproduces experimental results for different values of pump fluence and injected in-plane momentum.

CHAPTER 2 THEORY BACKGROUND AND LITERATURE REVIEW

In this chapter, we will give a brief overview of the important theoretical concepts underpinning the work, namely : strong light-matter coupling, the photophysics of carbon nanotubes, and classical nonlinear optics. This is followed by a review of the published reports on carbon nanotube exciton-polaritons.

2.1 Strong light-matter coupling

The interaction between an excitation of the electromagnetic field and an excitation in a material reaches the strong coupling regime when the rate of coherent energy exchange between the two excitations is faster than their combined rate of decay. This is expressed as $\Omega_R > \gamma_c + \gamma_x$, where Ω_R is the coupling rate, and $\gamma_{c,x}$ are the decay rates of the electromagnetic mode and the material excitation respectively. In the strong light-matter coupling regime, the behaviour of the system is best described by defining new excitations (polaritons) which are coherent superpositions of light and matter states. This has been realized with many different types of excitations in various materials [1]; there are plasmon-polaritons, phonon-polaritons, magnon-polaritons, etc. In this work, we focus on the strong coupling between bound electron-hole pairs in semiconductors (excitons) and photon excitations in a planar optical microcavity, creating microcavity exciton-polaritons. For simplicity, we will simply refer to these as "polaritons" in the rest of the work.

2.1.1 Excitons in semiconductors

The electronic band structure in solids generally contains a set of continuous bands of allowed electronic states separated by *band gaps*, i.e. ranges of energy where no allowed electronic state exists. A material is a semiconductor when its Fermi level (the energy required to add an electron to the system) is inside a band gap [2]. In this case, the electronic states below the gap (in the valence band) are fully occupied, and the states above the gap (in the conduction band) are unoccupied.

When a photon is absorbed in the solid, adding energy to the system, an electron can be excited from the valence band to the conduction band. The many-body quantum state of the valence band with $N-1$ electrons can be represented by defining a collective excitation with a positive charge and effective mass, called an *electron hole*. Since the electron and hole have opposite charges, they can be bound by Coulomb interaction to form a chargeless composite quasiparticle, the *exciton*. Excitons have a hydrogen-like energy level structure, and their spatial extent can be described by a Bohr radius a_0. The exciton bound state exists for a short time until it either decays radiatively when the electron and hole recombine, or nonradiatively when its coherence is destroyed by scattering of the electron or hole on a defect in the material. Excitons can also decay nonradiatively *via* exciton-exciton annihilation (EEA), where one exciton is destroyed and its energy transferred to another exciton [3]. EEA becomes an important relaxation pathway when the exciton density is high, which is the case in experiments pumped with ultrafast laser pulses.

Excitons can behave quite differently depending on the strength of the Coulomb interaction between electron and hole. In semiconductors with a low dielectric constant (such as organic semiconductors), we observe Frenkel excitons : the exciton binding energy is large, on the order of 100 meV [4], and the Bohr radius is very small. The exciton is localized to a a single crystalline unit cell or a single molecule. In semiconductors with a large dielectric constant, we observe Wannier-Mott excitons. Electric field screening reduces the strength of the Coulomb interactions, such that the binding energy is only a few meV (and therefore not thermodynamically stable at room temperature) and the exciton is delocalized across a large number of crystalline cells. This is typical of inorganic semiconductors, for example GaAs with an exciton binding energy of 4.9 meV [5]

2.1.2 Photon modes in microcavities

Optical cavities are structures which confine light in one or more dimensions, constraining the local density of states of the electromagnetic field from a continuum to a number of discrete modes. *Microcavities* are cavities where the length scale is on the order of the wavelength of the light. This high degree of confinement leads to a large field enhancement inside the cavity. Various geometries can be used to achieve this result, such as dielectric microdisks or microspheres [6] [7], waveguide-coupled microrings [8] or one- and two-dimensional photonic crystals [9] [10]. The simplest case to describe mathematically, which nevertheless exhibits all the properties relevant to us for the purposes of this work, is the Fabry-Pérot microcavity.

The Fabry-Pérot cavity structure is defined as two parallel planar mirrors separated by a gap of width L filled by a material of refractive index n. The resonant modes of the cavity are defined by the following condition on the out-of-plane wavevector inside the cavity (the phase of the electric field must be a multiple of 2π after a round-trip):

$$k_\perp = p\frac{\pi}{L} \tag{2.1}$$

where $p = 1, 2, 3...$ is the mode order index. At normal incidence ($k_z = |k|$) and considering the fact that the resonance condition applies to the wavevector inside the cavity (where the refractive index is n), the resonance frequency $\omega_0 = 2\pi/|k_0|$ of the p-th order cavity mode is

$$\omega_0 = p\frac{\pi c}{nL} \tag{2.2}$$

When the electromagnetic wave is propagating with an non-normal angle of incidence θ (i.e. $k_\parallel \neq 0$), the magnitude of the wavevector must be larger to satisfy the resonance condition on $k_\perp$. From the definition of the out-of-plane wavevector component $k_\perp = |k|\cos\theta$, we can derive the following relation for the dispersion of the resonance frequency of the fundamental cavity mode ($p = 1$):

$$\omega(\theta) = \frac{\omega_0}{\sqrt{1 - \left(\frac{\sin\theta}{n}\right)^2}} \tag{2.3}$$

Note that it is often useful to express the cavity mode dispersion in terms of the in-plane component of the wavevector :

$$\omega(k_\parallel) = \sqrt{\omega_0^2 + \left(\frac{c}{v}k_\parallel\right)^2} \tag{2.4}$$

If we do a series expansion of this expression around $k_\parallel = 0$ and discard the higher-order terms, the energy dispersion of the cavity mode at low incident angles becomes equivalent to that of a free particle with an effective mass $m_{eff} = \frac{n^2}{c^2}\hbar\omega_0$,

$$\hbar\omega(k_\parallel) = \hbar\omega_0 + \frac{\hbar^2 k_\parallel^2}{2m_{eff}}. \tag{2.5}$$

The effective mass of a microcavity photon is extremely small : taking typical values of $\hbar\omega_0 = 2\text{eV}$ and $n = 1.5$, $m_{eff} = 8 \cdot 10^{-36}\text{kg}$, or five orders of magnitude smaller than the electron mass. This has important implications for the formation of polariton condensates, further discussed in 2.1.4.

For metal-mirror microcavities, L can be taken directly as the separation distance between the mirrors. However, the case of dielectric mirrors, an effective cavity length L_{eff} must be used, taking into account the penetration depth of the field in the mirrors. This penetration depth varies as a function of the wavelength and incident angle, which can cause a slight deviation between the actual dispersion and this simple model. However, as we will see in Chapter 3, equation 2.3 can reproduce the measured cavity mode dispersion in real samples quite well, in the range of wavelengths and angles we are interested in.

A critical property of the cavity mode is its quality factor Q, expressing the degree of confinement of the electromagnetic field. For any resonance, the quality factor is defined by

$$Q \equiv \frac{\omega_0}{\gamma} \tag{2.6}$$

where ω_0 is the resonant frequency and γ is the full-width at half-maximum (FWHM) linewidth of the resonance. In a Fabry-Pérot cavity with identical mirrors of reflectance R, the quality factor is given by the expression

$$Q = \frac{2\omega_0 n L}{c(1-R)^2} \tag{2.7}$$

For metal mirrors, the reflectance is limited to about 98%, which in microcavities (where L is small) limits the quality factor to 100-200. However, using dielectric mirrors, the reflectance can be dramatically improved, with commercially-available epitaxially-deposited crystalline dielectric mirrors reaching $R = 99.999\%$ [11] and more common sputtered distributed Bragg reflector (DBR) mirrors (such as the ones fabricated for this project) reaching $R = 99.8\%$. Note that the expression above considers only the mirror losses, while in a cavity filled with a real material, there would also be absorption losses.

The term for the loss per round trip $(1-R)^2$ should then be updated to $(1-R-A)^2$ with A being the one-way-trip power loss from material absorption. Other possible losses that can reduce the cavity mode lifetime include scattering from surface roughness, and imperfect mirror flatness or parallelism [12].

The rate of decay (from leakage through the mirrors to the outside environment, and from absorption) of the energy confined by the cavity mode is an important parameter for defining the strong light-matter coupling regime and directly depends on the quality factor :

$$\gamma = \frac{\omega_0}{Q} \tag{2.8}$$

2.1.3 Coupled-oscillator model

The physics of the strongly-coupled cavity-exciton system can be described by employing the second quantization formalism, and representing the cavity mode and exciton as quantum harmonic oscillators [13]. The Hamiltonian describing the coupled system is

$$\hat{H} = \hbar \sum_{k_\parallel} \left(\omega_c(k_\parallel) \hat{a}_k^\dagger \hat{a}_k + \omega_x \hat{b}_k^\dagger \hat{b}_k + \Omega_R (\hat{a}_k^\dagger \hat{b}_k + \hat{a}_k \hat{b}_k^\dagger) \right) \tag{2.9}$$

where $\hbar\omega_c(k_\parallel)$ is the cavity mode energy dispersion as defined in equation 2.3, $\hbar\omega_x$ is the exciton energy (with a negligible energy dispersion compared to the cavity mode, due to the large difference in effective mass), and the Rabi frequency Ω_R is the coupling strength or rate of energy exchange between the cavity mode and exciton[1]. The operators $(\hat{a}_k^\dagger, \hat{a})$ and $(\hat{b}_k^\dagger, \hat{b})$ are the bosonic annihilation and creation operators for the cavity mode photon and exciton respectively, and the term $(\hat{a}_k^\dagger \hat{b}_k + \hat{a}_k \hat{b}_k^\dagger)$ describes the coupling, where a photon is destroyed while an exciton is created with the same wavevector, and vice versa.

In the Fock basis $|N_c, N_x\rangle$, the matrix representation of the Hamiltonian in the single-excitation reduced space $\{|1,0\rangle, |0,1\rangle\}$ is

$$\hat{H}' = \hbar \sum_{k_\parallel} \begin{pmatrix} \omega_c(k_\parallel) & \Omega_R \\ \Omega_R & \omega_x \end{pmatrix} \tag{2.10}$$

[1] Ω_R is proportional to $\sqrt{Nf/V}$ with N the number of excitons coupled to the cavity, f the exciton transition oscillator strength, and V the cavity mode volume [14]

The eigenstates of this Hamiltonian are coherent superpositions of the cavity photon and exciton states : the exciton-polaritons. For each in-plane wavevector $k_\parallel$ there are two eigenstates which are identified as the upper polariton (UP) and lower polariton (LP) according to their energy. The LP and UP energies are the eigenvalues of $\hat{H}'$:

$$E_{UP,LP}(k_\parallel) = \frac{\hbar}{2}\left(\omega_c(k_\parallel) + \omega_x \pm \sqrt{4\Omega_R^2 + (\omega_c(k_\parallel) - \omega_x)^2}\right) \tag{2.11}$$

Here we can see where the strong coupling condition $\Omega_R > \gamma_c + \gamma_x$ comes from. The energy splitting between the LP and UP states when $\omega_c = \omega_x$ is $2\hbar\Omega_R$. If the Rabi frequency is not large enough to fulfill the strong coupling condition, the splitting will be smaller than the linewidth of the exciton transition and cavity mode, and it will not be possible to resolve the two polariton states. Instead, we would observe a broadening of the bare transition (or, equivalently, an increase in the decay rate).

The coefficients of the eigenvectors $\{|LP_k\rangle, |UP_k\rangle\}$ (termed the Hopfield coefficients) determine the relative contribution of the photon and exciton states of the polariton state. The photon and exciton fraction of a given polariton state (shown below for the LP state) are calculated by projecting the eigenvectors onto the basis vectors of the reduced Fock space:

$$\begin{cases} |C_p(k_\parallel)|^2 = |\langle 1,0|LP_k\rangle|^2 = \frac{1}{2}\left(1 - \frac{\omega_c(k_\parallel)-\omega_x}{\sqrt{(\omega_c(k_\parallel)-\omega_x)^2+4\Omega_R^2}}\right) \\ |C_x(k_\parallel)|^2 = |\langle 0,1|LP_k\rangle|^2 = \frac{1}{2}\left(1 + \frac{\omega_c(k_\parallel)-\omega_x}{\sqrt{(\omega_c(k_\parallel)-\omega_x)^2+4\Omega_R^2}}\right) \end{cases} \tag{2.12}$$

The photon and exciton content of a given polariton state determine its properties [15]. For example, the effective mass of the lower polariton is determined from the cavity photon and exciton effective masses with

$$\frac{1}{m_{LP}} = \frac{|C_p|^2}{m_p} + \frac{|C_x|^2}{m_x} \tag{2.13}$$

and the decay lifetime of the lower polariton is similarly expressed in terms of the cavity mode lifetime and exciton lifetime as

$$\frac{1}{\tau_{LP}} = \frac{|C_p|^2}{\tau_p} + \frac{|C_x|^2}{\tau_x} \tag{2.14}$$

When describing polariton cavities, the cavity energy is usually defined by the detuning Δ between the exciton transition and the cavity mode energy at normal incidence.

$$\Delta \equiv \hbar(\omega_x - \omega_c(0)) \tag{2.15}$$

The main parameters controlling the polariton dispersion for a given semiconductor material (fixing the value of ω_X and n) are therefore Δ and Ω_R. In Figure 2.1, we show the polariton energy dispersions and Hopfield coefficients for the negative, zero, and positive detuning cases.

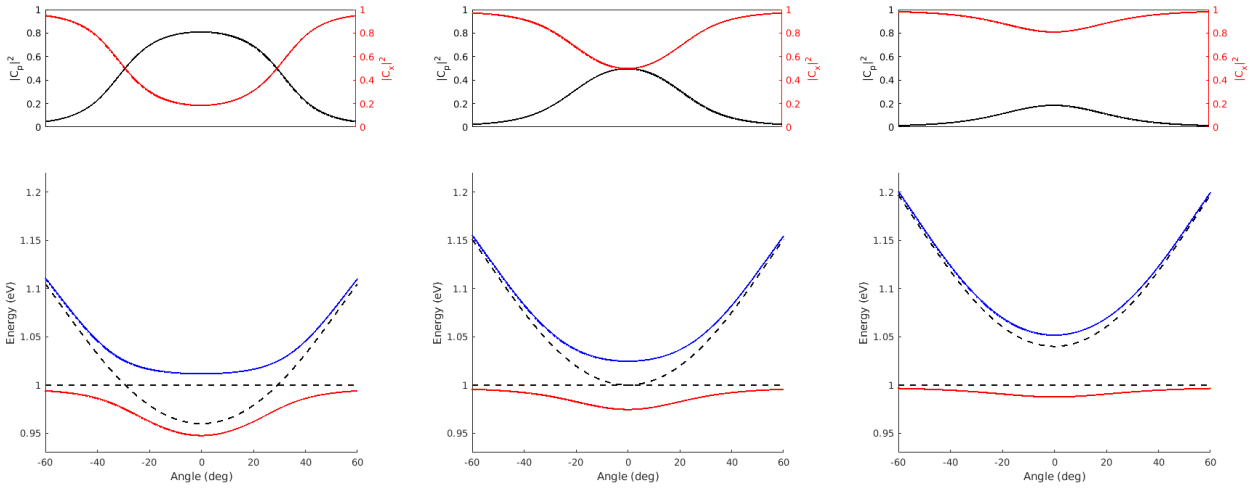

(a) $\Delta < 0$ (b) $\Delta = 0$ (c) $\Delta > 0$

Figure 2.1 Example energy dispersions of the LP(red) and UP (blue) modes and Hopfield coefficients for different values of Δ. The bare exciton transition energy and cavity mode dispersion are indicated with dashed lines.

In the zero detuning case, both polariton states have equal photonic and excitonic fractions. In the negative detuning case, the LP mode has a more photonic character, and in the positive detuning case, the LP mode is more excitonic. This is visible by comparing the curvature of the energy dispersion : as the exciton fraction increases, the polariton effective mass also increases, flattening the energy dispersion.

2.1.4 Polariton-polariton interaction and polariton condensation

Like photons, polaritons follow Bose-Einstein statistics. Unlike photons, however, polaritons are able to interact with each other through Coulomb interaction *via* their excitonic component [16]. The bosonic nature of polaritons means that they are able to form a condensate state, and polariton-polariton interactions enable faster relaxation to the ground state, facilitating the accumulation of polariton density required to reach the condensation threshold.

Bose-Einstein condensation is defined as the macroscopic occupation of a state by an ensemble of bosons, leading to long-range quantum coherence. The phase transition to the condensate state occurs when the mean interparticle spacing (inversely proportional to the polariton density n) becomes smaller than the thermal de Broglie wavelength. In two dimensions, this condition is expressed

$$n > \frac{2m_{eff}}{\pi\hbar^2} k_B T \tag{2.16}$$

The dependence of the condensation threshold on the effective mass is an important reason for the intense research interest in polariton condensation. Their very low effective mass can allow the formation of condensates even at relatively high temperature, and room-temperature polariton condensation has been demonstrated using several different semiconductor materials [17]. To illustrate this point, we consider the value of the thermal de Broglie wavelength $\lambda_{dB} = 321$ nm in the material system where Bose-Einstein condensation was first observed (^{87}Rb dilute atomic vapor, cooled down to $T = 170 \cdot 10^{-9}$ K). For exciton-polaritons with a typical effective mass of $3 \cdot 10^{-35}$ kg, the thermal de Broglie wavelength has the same order of magnitude at room temperature : $\lambda_{dB} = 530$ nm at $T = 300$ K.

In practice, experimentally-realized polariton condensates are typically far from thermodynamic equilibrium because the polariton lifetime is shorter than the thermalization time [18]. As such, their energy distribution function does not exactly follow a Bose-Einstein distribution. However, the phenomena typical of Bose-Einstein condensates can still be observed in polariton condensates, such as superfluidity [19] [20] and the formation of quantized vortices [21].

The long-range quantum coherence associated with the condensed state, in combination with the radiative decay of exciton-polaritons by leakage through the cavity mirrors, means that a polariton condensate emits light with a high temporal and spatial coherence [22], similar to a laser. There are two important distinctions between the emission of a polariton condensate and a traditional laser (which operates in the weak light-matter coupling regime).

First is the origin of the coherence. In a polariton condensate, the coherence of the emitted light comes from the underlying coherence of the polariton population; the particle species that accumulates coherence is polaritons. In conventional lasers, the particle species that accumulates coherence is the cavity photon, and the gain medium is an incoherent bath of excited charge carriers. The difference between the polariton lasing and conventional lasing regimes in the same microcavity has been observed [23], and the difference between the hybrid light-matter nature of polariton lasing and the purely photonic nature of conventional lasing was demonstrated by observing the change in the emission under a strong applied magnetic field.

The second important difference is the density threshold for coherent emission. The polariton density threshold for condensation was shown in Equation 2.16. The lasing threshold for a conventional semiconductor laser is the Mott density

$$n_{\text{Mott}} > \frac{1}{a_0^2} \tag{2.17}$$

where a_0 is the exciton Bohr radius. For example, in gallium nitride, the polariton condensation threshold is $n_c \sim 10^8 \text{cm}^{-2}$ while the Mott density is $n_{\text{Mott}} \sim 10^{13} \text{cm}^{-2}$, five orders of magnitude larger [24]. The numerous potential applications of a tunable coherent light source with a pumping threshold much lower than conventional semiconductor lasers is one of the main reasons motivating the development of polariton devices. In practice, there are numerous engineering challenges (among others, the difficulty of forming a condensate with electrically injected carriers and the poor chemical stability of the semiconductor materials used) to be overcome before polariton sources are commerically competitive with the mature technology of conventional semiconductor lasers [28].

Experimentally, the polariton condensation threshold is characterized by an increase in the slope of polariton emission intensity with applied pump power (or equivalently, a change in the slope of the polariton occupation number), a narrowing of the polariton emission linewidth, and an increase in the slope of the polariton energy shift with applied power [25]. The latter effect is often referred to as the "blueshift" and arises from the polariton-polariton interaction energy. A blueshift proportional to the polariton density can be observed even below the condensation threshold, as we show in Chapter 5, but it becomes much more apparent in a condensate, due to the large increase in polariton density. An example of the experimental signatures of polariton condensation is illustrated in Figure 2.2. In this example, the condensate forms at the minimum of the lower polariton dispersion curve (at $k_{\|} = 0$). This is typical for non-resonantly-pumped microcavities in the negative detuning regime [26]. When a polariton state is populated by resonant excitation, a condensate can be formed at an arbitrary position on the dispersion curve [19]. Condensation can also occur at non-zero momentum states for microcavities pumped non-resonantly, when the pump spot is very small and the detuning is close to zero [27].

Population of the polariton mode from the exciton bath

When a semiconductor-filled microcavity is driven with an external light source, the pump initially excites the LP and UP polariton states in addition to a large background density of dark states (exciton reservoir). Different relaxation and scattering processes then transfer population to the minimum of the lower polariton dispersion [28] at $k_{\|} = 0$, where a condensate will form if sufficient occupation density can be reached. The relative contribution of the different dynamical processes involved depends on the semiconductor material and the cavity properties, and determines whether polariton condensation is possible in a given system. Three important such processes are radiative pumping, phonon-polariton scattering, and polariton-polariton scattering.

In radiative pumping (illustrated in Figure 2.3a), the excitons from the reservoir decay radiatively and excite the $k_{\|} = 0$ polariton state though its photonic part. The radiative pumping rate can be optimized by controlling the cavity-exciton detuning to overlap the bare exciton PL emission with the minimum of the LP dispersion. Radiative pumping has been identified as the main contribution to the occupation of the $k_{\|} = 0$ polariton state in microcavities using the BODIPy-Br molecular dye [29].

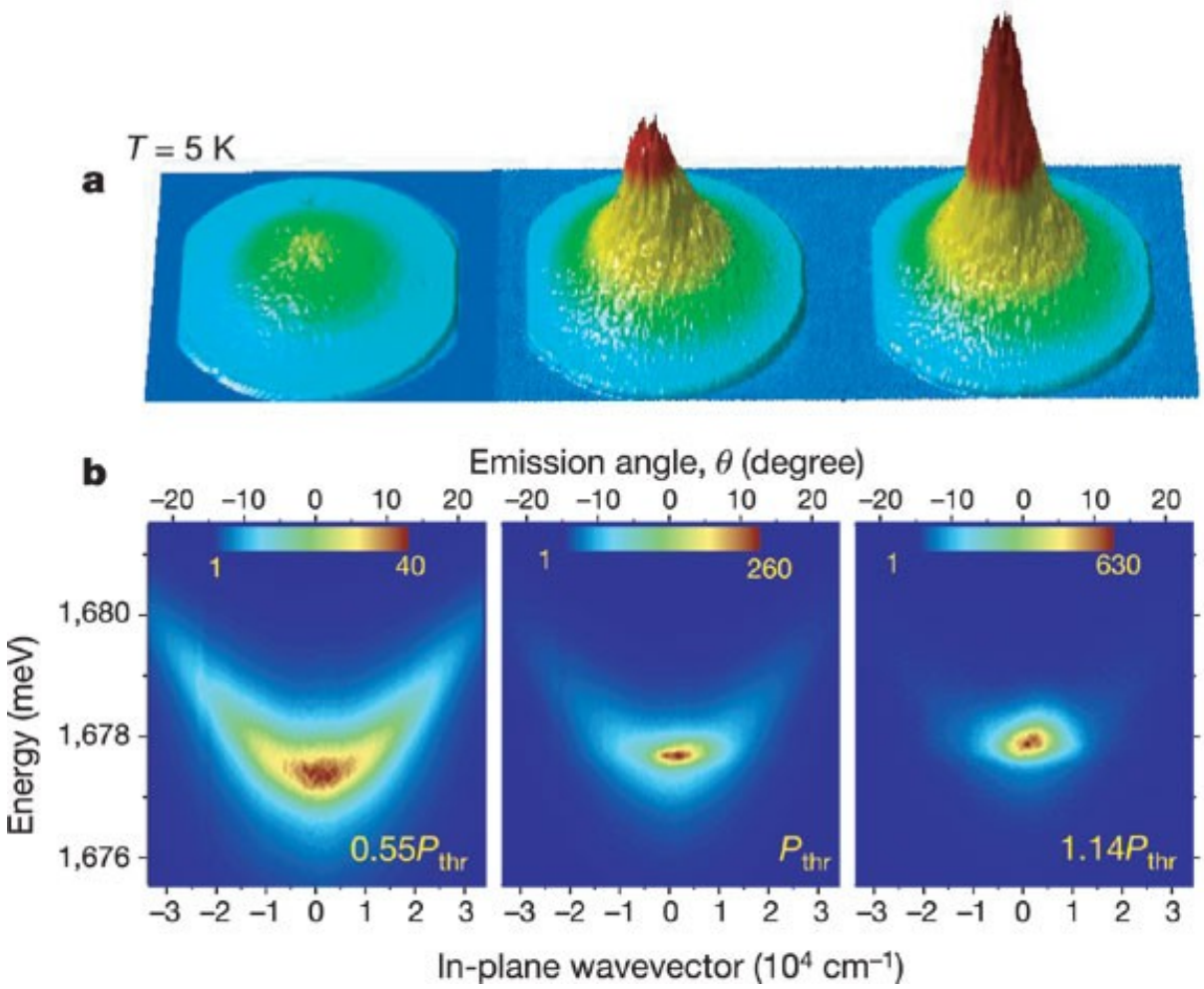

Figure 2.2 Polariton spatially-resolved (a) and angle-resolved (b) photoluminescence emission spectrum in a CdTe quantum well microcavity below and above the condensation threshold. Reproduced (adapted) with permission from [25].

Polaritons created at very high momenta (where the lower polariton is mostly excitonic in nature) dissipate energy quickly through polariton-phonon scattering mediated by the Coulomb interaction of the excitonic component [18]. As the polaritons move down the LP branch dispersion curve, the rate of this scattering process decreases (as the exciton fraction of the LP state diminishes). At the dispersion inflection point where $|C_p|^2 = |C_x|^2$, the energy dissipation from phonon scattering becomes negligible. In systems where the cavity mode lifetime is smaller than the exciton lifetime, this is also accompanied by a reduction in the polariton lifetime. This creates a "bottleneck" in the polariton population where relaxation to lower momenta is inhibited [30].

Polaritons with the same momentum $k_{\|}$ can interact with each other in an elastic scattering process [31] (illustrated in Figure 2.3b). One polariton is scattered higher up the dispersion curve to $2k_{\|}$ and the other is scattered to the $k_{\|} = 0$. This can overcome the polariton relaxation bottleneck, as the polariton scattered to higher momentum can efficiently cool again through polariton-phonon scattering.

Both spontaneous elastic polariton-polariton scattering and stimulated scattering are possible [31]. If the occupation of the $k_{\|} = 0$ state is sufficiently high, the stimulated scattering process (where the scattering rate is enhanced by the final state occupation) dominates, the occupation at $k_{\|} = 0$ increases substantially, and the condensate is formed.

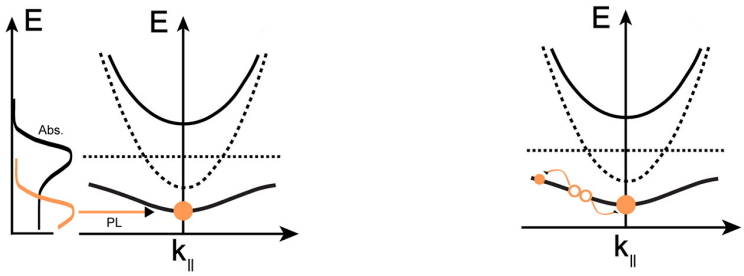

(a) (b)

Figure 2.3 Schematic representation of different processes that can contribute to populating the $k_{\|} = 0$ polariton state from the exciton bath. (a) In radiative pumping, spontaneous emission of reservoir excitons is reabsorbed by the polariton state. (b) Polariton-polariton scattering, sending one polariton to the $k_{\|} = 0$ state and the other one to a higher-momentum state. Reproduced (adapted) from [28] under CC-BY 4.0 license.

Dynamics of a polariton condensate

The dynamics of a coherent gas of interacting polaritons are complex, but can be well-represented by a mean-field approximation (using classical evolution equations for the expectation values of the quantum field theory). Within this approximation, the dynamics of the polariton field are described by a nonlinear partial differential equation named the Gross-Pitaevskii equation [32], in the "driven-dissipative" formulation which includes terms for the pumping and decay of the polariton population (as opposed to the canonical GPE, derived for boson gases with a conserved number of particles such as condensates of cold atoms).

$$i\hbar\frac{\mathrm{d}}{\mathrm{d}t}\begin{pmatrix}\psi_C(\mathbf{r},t)\\ \psi_X(\mathbf{r},t)\end{pmatrix} = \begin{pmatrix}P(\mathbf{r},t)\\ 0\end{pmatrix} + \left[\hat{H}' + \begin{pmatrix}-\frac{i\hbar\gamma_C}{2} & 0\\ 0 & V_x(\mathbf{r}) - \frac{i\hbar\gamma_x}{2} + g_X|\psi_X(\mathbf{r},t)|^2\end{pmatrix}\right]\begin{pmatrix}\psi_C(\mathbf{r},t)\\ \psi_X(\mathbf{r},t)\end{pmatrix} \tag{2.18}$$

The photon part of the state (represented by the wavefunction ψ_C) is pumped by a driving term $P(\mathbf{r},t)$ and decays with a rate γ_C. The exciton part of the state (represented by the wavefunction ψ_X) is subject to an external potential $V(\mathbf{r})$ (representing for example a defect in the material), decays at a rate γ_X, and the exciton-exciton interaction potential is described using the parameter g_X.

The term $\hat{H}'$ is the single-particle Hamiltonian given by

$$\hat{H}' = \begin{pmatrix}\hbar\omega_0 + \frac{\hbar^2 k_\parallel^2}{2m_{cav}} & \hbar\Omega_R\\ \hbar\Omega_R & \hbar\omega_x\end{pmatrix} \tag{2.19}$$

identical to the one derived in section 2.1.3.

In many cases, the GPE can be simplified further, by assuming that only the lower polariton mode has non-negligible occupation [16]. This was done for the numerical simulations presented in Chapter 6.

2.2 Photophysics of Carbon Nanotubes

Carbon nanotubes are an allotrope of carbon shaped like a cylinder (or several concentric cylinders) with a diameter on the order of a nanometer, and length that can reach several centimeters [33]. Since their initial discovery in 1991 in the soot from a carbon-electrode arc discharge [34], their unique mechanical, electronic, and optical properties have attracted much interest, and the processes for their synthesis and purification have been greatly improved. The original 1991 report by Ijima has now been cited in over 30 000 publications.

In the context of this project, we are interested in the optical response of semiconducting CNTs, which are dominated by excitonic effects due to the confinement of charge carriers to the tube surface. We will describe the origin of the electronic band gap in CNTs and discuss the photophysics of CNT excitons. Experimental details concerning the chirality purification and thin film fabrication will be discussed in section 3.1.1.

2.2.1 Chirality and electronic band structure

The structure of carbon nanotubes can be defined by first considering a piece of graphene (a sheet of carbon atoms in a hexagonal pattern) and rolling it along a defined vector $\mathbf{C}_h$ to form a cylinder (Figure 2.4a).

$$\mathbf{C}_h(n,m) = n\mathbf{a}_1 + m\mathbf{a}_2 \tag{2.20}$$

$\mathbf{C}_h(n,m)$ is named the chiral vector, and is defined in terms of the graphene lattice basis vectors $\mathbf{a}_1$ and $\mathbf{a}_1$. Nanotubes with a structure defined by $\mathbf{C}_h(n,m)$ are said to have the chirality (n,m).

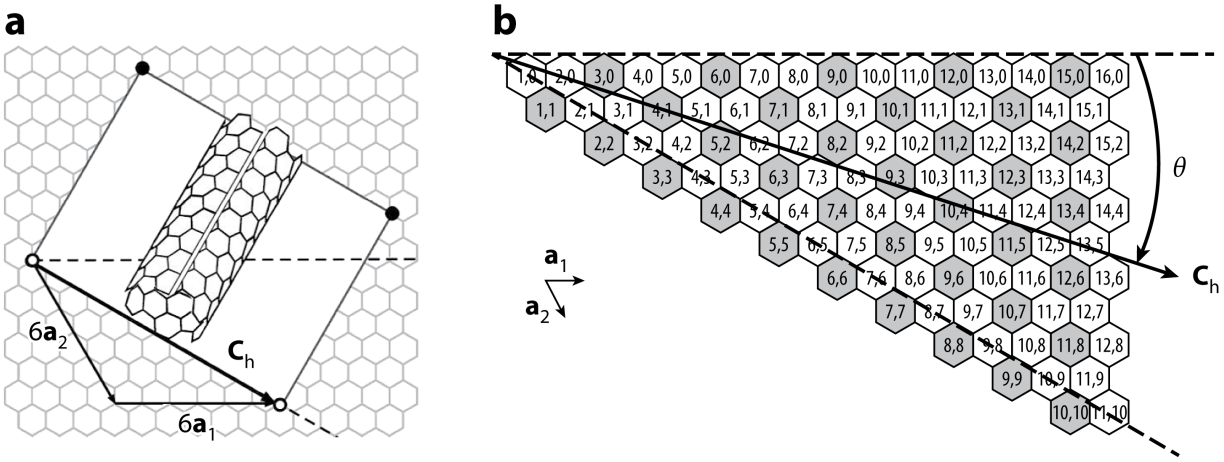

Figure 2.4 Structure of single-walled carbon nanotubes and definition of the chiral vector. Reproduced (adapted) with permission from [35]. Copyright 2018 by Annual Reviews.

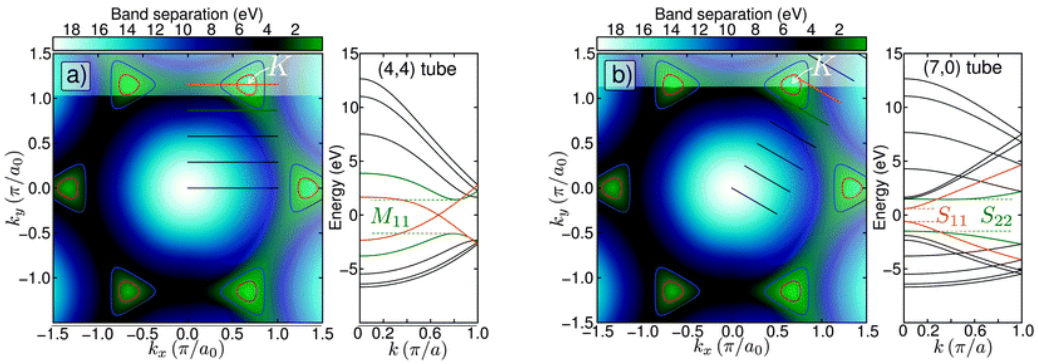

(a) (b)

Figure 2.5 Contour maps of band separation in the first Brillouin zone of graphene, overlaid with the lines of allowed states for CNTs. The associated CNT electronic band structure is also plotted to the right of each contour map. (a) Metallic CNT : the lines of allowed states cross the K point. (b) Semiconducting CNT : the lines of allowed states do not overlap with a K point, creating a band gap. Reproduced (adapted) with permission from [36].

The electronic band structure of graphene does not have a gap : the valence and conduction bands connect at six points (named the **K**-points). However, when a graphene sheet is rolled into a cylinder, the wavevector of the electrons are constrained by a periodic boundary condition enforcing continuity of the electron wavefunction around the tube's circumference.

$$\mathbf{k} \cdot \mathbf{C}_h = 2\pi q \quad (q \in \mathbb{Z}) \tag{2.21}$$

The values of **k** satisfying the periodicity condition for a given CNT chirality define one-dimensional "lines of allowed states" on the two-dimensional band structure of graphene (Figure 2.5). For values of n, m such that $\mathrm{mod}(n - m, 3) = 0$, the lines of allowed states cross a K-point, and the CNT is metallic : it has no bandgap. For other CNT chiralities, the lines of allowed states avoid the K-points and the CNTs are semiconducting, with a bandgap scaling inversely with CNT diameter. The different lines of allowed states define different electronic state bands, labelled with an index j. The transitions between the j_1 valence band and the j_2 conduction band are noted $S_{j_1 j_2}$.

The selection rules for conservation of angular momentum allow optical excitation of $S_{j_1 j_2}$ transitions, with the condition that the electric field must be parallel with the CNT axis for S_{jj} transitions and transverse to the CNT axis for $S_{j_1 \neq j_2}$ transitions. The S_{jj} transitions have a large oscillator strength [37]. The oscillator strength of $S_{j_1 \neq j_2}$ transitions is suppressed by the depolarization effect, and typically only S_{jj} transitions are considered [38] when interpreting CNT optical absorption spectra.

2.2.2 Excitons in CNTs

Optical excitation of a S_{jj} transition forms an exciton due to Coulomb interaction between the electron and hole, as discussed in section 2.1.1. The confinement of charge carriers to the CNT surface forces the electron and hole to remain in close proximity, giving excitons in nanotubes an unusually large binding energy of several hundred meV [35]. Apart from their large binding energy, they exhibit features typical of Wannier-Mott excitons, such as delocalization over a large spatial extent [39]) and high mobility [40].

There are two non-equivalent K-points in the first Brillouin zone, leading to four potential singlet excitons [41]. The lowest-energy exciton has zero angular momentum and even parity, so it is dipole-forbidden. The second exciton has zero angular momentum and odd parity, so optical excitation is allowed : we call this transition the direct bright S_{11} exciton. The remaining two excitons are degenerate in energy 36 meV above the bright S_{11} transition [42] and correspond to indirect transitions between subbands with different indices j_1, j_2, with a nonzero linear momentum. However, the indirect transitions (which we call the K-momentum dark exciton) can still occur with the assistance of a D-band phonon at 1300 cm^{-1} [43]. This transition appears in the absorption spectrum as a peak near 1.43 eV.

The proposed mechanism of the phonon-assisted brightening of a dark exciton was confirmed by Blackburn *et al.* comparing the spectra of CNTs synthesized from ^{12}C and ^{13}C isotopes, which showed that the peak is shifted by the same amount as the D-band phonon [44]. The states involved in this transition are illustrated in Figure 2.6.

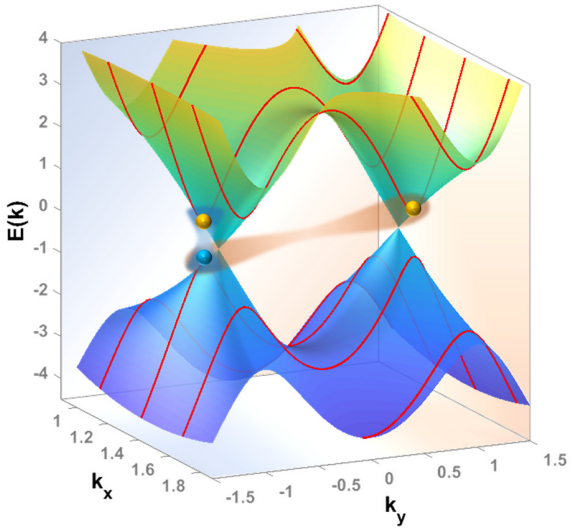

Figure 2.6 Schematic representation of the bright S_{11} direct exciton transition (highlighted in blue) and the phonon-assisted K-dark exciton transition (highlighted in orange). Reproduced (adapted) with permission from [45].

For the use of CNTs in polariton microcavities, an important parameter is the photoluminescence quantum yield (PLQY), defined as the ratio of radiative decay rate to total decay rate. In carbon nanotubes, the PLQY of excitons is very low. Depending on synthesis and processing methods, PLQY values from 0.2% to 2.4% have been reported for the S_{11} exciton for the (6,5) chirality (CNTs suspended in dilute solution) [46].

Excitons are quenched by scattering on defects in the CNT sidewall or when they diffuse to the ends of the tube [47]. The generally accepted explanation for the low PLQY is that due to the high mobility of excitons and the long intrisic exciton lifetime, excitons are likely to be quenched by encountering a defect before they can recombine radiatively, even at low defect densities [48] [49].

Using milder processing methods (shear-force mixing compared to tip sonication) has been shown to improve the PLQY from 1.5% to 2.4% [46] of as it introduces fewer defects and produces longer tubes. Aside from damage from aggressive processing, defects can also be introduced by surface adsorption of charged impurities [50] or by oxidation [51].

A recently developed approach for improving the PLQY aims to introduce new defects through chemical functionalization. These artificial defects locally perturb the band structure of the nanotube and creates a lower-lying energy level that traps the exciton without quenching it [49], providing more time for the exciton to decay radiatively. A dramatic improvement in PLQY can be observed for very short nanotubes [52], but the improvement for micrometer-length, low-defect-density CNTs is only a factor of two [53].

All of these results were measured on CNTs in dilute solution. In dense thin films, the PLQY is reduced further by an order of magnitude (0.17% in films of shear-force-mixed (6,5)CNT:PFO-BPy with a concentration of 39%wt) [54], due to the introduction of numerous exciton quenching sites at the point of contact between different tubes.

2.3 Nonlinear optics

To provide a theoretical background for the discussion of the nonlinear optical measurements and simulations presented in Chapter 5, we summarize some basic concepts of classical nonlinear optics, with a focus on monochromatic parametric and non-parametric $\chi^{(3)}$ processes.

The response of a material to an applied electric field $\mathbf{E}$ is classically described in terms of an induced polarization density $\mathbf{P}$ adding a contribution to the applied field, to give a displacement field $\mathbf{D}$.

$$\mathbf{D}(t) = \epsilon_0 \mathbf{E}(t) + \mathbf{P}(t) \tag{2.22}$$

The relation between the induced polarization density and the applied electric field is parametrized by the material electric susceptibility χ :

$$\mathbf{P}(t) = \epsilon_0 \chi \mathbf{E}(t) \tag{2.23}$$

As the material response is not instantaneous, the induced polarization is more properly expressed as a function of time, as a convolution integral over all past values of the applied electric field.

$$\mathbf{P}(t) = \epsilon_0 \int_{-\infty}^{t} \chi(t - t')\mathbf{E}(t')\ \mathrm{d}t' \tag{2.24}$$

It is convenient to work in the frequency domain, since taking the Fourier transform of equation 2.25 turns the convolution integral into a simple product.

$$\mathbf{P}(\omega) = \epsilon_0 \chi(\omega)\mathbf{E}(\omega) \tag{2.25}$$

The frequency-domain electric susceptibility $\chi(\omega)$ is related to the refractive index dispersion $n(\omega)$, which can be measured experimentally *via* ellipsometry, as will be discussed in section 3.2.

$$n(\omega) = \sqrt{1 + \chi(\omega)} \tag{2.26}$$

It should also be noted that in the formalism where the electric field is represented as $\mathbf{E}(t) = \mathbf{E_0} e^{i(\mathbf{k}\cdot\mathbf{r} - \omega t)}$, the refractive index and the electric susceptibility are complex quantities. The real part relates to light refraction (affecting the phase of the wave) and the imaginary part to absorption (affecting the amplitude).

The linear dependence of the induced polarization as stated in equation 2.26 is valid up to a certain field amplitude, but it cannot be valid for an arbitrarily large applied electric field, because the bound charges in the material that create the induced dipole cannot be displaced infinitely far from their equilibrium positions. Therefore, at some value of applied field amplitude, the $\mathbf{P}$ field must begin to deviate from a simple proportionality relation to $\mathbf{E}$.

This can be mathematically described by a series expansion of $\mathbf{P}$ [55].

$$\mathbf{P}(\omega) = \epsilon_0 \left(\chi^{(1)}(\omega)\mathbf{E}(\omega) + \chi^{(2)}(\omega)\mathbf{E}^2(\omega) + \chi^{(3)}(\omega)\mathbf{E}^3(\omega) + ... \right) \tag{2.27}$$

The first-order term of χ is the linear susceptibility, and the higher-order terms add non-linear corrections to the induced polarization. Note that for materials which have inversion symmetry, all the even-order terms in the expansion vanish.

The linear electric susceptibility is a 3-by-3 matrix, representing the polarization in each direction induced by an electric field in each direction.

$$\begin{bmatrix} P_x \\ P_y \\ P_z \end{bmatrix} = \epsilon_0 \begin{bmatrix} \chi^{(1)}_{xx} & \chi^{(1)}_{xy} & \chi^{(1)}_{xz} \\ \chi^{(1)}_{yx} & \chi^{(1)}_{yy} & \chi^{(1)}_{yz} \\ \chi^{(1)}_{zx} & \chi^{(1)}_{zy} & \chi^{(1)}_{zz} \end{bmatrix} \begin{bmatrix} E_x \\ E_y \\ E_z \end{bmatrix} \tag{2.28}$$

For an isotropic material, this is a diagonal matrix with all elements identical, but in material with lower symmetry, the form of the matrix is more complicated. This causes phenomena such a birefringence, a change in refractive index dependent on the orientation of the light polarization with respect to the material principal axes.

In the case of the nonlinear electric susceptibility, $\chi^{(N)}$ is represented as a $(n+1)$-rank tensor, which will describe the induced nonlinear contribution to the polarization as

$$P_i^{(2)} = \epsilon_0 \sum_{jk} \chi^{(2)}_{ijk} E_j E_k \tag{2.29}$$

$$P_i^{(3)} = \epsilon_0 \sum_{jkl} \chi^{(3)}_{ijkl} E_j E_k E_l \tag{2.30}$$

$$...$$

Where the number of independent elements and the tensor symmetries are determined by the symmetries of the underlying material. In the case of carbon nanotube thin films, the material has uniaxial optical anisotropy, with the optical axis normal to the film plane.

This means that in the TE polarization, the susceptibility does not depend on the angle of incidence, and we can represent the susceptibility by a simple scalar number.

The higher-order terms of the material electric susceptibility give rise to various nonlinear optical processes which have important technological applications. Our aim here is not to present an exhaustive review of nonlinear optics, but to summarize those who are relevant to this work. To this end, we do not discuss second-order nonlinear processes in detail (since the materials used in this work are centrosymmetric). We focus our discussion of $\chi^{(3)}$ processes on the general case of four-wave mixing, and the specific examples of third-harmonic generation and the optical Kerr effect. We also briefly discuss non-parametric third-order effects.

Four-wave mixing : third harmonic generation and optical Kerr effect

In equation 2.30, the different electric fields in the tensor product do not necessarily have to be at the same frequency. In the most general description of a third-order nonlinear process, we consider the interaction of four waves at different frequencies [56], with the condition $\omega_1 + \omega_2 + \omega_3 = \omega_4$ enforcing conservation of energy. The third-order electric susceptibility for a given combination of frequencies is written $\chi^{(3)}(\omega_4; \omega_1, \omega_2, \omega_3)$, and the polarization at frequency ω_4 is

$$P_i^{(3)}(\omega_4) = \frac{1}{4}\epsilon_0 \sum_{jkl} \chi_{ijkl}^{(3)}(\omega_4; \omega_1, \omega_2, \omega_3) E_j(\omega_1) E_k(\omega_2) E_l(\omega_3). \tag{2.31}$$

For the wave-mixing process to occur efficiently, the waves at the different frequencies must be able to co-propagate without destructively interfering. This imposes a condition on the wavevectors known as the phase-matching condition : $\mathbf{k}_1 + \mathbf{k}_2 + \mathbf{k}_3 + \mathbf{k}_4 = 0$. In practice, this means that to realize a specific wave-mixing interaction in a given material, the frequency, propagation direction and polarization of the incident waves must be precisely tuned.

We shall consider the simplest case, where there is only one frequency in the applied electric field. We write the expression for the third-order nonlinear polarization in the time domain[2] for an applied electric field $\mathbf{E}(t) = \mathbf{E}_0 \cos(\omega t)$

$$\mathbf{P}^{(3)}(t) = \epsilon_0 \chi^{(3)}(\omega) \mathbf{E}_0^3 \cos^3(\omega t) \tag{2.32}$$

Using the trigonometric identity $\cos^3(x) = \frac{1}{4}\cos(3x) + \frac{3}{4}\cos(x)$, this becomes

$$\mathbf{P}^{(3)}(t) = \frac{1}{4}\epsilon_0 \chi^{(3)}(\omega) \mathbf{E}_0^3 \cos(3\omega t) + \frac{3}{4}\epsilon_0 \chi^{(3)}(\omega) \mathbf{E}_0^3 \cos(\omega t) \tag{2.33}$$

The first term corresponds to the generation of third-harmonic radiation at 3ω, in the four-wave mixing notation : $(3\omega; \omega, \omega, \omega)$. The second term is equivalent to a modulation of the linear susceptibility by an amount $\frac{3}{4}\chi^{(3)}\mathbf{E}_0^2$. The generated wave has the same frequency as the incident wave : $(\omega; \omega, -\omega, \omega)$.

The intensity-dependent modulation of the susceptibility is known as the optical Kerr effect, and is commonly described as a modulation of the refractive index :

$$n(I) = n_0 + n_2 I \tag{2.34}$$

where n_2 (known as the nonlinear refractive index or Kerr coefficient) is given by

$$n_2 = \frac{3\chi^{(3)}}{4n_0^2 \epsilon_0 c} \tag{2.35}$$

An important consequence of the Kerr effect is self-focusing of light beams in $\chi^{(3)}$ materials. The spatial intensity profile of a light beam (typically, a Gaussian distribution) causes a spatial variation of the refractive index, which acts as a lens. This can either focus or defocus the beam depending on the sign of n_2.

[2]Here, we can use the time-independent susceptibility $\chi(\omega)$ because we are assuming a monochromatic, continuous excitation.

In the case of a positive Kerr coefficient, the self-focusing of the beam increases the peak intensity, further increasing the refractive index modulation. This can lead to a waveguiding effect allowing diffractionless propagation or to a runaway self-focusing which increases the peak intensity above the damage threshold of the material. The optical Kerr effect and Kerr self-focusing are the fundamental nonlinear processes underpinning the experiments and simulations described in Chapter 5.

Non-parametric $\chi^{(3)}$ processes : saturable and two-photon absorption

All the nonlinear interactions described so far were parametric processes, defined as interactions that do not involve real optical transitions in the material, and so do not describe the absorption of radiation. They relate to the real part of $\chi^{(3)}$. However, the third-order susceptibility can also have an imaginary part, describing changes in absorption proportional to the intensity.

As the absorption of light by a material is accompanied by a transition from the ground state to an excited state, if the intensity of the light is sufficiently increased, eventually the ground state population will be depleted and the probability of absorption will decrease. This effect is known as saturable absorption, and the intensity-dependent absorption is expressed

$$\alpha(I) = \frac{\alpha_0}{1 + I/I_s} \tag{2.36}$$

where α_0 is the linear absorption and I_s is the saturation intensity at which the absorption is reduced by half.

Two-photon absorption (2PA) is another process modulating absorption as a function of light intensity, in the opposite direction. If the intensity is sufficiently high, a transition at frequency 2ω can be excited with light at a frequency ω, by the simultaneous absorption of two photons. The intensity-dependent absorption for 2PA follows the form

$$\alpha(I) = \alpha_0 + \beta I \tag{2.37}$$

where β is the 2PA coefficient.

Saturable and two-photon absorption can both be present in the same material and one or the other can dominate the nonlinear absorption depending on the wavelength and intensity [57]. This is the case in the carbon nanotube thin films used in our experiments [58]; measurements of the saturable and two-photon absorption are discussed in section 3.2.4 and 5.1.2.

In this overview, we have only discussed the cases of continuous-wave excitation. There are also nonlinear optical effects that occur specifically with ultrashort light pulses, such as self-phase modulation leading to supercontinuum generation, and the formation of solitons.

2.4 Carbon nanotube exciton-polaritons

Optical microcavities reaching the strong coupling regime with semiconducting carbon nanotubes were first demonstrated in 2016 by Graf et al. [46]. The cavities used metal mirrors and (6,5)CNT:PFO-BPy thin films at concentrations ranging from 0.20%wt to 1.71%wt. Angle-resolved reflectance measurements confirmed the strong-coupling regime by a clear anticrossing of the exciton and cavity mode dispersions, with fitted Rabi splitting between 34meV and 112meV. Angle-resolved photoluminescence showed emission from the lower polariton branch, and no emission at the bare exciton energy. The angular distribution of the emission for some values of coupling and detuning suggested the existence of a polariton relaxation bottleneck. Due to the roughness of the top cavity mirror (evaporated directly on the CNT film surface), the polariton quality factor was limited to 23.

Soon after, the same group demonstrated the electrical pumping of polaritons using a light-emitting field-effect transistor structure embedded inside a metal-mirror microcavity. Angle-resolved reflectance measurements without applied bias to the contacts confirmed the strong coupling regime, with a Rabi splitting of 127meV. Under optical pumping, the cavity showed polariton photoluminescence emission similar to what was observed in previous work. However, due to the integration of the field-effect transistor structure, polariton electroluminescence could also be observed. The identical energy dispersion spectrum on the electroluminescence and photoluminescence confirmed electrical pumping of exciton-polaritons. The LP occupation distribution was analyzed and found to be in thermal equilibrium, indicating efficient relaxation of the electrically-pumped polaritons. By varying the detuning, electroluminescent emission could be tuned from 1060 to 1530nm. The external efficiency of the device was quite low (on the order of 10^{-4}), which was explained by the low PLQY of the films (measured at 0.17%) and the scattering losses limiting the polariton lifetime. The dependence of electroluminescence intensity on detuning showed a maximum at -160meV, and decreased at larger negative detunings. This suggests that radiative pumping might not be the dominant mechanism for polariton population, and that exciton-phonon scattering involving the D-band phonon at 160meV could play a role.

The field-effect transistor structure also allowed the modulation of the Rabi splitting by electrical doping. When a negative voltage was applied to the top gate, an excess of holes accumulated in the channel, which bleaches the S_{11} exciton transition. By modulating the gate voltage, a transition between the weak and strong coupling regimes could be observed.

Möhl et al. further explored the idea of CNT doping in the strong coupling regime [59]. A gold-mirror cavity (one of the mirrors also acting as a working electrode) filled with a dense (6,5)CNT:PFO-BPy film was connected to a film of metallic CNTs acting as a counter electrode, with an ion gel electrolyte covering the two films. An applied voltage between the electrodes doped the (6,5)CNTs with holes, which formed trions (charged excitons). Angle-resolved reflectance showed the expected lower and upper polariton modes, with the apparition of an additional mode in the polariton dispersion when the potential was applied. This was attributed to the strong coupling of trions with the cavity mode. The photoluminescence emission intensity was reduced in the doped case, but the angular distribution of the intensity suggested a more efficient relaxation in the doped case, as more of the total intensity was concentrated near $k_{\|} = 0$.

Gao et al. demonstrated metal-mirror CNT polariton cavities using dense aligned CNT thin films [60]. Due to the strongly anisotropic transition dipole moment of the exciton in CNTs, the use of aligned films concentrated all of the oscillator strength in one direction. This allowed the tuning of the light-matter interaction from the weak to the ultrastrong coupling regime (up to a Rabi splitting of 329meV) by rotating the polarization of the incident light. An angle- and polarization-resolved transmission measurement showed a parabolic mode dispersion when the polarization was perpendicular to the CNT axis, and a splitting of the mode into upper and lower polariton branches for the parallel polarization. The use of aluminium mirrors with good reflectance at 560nm allowed the observation of strong coupling of the S_{22} exciton transition. The complete two-dimensional energy surface of the cavity modes showed the continuous transition from weak to ultrastrong coupling, with exceptional points connecting the lower and upper polariton surfaces.

Lüttgens et al. [61] measured the PL emission of microcavities containing unmodified CNTs and CNTs functionalized with luminescent sp^3 defects which shifted the S_{11} PL emission peak while leaving the absorption essentially unchanged. This allowed them to compare the exciton population for cavities with the same detuning but a different spectral overlap between the exciton emission and LP absorption spectra. The results show a 10-fold enhancement of polariton occupation with the luminescent defects, in the detuning range where they are well-matched to the LP energy. This is strong evidence that radiative pumping is the dominant mechanism for polariton population from the exciton bath in CNT microcavities.

Additionally, time-resolved measurements showed no significant change in polariton emission lifetime between the unmodified and functionalized CNTs, ruling out vibrationally-assisted scattering as a significant polariton populating process. The PL lifetime was also unaffected as the LP mode was tuned to resonance with a weakly-coupled transition, showing that Purcell enhancement by the LP mode does not occur, and cannot explain the observed increase in PL emission intensity, which must be attributed to the relaxation of occupied polariton states.

CHAPTER 3 STRONG AND ULTRASTRONG COUPLING IN CNT MICROCAVITIES

In this chapter, we describe the methods used for the design, fabrication, and characterization of carbon nanotube-filled optical microcavities. We discuss the measurement of linear optical properties of both the constituent thin films and the fully-assembled cavities and show that by using high-concentration nanotube films, the ultrastrong coupling regime can be attained, and we observe strong coupling of the cavity mode with a phonon-assisted transition.

3.1 Microcavity design and fabrication

For the experimental results discussed in Chapters 3-5, all samples were fabricated by Dr. Abitha Dhavamani in the group of Dr. Michael S. Arnold at the University of Wisconsin-Madison (UWM). She performed the chiral purification of CNTs, the fabrication of drop-cast and vacuum-filtered CNT films, and the lamination of microcavities. To provide context for the results discussed in this work, the fabrication methods from Dr. Dhavamani's publications [45] and dissertation [62] are summarized below.

3.1.1 CNT purification and film fabrication

The CNTs used in all samples during the project were commercially sourced (CoMoCAT SG65i, Sigma-Aldrich) and were purified using a selective solubilization method [63] [46] with the polymer poly[(9,9-dioctylfluorenyl-2,7-diyl)-alt-co-(6,60-(2,20-bipyridine))] (PFO-BPy). This polymer wraps selectively around the (6,5) chirality of CNTs, allowing them to remain in dispersed in solution while other CNT chiralities aggregate into bundles which can be removed by ultracentrifugation.

CNT chirality purification

The mixed-chirality CNT starting material is dispersed by tip sonication in a solution of PFO-BPy in toluene. The resulting suspension is then centrifuged at high speed for a short time (300,000g for 10 minutes) which precipitates all the undesired-chirality CNTs, and the

supernatant is then filtered (PTFE membrane, 5μm pore size) to remove residual impurities.

The toluene solvent is removed from the supernatant by rotary evaporation. After solvent removal, the solid residue contains almost exclusively PFO-BPy-wrapped (6,5) CNTs and excess PFO-BPy polymer. For the fabrication of high-density CNT films, the excess polymer concentration must be reduced as much as possible. This is done by redispersing the CNTs in hot tetrahydrofuran (THF) followed by centrifugation at moderate speed for a long time (50,000g for 24 hours) to precipitate the purified (6,5) CNTs and leave excess polymer dissolved in the supernatant. The CNT pellet is redispersed in fresh THF and the CNT to PFO-BPy ratio is checked by optical absorbance spectroscopy. The centrifugation/redispersion in fresh solvent is repeated until the absorbance measurement shows a wrapping polymer to CNT mass ratio close to one, indicating minimal remaining excess polymer. A final centrifugation isolates the CNTs, which can be redispersed in o-dichlorobenzene (ODCB) or toluene at the desired concentration to produce a "CNT ink" for the preparation of thin films.

Thin film fabrication

Two different methods were used for CNT thin film fabrication : drop-casting and vacuum filtration.

For drop-casting, a micropipette is used to deposit calibrated volumes of CNT ink in ODCB on a glass substrate. The ink is then allowed to dry in ambient conditions. The resulting films are initially very non-uniform, with a rough thick spot at the center. The surface quality is improved by soaking in hot solvent baths (toluene followed by isopropanol) to remove polymer residue and reduce surface roughness, thereby producing a relatively uniform thickness across the width of the substrate (Figure 3.1a). By varying the concentration and volume of CNT ink used, the film thickness could be varied from 10nm to 150nm. The upper bound on film thickness is determined both by the maximal concentration of the CNT ink before the solution becomes unstable and precipitates, and by the maximum volume that can be supported by the substrates before the ink spills over the edge. The maximum CNT concentration that could be obtained in drop-cast films was 43% CNT by weight. This is the concentration that was used for the fabrication of CNT microcavities.

For vacuum filtration, the CNT ink is prepared in toluene, sonicated for two minutes, and pre-filtered through a PTFE membrane with 10um pore size to remove aggregates. Then, a calibrated volume of this particle-free CNT ink is filtered at a controlled flow rate (using a vacuum pump) through a mixed cellulose ester (MCE) membrane with a pore size of 25nm placed on a corrugated glass filter. This allows for the toluene to flow through, leaving the CNTs to be collected on top of the membrane to form a dense film. The thickness and uniformity of the film are dictated by the concentration of the CNT ink, the filtration flow rate, and total filtration volume. After the desired volume of CNT ink has flowed through, the membrane (holding the CNT film) is removed from the corrugated glass and placed carefully on the desired substrate with the CNT film facing down. It is then wetted with a drop of isopropanol and soaked in hot acetone vapours. This dissolves the MCE membrane, leaving the transferred CNT film adhered to the target substrate (Figure 3.7b).

The vacuum-filtered CNT films have a diameter of 13mm fixed by the size of the MCE membrane. When transferred onto larger substrates, this leaves a CNT-free region which can be used for baseline measurements or (in the case of microcavities) to compare measurements of a "loaded" and "unloaded" cavity with identical parameters except for the presence of CNTs. Using the vacuum-filtration method, films with thicknesses from 10 to 100nm were obtained, with a very high concentration of 63% CNT by weight. A disadvantage of the vacuum-filtration method is that the prefiltration step (required to remove aggregated CNT bundles and obtain a smooth uniform film) removes part of the CNTs from the solution, which changes the final thickness of the films for a given filtration volume. The amount of CNTs removed by the prefiltration step cannot be calculated, making it difficult to fabricate vacuum-filtered films with reproducible thicknesses. The CNT film may also develop wrinkles and tears during the transfer from the MCE membrane to the target substrate, which limit the usable area for measurements.

The first experiments were performed using drop-cast films. This was later changed to vacuum-filtered films for two reasons : first, it allowed higher CNT concentration in the final films, and second, it allowed the use of a non-chlorinated solvent for the CNT ink preparation, which reduced trion absorption and improved the long-term stability of optical properties (this is discussed in more detail in the "Absorbance spectroscopy" section below). Both methods produce dense CNT films which are mostly aligned within the substrate plane but otherwise randomly oriented (Figure 3.7c) with a surface roughness of about 2nm [62].

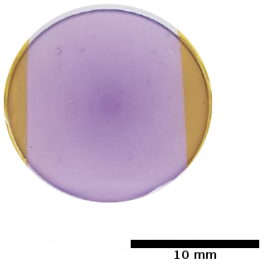

(a)

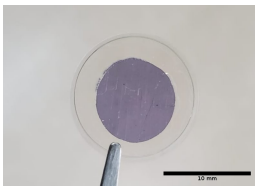

(b)

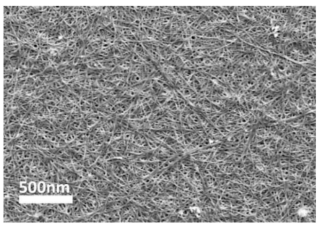

(c)

Figure 3.1 (a) CNT film fabricated by drop-casting. (b) CNT film fabricated by vacuum filtration. [Image credit Abitha Dhavamani] (c) Scanning electron microscope image of a drop-cast CNT:PFO-BPy film, showing the random in-plane alignment of the nanotubes and the high surface roughness. Reproduced with permission from [62], Copyright 2024 by Abitha Dhavamani.

3.1.2 Microcavity fabrication

With microcavities fabricated in the conventional "bottom-up" manner, where the bottom mirror, semiconductor layer, and top mirror are grown sequentially on a single substrate, the maximum concentration of CNTs that can be used is limited by the surface roughness of the CNT film. At concentrations above a few percent, the surface roughness causes significant scattering losses in the top mirror grown on top of the CNTs. This suppresses the quality factor of the cavity mode and leads to very short polariton lifetime.

The key innovation that enabled the use of highly-concentrated CNT thin films in microcavities while maintaining a high quality factor was the lamination process, using two pristine mirrors on separate substrates and a polyvinyl acetate (PVAc) bonding layer. This process was developed at UWM and used for all the microcavities fabricated during the project.

Prior to cavity fabrication, high-quality mirrors are grown on glass substrates. From the batch of pristine mirrors, one is used as the bottom mirror on which the CNT layer is deposited using the drop-casting or vacuum-filtration methods discussed previously. A PVAc film is then spin-coated on top of the CNT film. The PVAc film has three purposes : it smooths out the rough surface of the CNT film, it serves as a spacer layer to tune the cavity mode energy, and it acts as a bonding layer to attach the top mirror. A second pristine mirror is also spin-coated with PVAc to be used as the top mirror.

The bottom and top mirrors are then laminated together in a heated press (12 MPa pressure at 100C) to bring the PVAc films to their glass transition temperature, where the polymer flows to fill any gaps and permanently bond the two substrates together. This method has been successfully employed to fabricate both metal-mirror and dielectric-mirror microcavities incorporating high-concentration CNT films (Figure 3.2) without introducing excess mirror scattering losses.

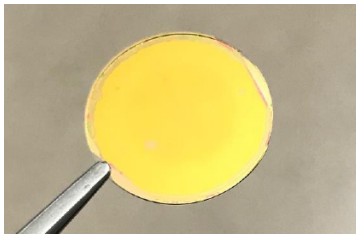

(a)

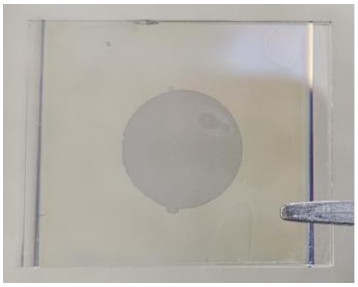

(b)

Figure 3.2 (a) Laminated gold-mirror microcavity with drop-cast CNT film. (b) Laminated DBR-mirror microcavity with vacuum-filtered CNT film. [Image credit Abitha Dhavamani]

3.1.3 Transfer-matrix modelling and optimization of cavity design

Prior to fabrication, the microcavity design is modelled using the transfer-matrix method to produce simulated reflection, transmission and absorption spectra for a range of incident angles. The angular dispersion of the polariton modes in the simulated spectra is then fitted to a coupled-oscillator model (see section 2.1.3) to extract detuning and Rabi splitting values. The cavity design can then be optimized to improve key metrics such as the quality factor and Rabi splitting, and adjust the detuning to the target value for the planned experiments.

The transfer-matrix method

The transfer-matrix method (TMM) is a widely-used tool for modelling the optical response of multilayer structures [64]. The electric field at the input and output of the structure is represented as two-component vectors consisting of the complex amplitudes of the forward- and reverse-propagating waves. The structure under study is represented as a 2x2 matrix transformation acting on these vectors.

This transformation (the "transfer matrix") is computed by simple matrix multiplication of the characteristic transfer matrices of each individual layer and interface, derived from the Fresnel equations for the complex reflection and transmission coefficients. These characteristic transfer matrices are defined in terms of the layer thickness and refractive index, the polarization, the wavelength, and the wavevector (or equivalently, the incidence angle). From the transfer matrix of the entire structure, the transmission and reflection coefficients can be easily calculated, and the absorption coefficient is known from energy conservation ($A = 1-R-T$). In order to simulate the angle-resolved spectra of a multilayer structure, the transfer matrix must be computed for a range of wavelengths and angles, and the transmission or reflection coefficient calculated from the transfer matrix elements for each point λ, θ. Examples of TMM-calculated angle-resolved reflectance spectra for a polariton microcavity are shown in Figure 3.4. The energy dispersions on the LP and UP modes that were derived in Chapter 2 are clearly recognizable in the TMM simulations.

From partial transfer matrices (that is, transfer matrices computed up to the j-th layer), the complex amplitude of the forward and back-propagating waves at each interface can be known, and the electric field amplitude profile along the propagation direction can be calculated. Knowledge of the cavity mode electric field profile is useful when trying to optimize light-matter coupling, as the overlap of the semiconductor layer with the cavity mode field can be maximized by adjusting the thickness of spacer layers (see section 3.4). An example of a simulated electric field profile is shown in Figure 3.3.

For the computation of angle-resolved spectra, the `tmm` open-source Python package by Steven Byrnes [65] was used. For calculation of the electric field profile, a MATLAB code was developed following the derivation in [64].

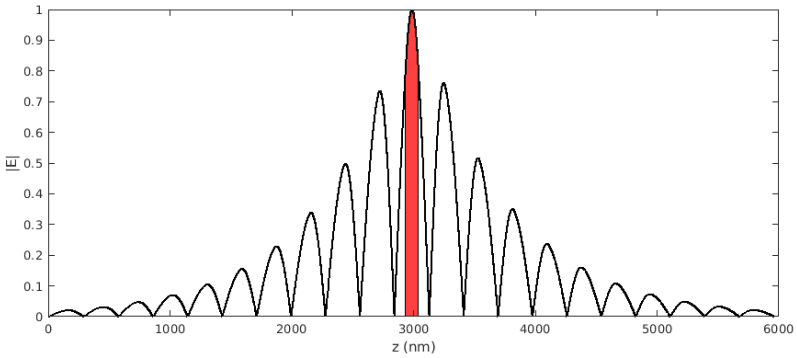

Figure 3.3 Electric field amplitude profile computed using TMM, for a 10.5-pair DBR cavity using symmetrical spacers to optimize the overlap of the CNT layer (in red) with the cavity mode electric field.

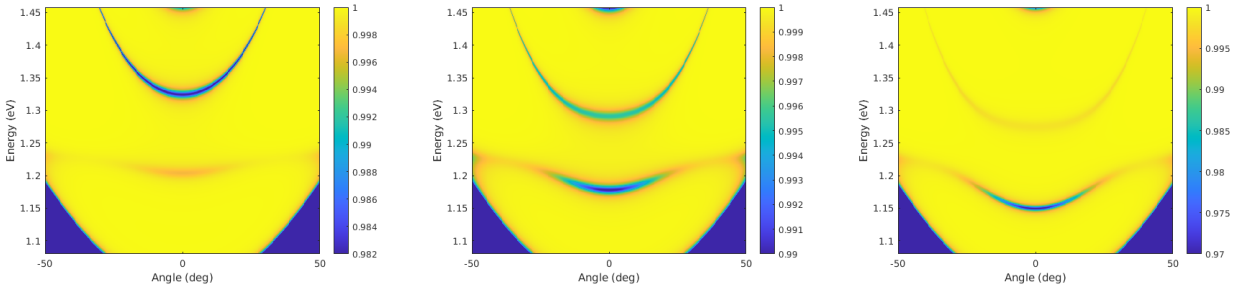

(a) (b) (c)

Figure 3.4 TMM-calculated angle-resolved reflectance spectra of a DBR-mirror cavity in the strong-coupling regime, with different spacer thicknesses to adjust the cavity-exciton detuning. (a) Positive detuning regime. (b) Near-zero detuning regime. (c) Negative detuning regime. The features at high angle and low energy are the DBR mirror sidelobes.

Extraction of polariton parameters from TMM-simulated spectra

From the angle-dependent spectra calculated from TMM, the angular dispersion of the LP and UP mode energy can be extracted by fitting Lorentz lineshapes to the spectra (when the mode occurs close to the edge of the DBR stopband, adding an exponentially decaying background terms can be required). The energy dispersion can then be fitted to the coupled oscillator model to obtain the polariton parameters Δ and Ω_R, the exciton-cavity detuning and Rabi splitting. For example, in Figure 3.5 we show the results of fitting the coupled-oscillator model on the angle-resolved reflectance spectra of Figure 3.4.

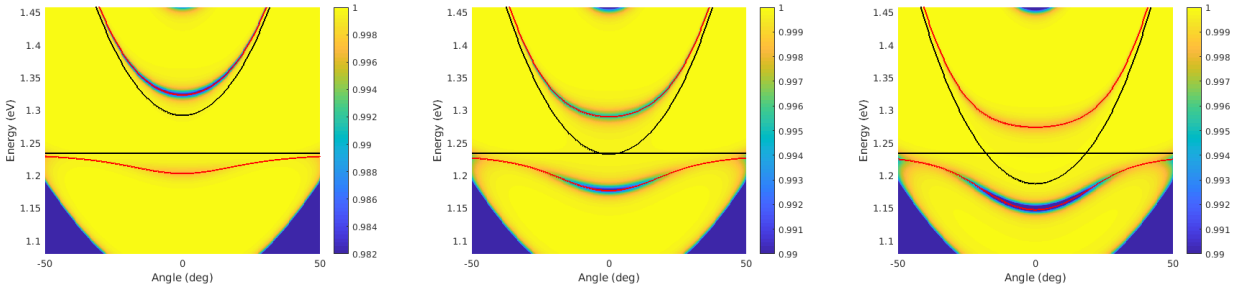

(a) $\Delta = 58\,\text{meV}$, $\Omega_R = 53\,\text{meV}$ (b) $\Delta = -2\,\text{meV}$, $\Omega_R = 57\,\text{meV}$ (c) $\Delta = -47\,\text{meV}$, $\Omega_R = 59\,\text{meV}$

Figure 3.5 Coupled-oscillator model fit (red) to the TMM-calculated angle-resolved reflectance spectra of Figure 3.4. The fitted bare exciton energy and cavity mode dispersion are also shown (black).

This workflow (TMM simulation of the angle-resolved spectra followed by fitting the simulated spectra to the polariton mode energy dispersion model) was used not only for simulating cavity designs prior to fabrication, but also for modelling fabricated cavities after characterization, using measured values of the layer thicknesses. This is discussed in more detail in section 3.2.7.

3.2 Characterization

3.2.1 Microscope images

To assess CNT film morphology and surface quality, as well as diagnose adhesion issues in laminated microcavities, most samples received from UWM were first photographed under 4X to 50X magnification in the same microscope that is used for angle-resolved spectroscopy measurement. Two imaging modes were used : bright-field transmission and dark-field scattering microscopy.

In the bright-field imaging mode (Figure 3.6a), white light from a halogen lamp is focused on the sample at normal incidence, and the transmitted light is collected by the imaging objective. Differences in absorption are clearly visible, which allows the visual assessment of the uniformity of the CNT layer (Figure 3.7). Defects such as CNT aggregates or cracks are also easily detected. However, pinholes in the transparent layers of the cavity or air gaps due to poor adhesion between substrates are not easily detected in brightfield imaging.

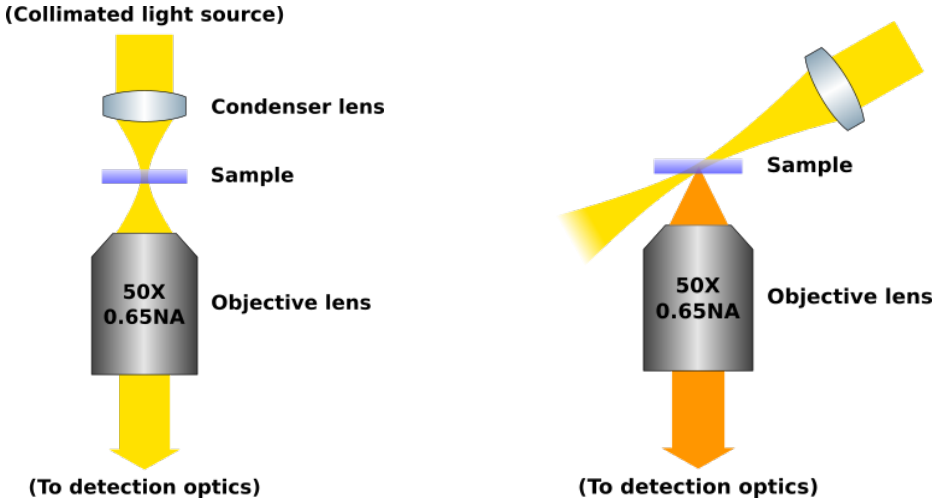

(a) (b)

Figure 3.6 (a) Illumination setup for bright-field transmission microscopy. The illumination light is focused on the sample at normal incidence by a condenser lens, and the transmitted light is collected by the microscope objective. (b) Illumination setup for dark-field scattering microscopy. The illumination light is focused on the sample by a condenser lens with a long focal length (to reduce the angular spread of illumination) and incident at a grazing angle. The transmitted light (yellow beam) is not collected by the microscope objective, but part of the light scattered by defects or sharp features in the sample (orange beam) lies inside the objective's acceptance angle and is collected.

In the dark-field imaging mode (Figure 3.6b), the white light source is collimated and incident on the sample at a grazing angle, such that only scattered light, and no directly transmitted light, is detected. Any small cracks or pinholes in any layer of the cavity appear as bright spots on a dark background, and air gaps from incompletely laminated regions appear as bright areas (Figure 3.8). The dark-field imaging mode was extensively used throughout the various experiments performed with the CNT cavities, in order to align the optical pump or probe spot with a clean, defect-free location in the sample.

The bright-field and dark-field microscopy images illustrate one of the difficulties of working with high-concentration CNT films; even the best film that were fabricated had many tears, pinholes, wrinkles and other defects. This limits the size of the optical probe spot that can be used, as the probe cannot be allowed to overlap with defects which scatter and absorb the probe light, introducing artifacts in the angle-resolved spectra.

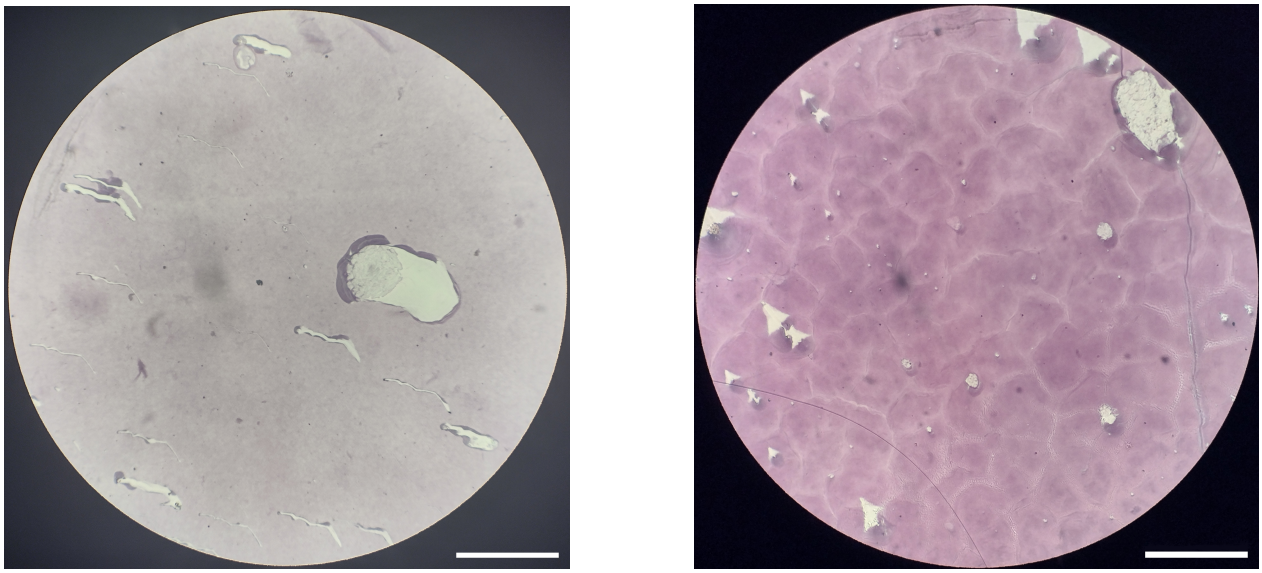

(a) (b)

Figure 3.7 (a) Bright-field transmission image of a good-quality vacuum-filtered CNT film. Some tears and pinholes in the film are visible, as well as CNT aggregates. The film thickness does not change noticeably over the field of view, giving the film an uniform pale purple colour. Scale bar 100μm. (b) Bright-field transmission image of a poor-quality vacuum-filtered CNT film. The film thickness is uneven, with thick spots appearing a darker purple color. Pinholes and tears are also present. Scale bar 100μm.

Thickness non-uniformity also limits the size of the probe spot. CNT film thickness cannot be allowed to vary significantly over the width of the probe spot, or the measured cavity modes will appear broadened.

In practice, this means it was necessary to use a probe spot of a few μm in diameter, close to the diffraction limit. Because of this constraint, the maximum optical power that could be used to pump or probe the cavity without damaging the measurement spot was very low, and the signal at the detector was correspondingly weak. In the photoluminescence measurements discussed in Chapter 4 as well as in the nonlinear measurements discussed in Chapter 5, poor signal-to-noise ratio was a major challenge that could have been overcome by using more optical power spread over a larger spot size, if the CNT films had been more uniform.

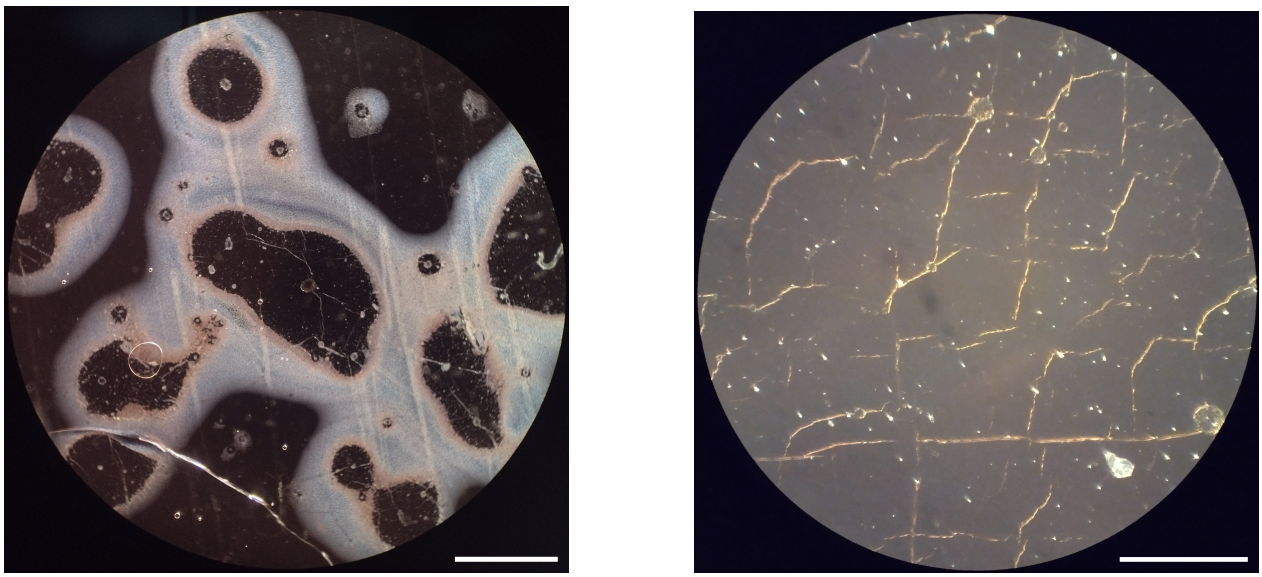

(a) (b)

Figure 3.8 (a) Dark-field scattering low-magnification image of a laminated CNT cavity with DBR mirrors. The well-laminated, defect-free regions suitable for measurement appear as uniform dark areas, while regions with incomplete adhesion between substrates appear as bright areas. Cracks and pinholes are visible as sharp bright features. Scale bar 1000μm. (b) Dark-field scattering high-magnification image of a laminated CNT cavity with DBR mirrors. This level of magnification is used during experiments to align the optical probe spot with a defect-free spot in the sample. Scale bar 100μm.

3.2.2 Absorbance spectroscopy

In addition to its use during CNT ink preparation to determine the CNT to wrapping polymer ratio, absorbance spectroscopy (using an Agilent Cary 7000 spectrophotometer)was used to assess the quality of the thin films, and as an indication of total CNT content of the film (the product of CNT concentration and film thickness). For example, to confirm that CNT films made on the same day with the same batch of ink could be considered identical, their absorption spectra were compared (Figure 3.9). We can also observe that the absorption linewidth of the S_{11} transition (FWHM = 76meV in vacuum-filtered films with 63%wt loading) is about twice as large in these highly concentrated films as what was reported for drop-cast films at $<$ 2%wt concentration [66] and nearly four times broader than dilute (6,5)CNTs in solution [46]. Broadening of the exciton transition at high concentrations is expected, as contact between nanotubes creates quenching sites which reduce exciton lifetime.

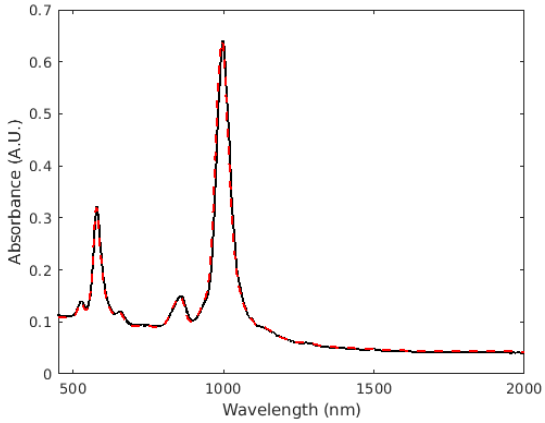

Figure 3.9 Comparison of the absorbance spectra of two vacuum-filtered CNT films fabricated on the same day, from the same batch of ink.

The absorbance spectra allowed us to identify some issues that could then be mitigated with changes to the fabrication and sample handling methods. The first issue was the high losses on the low-energy tail of the S_{11} transition at 1000nm, which has two causes : the trion absorption peak at 1150nm and a broad background from scattering losses (due to roughness of the film). These excess losses occur in the energy range where the lower polariton lies, suppressing the polariton lifetime. The issue was partially mitigated by changing the solvents used in the film processing from toluene to THF and isopropanol (Figure 3.10).

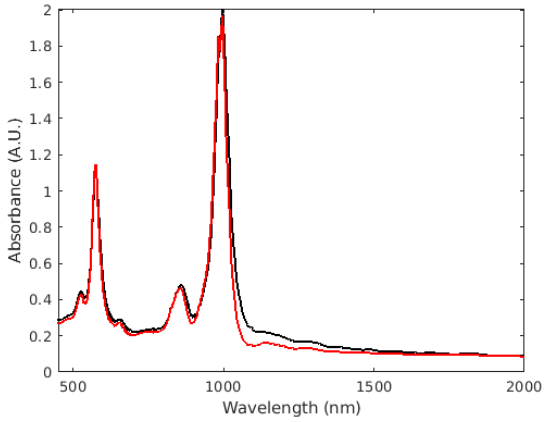

Figure 3.10 Absorbance spectra of drop-cast films made from the same ink, using a toluene soak (black) or THF and isopropanol soaks (red) for processing.

The other issue that was noticed was a gradual bleaching of the exciton transitions as the films aged, over a timescale of a few months. We determined that this was caused by oxidation from exposure to the ambient atmosphere (Figure 3.11), and solved the issue by storing all samples in a nitrogen glovebox, protected from light. However, some samples still showed signs of degradation, possibly from dissolved oxygen in the CNT ink solvents that remained trapped in the films after fabrication. This is discussed further in section 4.2.4.

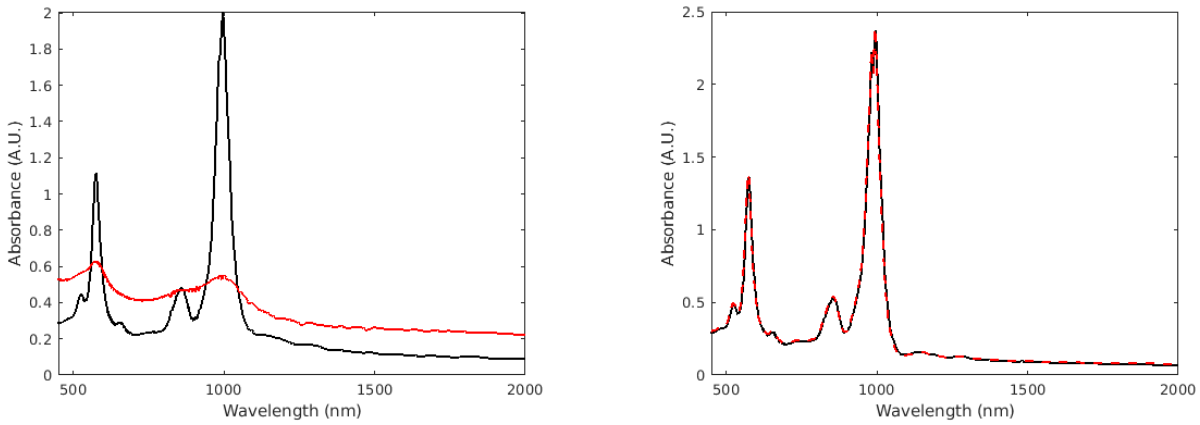

(a) (b)

Figure 3.11 Absorbance spectra of drop-cast CNT films two weeks after fabrication (black) and after 6 months storage (red). (a) Storage in ambient air. (b) Storage in dry nitrogen glovebox. In both cases, the samples were protected from light by aluminium foil.

3.2.3 Spectroscopic ellipsometry

To be able to model the cavities' optical response, and design cavities with the desired energy dispersion, it is essential to know the optical dispersion of all the materials to a high degree of accuracy. In the case of the DBR mirrors, as they were made commercially (Spectrum Thin Films, Intlvac Canada), the dispersion data from the manufacturer could be used directly. For the films fabricated at UWM (CNT, PVAc) or Polytechnique Montréal (MgF_2), it was necessary to characterize the optical dispersion. This was done using variable-angle spectroscopic ellipsometry, with a J.A. Woolam RC2 ellipsometer in the Functional Coating and Surface Engineering Laboratory at Polytechnique Montréal. The thicknesses of spin-coated and evaporated films were also measured with ellipsometry in order to calibrate the fabrication processes.

Because of variability in optical properties between different batches of CNT films, with each cavity fabrication run, a bare CNT film was also prepared for characterization. The optical dispersion for all the CNT films in that fabrication run can then be determined to a good degree of accuracy, and the cavities in the fabrication run can be modelled using the transfer-matrix method.

The variability in optical properties between different batches of films posed a significant challenge throughout the project. The cavities were designed from numerical simulations using optical dispersion data from previous fabrication runs, but the fabricated design would have slightly different CNT optical properties, and would deviate from the design. Our collaborators at the University of Madison made various improvement to the CNT purification and film fabrication processes throughout the project, but reproducibility remains low. To circumvent this issue, in each fabrication run, several cavities were fabricated with small variations in the CNT layer thickness around the design value. This increased the probability that at least one sample would be close to the simulated design.

Since the oscillator strength of the exciton transitions in CNTs is strongly anisotropic (the transition moment dipole being aligned with the nanotube axis), the optical dispersion of the CNT thin films is also anisotropic. In aligned CNT thin films, the anisotropy is biaxial, with strong absorption and dispersion only in the direction corresponding to the alignment axis [67] and negligible absorption in the two other axes. In the case of the randomly-oriented films used in our experiments, the anisotropy become uniaxial as the in-plane contributions are averaged over all CNT orientations. Note that for TMM simulations, the definitions of the characteristic transfer matrices for the CNT layer in the TM-polarized case would need to be modified to account for the optical anisotropy. However, in this work, we only consider the TE-polarized mode as it is the one with the strongest light-matter coupling. Therefore, we can use the isotropic formulation of the transfer-matrix method with the in-plane optical dispersion of the CNT layer.

In variable-angle spectroscopic ellipsometry, the sample is illuminated with a collimated beam of polarized light, and the polarization state of the reflected beam is measured. This measurement is done for a range of wavelengths and incidence angles. For each wavelength and angle, the ellipsometry data is expressed as a matrix (the Müller matrix) representing the transformation of the polarization state of the light (in the Stokes vector formalism) by the sample.

The Müller matrix elements must then be fitted with an optical dispersion model and a geometry model (number of layers present and their thickness) to extract experimentally relevant sample parameters.

For the CNT thin film samples, the model that gave the best fits was an uniaxial model. The in-plane dispersion was represented by several Lorentz oscillators to model the S_{11} transition of the (6,5) CNT chirality, its phonon sideband, and the associated trion. Additional Lorentz oscillators were added to model the S_{11} transitions of the (7,5), (8,3), and (9,1) CNT chiralities which were not fully removed by the purification process and were present as trace contaminants. A background permittivity was included in the model to account for the index of the wrapping polymer PFO-BPy, and Lorentz oscillators at zero energy and high (about 10eV) energies account for the optical transitions outside of the measured wavelength range.

The out-of-plane dispersion was represented by a similar model, with only the background terms (background permittivity, and the zero-energy and high-energy poles). The coefficients of the background terms were constrained to be identical between the in-plane and out-of-plane models.

The substrate dispersion must also be included in the ellipsometry model. A clean substrate from the same batch as the one used for the CNT thin film was measured separately on the ellipsometer, and fitted with a Sellmeier dispersion model.

In the case of highly absorbing thin films, it can be difficult to accurately determine the imaginary part of the refractive index from ellipsometry data alone, as it is correlated with film thickness in the model [68]. To mitigate this issue the ellipsometry data was first fitted in a wavelength range of 1500-2500nm, below the S_{11} transition, where the CNT film is essentially transparent. This data can be fitted with a simple isotropic Sellmeier model to extract the film thickness, which is then fixed during the fits with the complete model in the wavelength range around S_{11}. Contact profilometer measurements (Dektak XT) confirmed that the values of CNT film thickness obtained in this way are accurate.

To further improve the accuracy of the imaginary refractive index, the CNT dispersion model was simultaneously fitted to the ellipsometry data and to a normal-incidence transmission spectrum measured separately using a spectrophotometer. An example of optical dispersion obtained in this was is shown in Figure (3.12) and the corresponding fits to the ellipsometry and transmission data are shown in Figure 3.13.

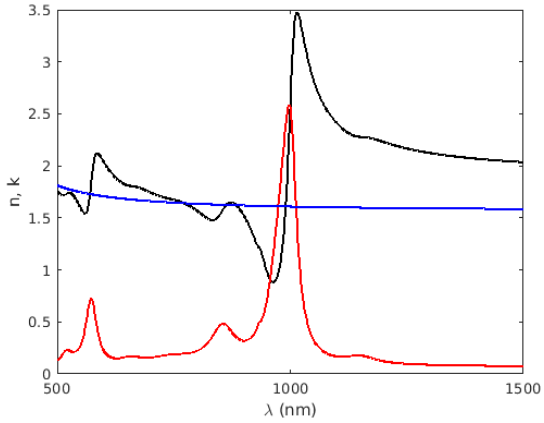

Figure 3.12 Optical dispersion of a drop-cast CNT film with a concentration of 43%wt, fitted from ellipsometry and transmission data. In-plane refractive index (black), in-plane absorption (red), out-of plane refractive index (blue).

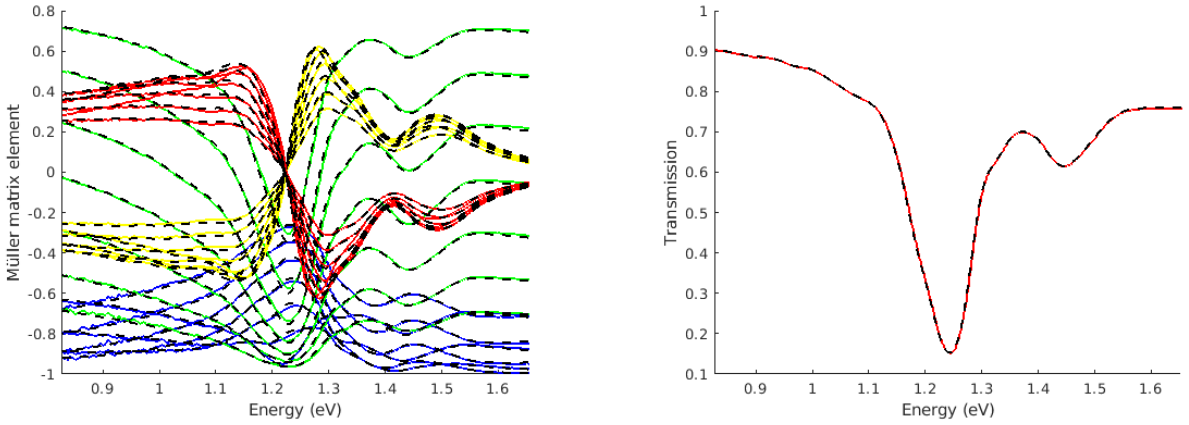

(a) (b)

Figure 3.13 Multiple Lorentz oscillator model (black dashed curve) fit to the measured (a) Müller-matrix elements at angles ranging from 45 to 75 degrees (b) Normal-incidence transmission data.

3.2.4 Nonlinear optical characterization of the CNT thin film

To support the numerical modelling of the polariton nonlinear response experiments discussed in Chapter 5, the optical nonlinear response of the CNT thin films was characterized using the Z-scan method. This is discussed in more detail in Chapter 5.

The Z-scan method is a widely-used experimental technique to characterize the refractive and absorptive nonlinear optical response of thin films [69]. A laser beam (typically a pulsed laser, in order to reach the very high peak intensity required to observe nonlinear effects) is focused on the sample with a long focal length lens. The sample is mounted on a motorized linear stage, and is translated along the beam propagation direction (crossing the focus) as the transmitted laser intensity in the far field is measured. Two measurements are done (either sequentially, or simultaneously using a beamsplitter or camera) : the open-aperture (OA) measurement records the total transmitted intensity, and the closed-aperture (CA) measurement records the intensity transmitted through a circular aperture centered on the beam.

The OA measurement is sensitive to the nonlinear absorption of the sample. As the sample approaches the beam focus, the incident peak intensity increases, which will either increase the absorption (in the case of multiphoton absorption processes) or decrease it (in the case of saturable absorption). This will be visible as a dip or a peak in the normalized OA transmission.

The CA measurement is sensitive to both nonlinear absorption and nonlinear refraction. To more clearly visualize the effect of refractive nonlinearity, the CA trace can be divided by the OA trace to factor out the contribution from nonlinear absorption. The Gaussian transverse intensity profile of the laser will cause a Gaussian modulation of the refractive index in the film, effectively forming a lens. Adding this lens in the path of the laser will change its divergence, and change the power transmitted through the aperture. For example, a positive lens placed after the beam focus will reduce the divergence, and increase the transmission through the central aperture, while a negative lens would have the opposite effect. As the sample approaches the beam focus and the peak intensity increases, the nonlinear refractive index modulation becomes larger. Note that adding a lens at the exact position of the focus does not affect the beam divergence, which is why the CA/OA trace has a value of one at the focus position $z = 0$.

The OA and CA/OA normalized transmission traces can be fitted with an analytical model [70] to extract the phase shifts $\Delta\phi$ and q_0 caused by the refractive and absorptive nonlinearity respectively. These can then be used to calculate material properties such as the Kerr coefficient n_2 and two-photon absorption coefficient β. The analytical models rely on approximations valid in the perturbative nonlinear optics regime, where $\Delta n_{NL}/n_0 \ll 1$.

In materials with a very strong nonlinear response, or when the measurement is done close to a material resonance, more complex modelling of the Z-scan data is required, using numerical beam propagation algorithms [58].

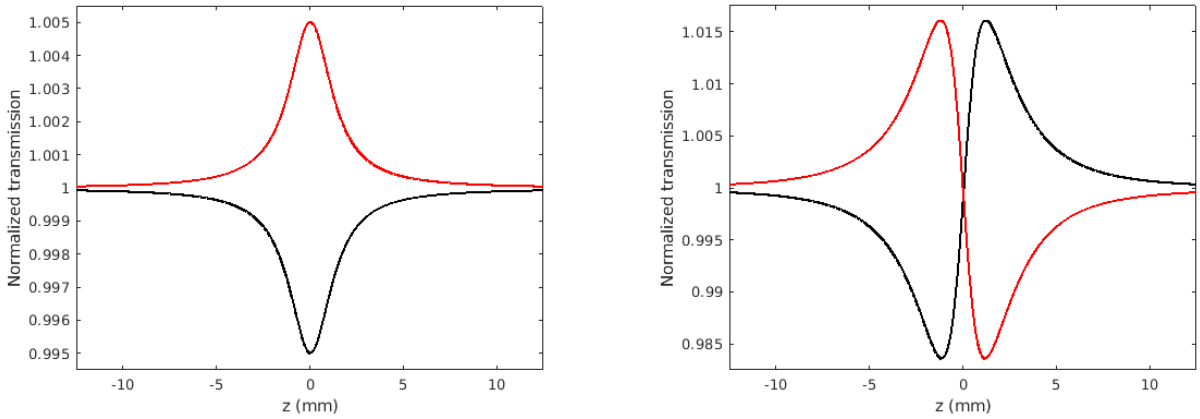

(a) OA (b) CA/OA

Figure 3.14 Example Z-scan traces. (a) Open-aperture trace for a material with $\beta > 0$ corresponding to two-photon-absorption (black) or $\beta < 0$ corresponding to saturable one-photon absorption (red). (b) Closed aperture traces for a material with a positive (black) or negative (red) Kerr coefficient n_2.

3.2.5 Micro-absorption measurement of CNT film thickness

In the case of DBR-mirror microcavities, all the materials in the structure can be considered non-absorbing, except the CNT layer. It is therefore possible to determine the CNT thickness inside the cavity from an absorption measurement. This is very useful for accurately modelling the microcavities with the transfer-matrix method.

Due to the defects that commonly occur in laminated microcavities (substrate cracking, tears and wrinkles in the CNT film), the large measurement spot size of a benchtop spectrophotometer is not suitable for this measurement, as much of the light would be scattered. Instead, we use a micro-absorption setup (illustrated in Figure 3.15) to measure the absorption in randomly selected defect-free locations in the sample, with a spot size of approximately 25 μm.

We use a 532nm laser as the probe (measuring the absorption of the S_{22} exciton transition), far outside of the stopband of the DBR mirrors. The power is attenuated to about 100μW to avoid damaging the sample. The absorption is measured in several locations and the average value is used to calculate the film thickness.

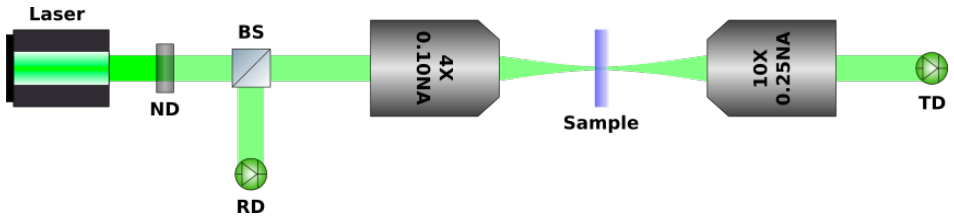

Figure 3.15 Experimental setup for the micro-absorption measurements at 532nm. ND : Neutral density filter. RD, TD : Reflected, transmitted signal detector (Si photodiode). BS : 50:50 beamsplitter.

3.2.6 Angle-resolved micro-reflectivity and photoluminescence

The main tool used to investigate the microcavities was angle-resolved reflectance and photoluminescence spectroscopy. The experimental setup was built around an Olympus IX81 inverted microscope (Figure 3.16).

Pump or probe beams are injected at the microscope back port, reflected up into the microscope objective by a beamsplitter, and focused onto the sample. Typical spot size is $2-10\mu$m. Light from the sample is collected by the same objective and focused by a tube lens, forming an image plane a few centimeters away from the microscope side port output. An iris aperture (A) is mounted at this plane to remove stray light.

Lens L1 (f=100mm), placed one focal length away from the image plane, forms a Fourier plane at a distance of one focal length on the opposite side. The Fourier plane is the spatial Fourier transform of the image plane, where position in the plane correlates with the angle of the light emitted from the sample, rather than the position from which it was emitted. Lenses L2 (f=100mm) and L3 (f=300mm) form a relay which focuses a magnified image of the Fourier plane on the spectrometer entrance slit. When L2 is removed, L1 and L3 form a relay which focuses the real-space image on the spectrometer entrance slit. L2 is mounted on a kinematic base which allows it to be moved in and out of the optical path without losing alignment, for easy switching between real-space and Fourier imaging modes.

In the space before L3, the light is always collimated whether the system is in real-space or Fourier-imaging mode. This is a convenient place to insert filters in the optical path. Usually, a linear polarizer is installed to select between measurement of the TE or TM modes of the microcavity sample. During PL measurements, a longpass filter is also installed to cut out any residual pump that was not removed by the dichroic beamsplitter.

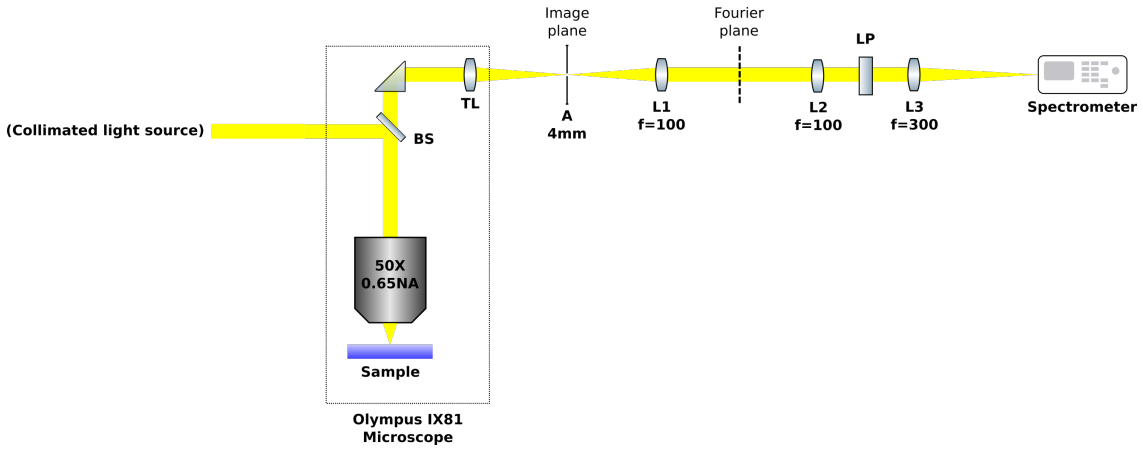

Figure 3.16 Schematic of the setup for angle-resolved reflectance and photoluminescence spectroscopy. BS:Beamsplitter. TL:Tube lens (f = 180mm). A:Iris aperture. LP:Linear polarizer. The microscope eyepiece output port and the illumination optics for bright-field/dark-field imaging are omitted for clarity.

The angle-resolved spectroscopy microscope setup can be used in different configurations (Table 3.1). During an experiment, the real-space imaging mode is typically used at the beginning to measure the pump spot size and align the pump spot. The setup is then switched to the angle-resolved spectroscopy mode for the measurement. The Fourier-space imaging mode is mostly used during setup alignment and calibration (see Appendix A).

Table 3.1 Configuration of the detection optics for the different imaging modes of the setup.

Imaging mode	Lens L2	Spectrometer slit	Spectrometer grating
Real-space imaging	Removed	Fully open	Zero-order
Real-space spectroscopy	Removed	30 μm	Target wavelength
Fourier-space imaging	Installed	Fully open	Zero-order
Angle-resolved spectroscopy	installed	30 μm	Target wavelength

Procedure for angle-resolved spectroscopy measurements

The general procedure for measuring angle-resolved spectra is outlined below. Measurements discussed elsewhere in the text will refer to this procedure, and any deviations or additions will be explained in the relevant section.

The sample is fastened with Kapton tape to a metal microscope slide with a 15mm central aperture, and loaded into the microscope sample holder. Looking through the eyepiece and using dark-field illumination, the collection objective is focused on the sample, and a suitable spot for measurement is located.

Once the sample is in focus and the microscope field of view is centered on a defect-free spot, the microscope imaging path is switched from the eyepiece to the side port output. The detection optics are then configured for real-space imaging. The white light source for dark-field illumination is switched off, and the pump (or probe, depending on the experiment) is attenuated to the lowest power possible. The shutter is opened to let the pump illuminate the sample, and the beam turning mirrors at the microscope back port are adjusted to align the pump spot with the center of the field of view on the camera. If required, a real-space image is then save to keep a record of the pump spot size.

The beam shutter is then closed, and the detection optics are reconfigured for angle-resolved spectroscopy. The pump attenuation and camera gain/integration time are set to the values required for the measurement. A background image is measured with the shutter closed, and a second image is measured immediately afterwards with the shutter opened.

For reflectance measurements, the beamsplitter below the objective is a 50:50 non-polarizing plate beamsplitter, and the light source is a fiber-coupled stabilized halogen lamp and achromatic large-beam collimator. For photoluminescence measurements, the 50:50 beamsplitter is replaced with a longpass dichroic filter with a cutoff wavelength of 600nm, and the light source is a pump laser (typically a few milliwatts at 532nm). Examples of angle-resolved spectra measured using this system are shown in Figure 3.17.

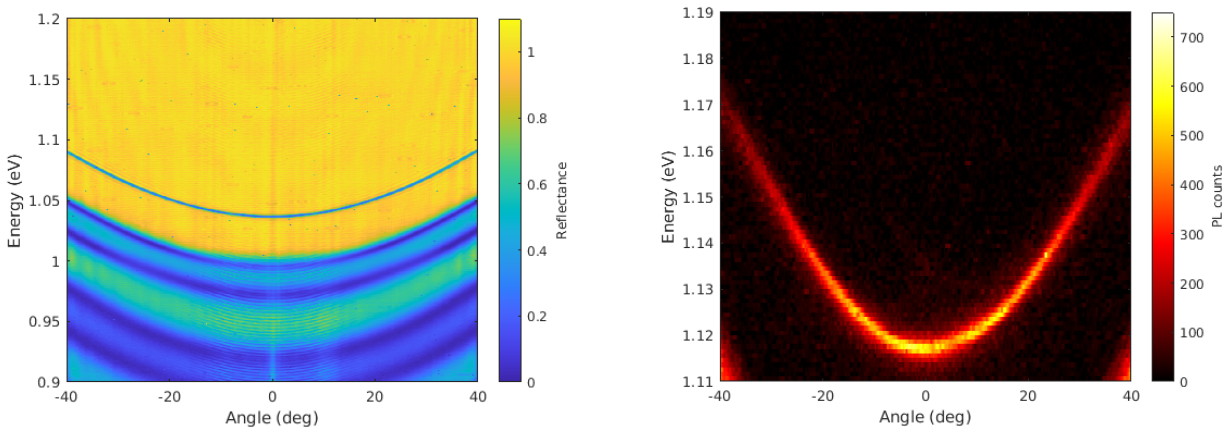

(a) (b)

Figure 3.17 Examples of angle-resolved reflectance and photoluminescence spectra measured with the Fourier imaging microscope. (a) Reflectance of a DBR unloaded cavity mode close to the stopband edge. (b) Lower polariton PL emission of a DBR cavity in the far negative detuning regime.

3.2.7 Fitting of the polariton dispersion model to angle-resolved spectra

The measured reflection spectra can be fit with Lorentz or Voigt lineshapes and the modes' energy dispersion extracted as described previously for the TMM-simulated spectra, and then fitted to the polariton energy dispersion model to obtain the Rabi splitting and detuning values.

Because we are operating the cavities in a negative detuning regime (to increase the lower polariton lifetime), the upper polariton mode contrast is very low. As a result, in most of our samples, it was not possible to resolve the UP mode in the Fourier-imaging spectroscopy measurement.

It is possible to fit the polariton dispersion model only to the lower polariton branch (if a wide enough angular range is measured to see the deviation from a parabolic dispersion at large angles), at the cost of wider confidence intervals on the fitted coefficients. For the DBR cavities, another strategy can be used, exploiting the fact that the entire cavity structure can be inferred from the linear characterization measurements. The refractive index dispersion of all materials in the cavity is accurately known from ellipsometry. The thicknesses of the DBR high- and low-index layers (and the MgF_2 spacer layer, if present) are also known from ellipsometry. The thickness of the CNT layer is known from the micro-absorption measurement. The only unknown thickness in the structure is the spin-coated PVAc spacer/bonding layer. This can be determined by fitting the measured LP energy dispersion to a TMM-simulated one, with PVAc thickness as the only free parameter.

Once this is done, the TMM model completely reproduces the cavity's angle-resolved dispersion, but can be computed to an arbitrarily high precision and without noise. Fitting the polariton energy dispersion model to the UP and LP modes in the TMM-simulated absorption spectra of the cavity then yields the Rabi splitting and detuning values with a much narrower uncertainty than fitting the LP mode alone in the experimental data. An example of the process is shown in Figure 3.18.

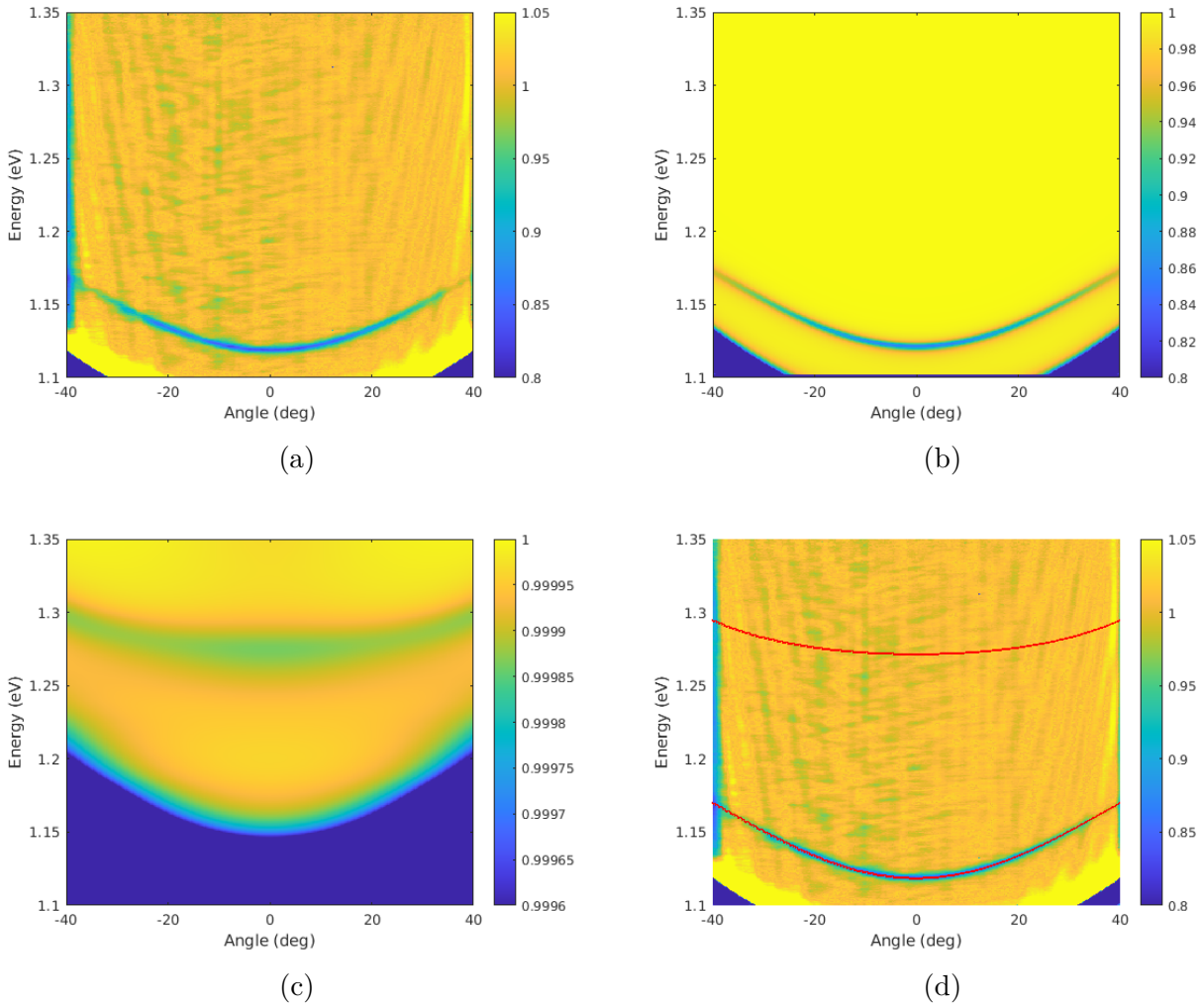

Figure 3.18 Process for fitting a coupled-oscillator model to a TMM model based on the characterization of a real sample. (a) Measured angle-resolved reflectance spectrum of a CNT DBR microcavity. Only the LP mode is visible. (b) TMM-calculated angle-resolved reflectance of the same sample, based on the measured layer thicknesses and optical dispersion of the materials. (c) When the colourscale is adjusted, the UP mode can now be resolved in the TMM simulated spectrum. (d) LP and UP dispersion fitted on the TMM data, overlaid on the original measurement. The fitted parameters are $\Delta = -90.16 \pm 0.11$meV, $\Omega_R = 61.75 \pm 0.02$meV.

3.3 Observation of ultrastrong coupling in metal-mirror CNT microcavities

Using the microcavity lamination fabrication method and the high-concentration single-chirality CNT films, metal-mirror cavities were fabricated and demonstrated record-breaking exciton-photon coupling strength for CNTs, reaching into the ultrastrong coupling regime. We also observed an additional polariton mode in the angle-resolved reflectance data, arising from the strong coupling of the cavity mode to a phonon-assisted exciton transition, and determine the coupling strength of both transitions to the cavity mode using an extended coupled-oscillator model.

The results described in this section were published in:

A. Dhavamani, L. Haeberlé, J. Wang, S. Kéna-Cohen, and M.S. Arnold, "Cavity-mediated hybridization of bright and dark excitons in an ultrastrongly coupled carbon nanotube microcavity", ACS Photonics 8, 2375–2383 (2021) Copyright ©2021 American Chemical Society. DOI : 10.1021/acsphotonics.1c00540

The fabrication and angle-resolved reflectivity measurements in the article were performed by Dr. Dhavamani. The contributions of the author to the article were : transfer-matrix modelling and design of the microcavity structure, development of the three-branch model for fitting the polariton energy dispersion, and angle-resolved photoluminescence spectroscopy measurements.

3.3.1 Samples under investigation

Four cavities were fabricated, using drop-cast films of (6,5)CNT:PFO-BPy with a concentration of 43%wt. The cavities used evaporated gold mirrors, with a 60nm thick mirror on the bottom substrate and a 30nm thick mirror on the top substrate. These values were chosen in order to optimize the polariton mode reflectance contrast when measured through the top substrate, while maximizing the quality factor. The cavities were fabricated using the lamination method described in 3.1.2. A constant thickness of 150nm was used for the PVAc bonding layer, while the thickness of the CNT layer varied from 80nm in the first cavity to 150nm in the fourth.

3.3.2 Angle-resolved reflectance measurements

The angle-resolved reflectance was measured using a J.A. Woollam V-VASE variable-angle spectroscopic ellipsometer, at incidence angles from 20 to 60 degrees. This was used instead of the Fourier-imaging microscope system because of its large detector spectral range. Due to the very large Rabi splitting of the cavities, the UP branch energy lies outside of the detectable range of the InGaAs detector in the Fourier-imaging setup. The measurement spot size when using the ellipsometer with focusing probes is approximately 500 μm, much larger than in the microscope. The large spot size combined with the non-uniform thickness of the CNT and PVAc films is expected to broaden the linewidth of the observed modes, but they remain easily resolvable. The TE polarization is used, as it provides the largest light-matter coupling.

The measured reflectance spectra (Figure 3.19) show that in addition to the expected UP and LP branches, a third peak is present, which we name the middle polariton (MP) branch. This third mode arises from the strong coupling of the cavity mode with the phonon-assisted K-dark exciton transition (see section 2.2). As the detuning is increased, we can also observe a small peak at 1010nm with a negligible energy dispersion slope, which we attribute to strong coupling of the S_{11} transition with the second-order cavity mode (this LP_2 polariton branch would have very large positive exciton-photon detuning, and therefore an almost entirely excitonic character, giving it a very high effective mass). We do not consider the LP_2 branch in our modelling.

3.3.3 Coupled-oscillator model

For modelling the light-matter coupling in these samples, we follow the same derivation as in section 2.1.3, but considering three excitations : the fundamental cavity mode with energy $\hbar\omega_c$, the S_{11} bright exciton transition with energy $\hbar\omega_1$, and the phonon-assisted K-dark exciton transition with energy $\hbar\omega_2$. In the second quantization formalism, the Hamiltonian describing the coupled cavity-exciton system is expressed

$$\hat{H} = \hbar\omega_c\,\hat{a}^\dagger\hat{a} + \hbar\omega_1\,\hat{\sigma}_1^\dagger\hat{\sigma}_1 + \hbar\omega_2\,\hat{\sigma}_2^\dagger\hat{\sigma}_2 + \hbar\Omega_1\,(\hat{a}\hat{\sigma}_1^\dagger + \hat{a}^\dagger\hat{\sigma}_1) + \hbar\Omega_2\,(\hat{a}\hat{\sigma}_2^\dagger + \hat{a}^\dagger\hat{\sigma}_2) \tag{3.1}$$

where $(\hat{a},\,\hat{a}^\dagger)$, $(\hat{\sigma}_1,\,\hat{\sigma}_1^\dagger)$, $(\hat{\sigma}_2,\,\hat{\sigma}_2^\dagger)$ are the bosonic annihilation and creation operators for the cavity mode photon, the bright S_{11} exciton and the phonon-assisted K-dark exciton respectively.

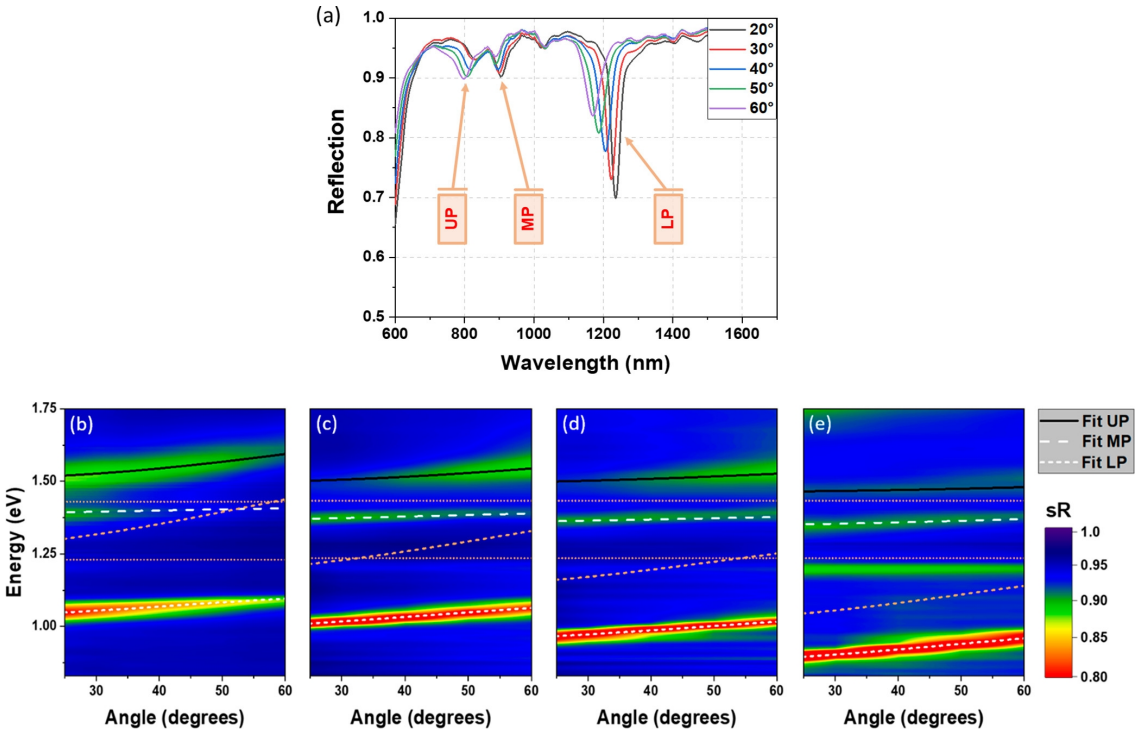

Figure 3.19 Measured angle-resolved reflectance spectra of the four gold-mirror CNT microcavities. (a) Example reflectance spectra for one of the cavities, with the three observed polariton branches labelled. (b-e) Angle-resolved reflectance of the four microcavities, from highest to lowest detuning. The bare exciton transition energies and the unloaded cavity mode dispersion are indicated with orange dashed curves, and the eigenvalues of the fitted coupled-oscillator model are indicated with the white and black curves. Reproduced with permission from [45]. Copyright 2021 American Chemical Society.

The coupling of each exciton transition with the cavity mode is parametrized by the Rabi frequencies Ω_1 and Ω_2.

In the Fock basis $|N_c, N_1, N_2\rangle$, the matrix representation of the Hamiltonian in the single-particle reduced space $\{|1,0,0\rangle, |0,1,0\rangle, |0,0,1\rangle\}$ is

$$\hat{H}' = \begin{pmatrix} \hbar\omega_c & \Omega_1 & \Omega_2 \\ \Omega_1 & \hbar\omega_1 & 0 \\ \Omega_2 & 0 & \hbar\omega_2 \end{pmatrix} \tag{3.2}$$

The angular energy dispersion of the polariton branches is obtained by diagonalizing the matrix H' to obtain the eigenvalues, with the cavity mode energy defined using equation 2.3.

To fit the coupled-oscillator model to the measured energy dispersion of the samples, the exciton transition energies $\hbar\omega_1 = 1.245$eV and $\hbar\omega_2 = 1.442$eV are fixed to the values fitted from absorbance spectra of the CNT film material. The fit parameters are the detuning at normal incidence Δ between the S_{11} bright exciton transition and the cavity mode energy, the cavity mode effective refractive index n_{eff}, and the Rabi frequencies Ω_1, Ω_2. The fitted values for the four microcavities are listed in Table 3.2.

Table 3.2 Fitted parameters of the coupled-oscillator model to the measured energy dispersion of the CNT microcavities. Reproduced (adapted) with permission from [45]. Copyright 2021 American Chemical Society.

Sample	t_{CNT} (nm)	Δ (meV)	$\hbar\Omega_1$ (meV)	$\hbar\Omega_2$ (meV)	n_{eff}
1	80	$40 \pm 1\%$	$210 \pm 1\%$	$79 \pm 4\%$	$1.80 \pm 4\%$
2	100	$-50 \pm 1\%$	$210 \pm 1\%$	$97 \pm 3\%$	$1.91 \pm 5\%$
3	138	$-120 \pm 2\%$	$220 \pm 3\%$	$106 \pm 6\%$	$1.91 \pm 9\%$
4	150	$-200 \pm 2\%$	$230 \pm 3\%$	$103 \pm 8\%$	$1.87 \pm 11\%$

We observe that the Rabi frequencies Ω_1, Ω_2 increase slightly with increasing CNT film thickness. This is consistent with the fact that light-matter coupling strength scales with the square root of the number of oscillators in the cavity, but scales inversely with the cavity mode volume. As t_{CNT} is increased, both the number of oscillators and the mode volume increase. For a completely filled cavity, these two effects would compensate exactly and the coupling strength could be independent from the detuning [14]. In our case, the cavity is not completely filled due to the presence of the PVAc bonding layer, and there is a small variation of Ω with t_{CNT}.

The ratio of the fitted Ω_1 and Ω_2 is consistent with the measured ratio of the bright S_{11} exciton transition to the phonon assisted K-dark exciton transition oscillator strengths fitted from ellipsometry and absorbance data.

The Hopfield coefficients of the polariton modes (from the eigenvectors of H') show that the LP branch is a mixed cavity photon and bright S_{11} exciton state, with negligible contribution from the phonon-assisted K-dark exciton. The MP and UP branches have significant contributions from both exciton transitions.

Finally, owing to the high CNT concentration of the thin films and the small mode volume inherent to metal-mirror microcavities, the light-matter coupling strength obtained in these samples is large, with $\Omega_1 = 230$meV and $\Omega_2 = 103$meV in the sample with the thickest CNT film. The maximal observed total splitting between the LP and UP branches was 486meV, surpassing the previous highest reported value of 329meV [60] for CNT polariton microcavities. The ratio of Rabi splitting to polariton linewidth is $2\Omega_1/\gamma_{LP} = 15.3$, showing that despite the very high CNT concentration, a good quality factor was preserved. The normalized coupling $\Omega_1/\omega_1 = 0.187$, showing that the cavity is in the ultrastrong coupling regime. This is the highest-reported value of the normalized coupling in polariton microcavities with Wannier-Mott excitons [14] [71] [60].

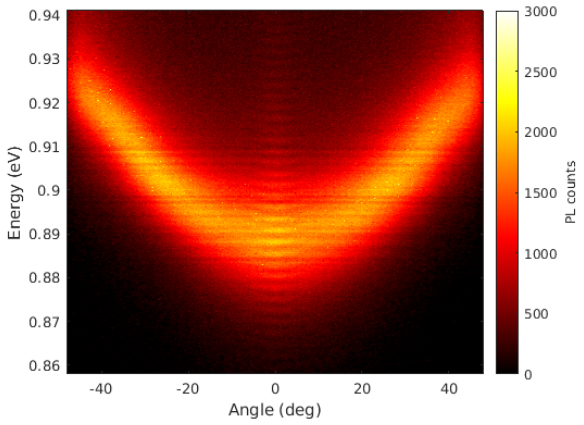

Figure 3.20 Measured angle-resolved photoluminescence spectra for microcavity # 4. The fringes near zero angle are caused by Fabry-Pérot interference between the reflections on the substrate front and back surfaces (substrate thickness 0.15mm).

3.3.4 Angle-resolved photoluminescence

The lower polariton photoluminescence emission was measured in our angle-resolved spectroscopy setup (Figure 3.20), and we confirmed that the LP energy dispersion from photoluminescence matches what was measured in reflectance using the ellipsometer. The LP emission linewidth ($\gamma_{LP} = 30$ meV) also matches the linewidth measured in reflectance. The PL emission intensity distribution is essentially uniform over the measured angular range, showing that there is no polariton relaxation bottleneck. Finally, no PL emission was observed at the MP energy, showing efficient relaxation to the LP state.

3.4 High quality factor microcavities with large Rabi splitting

The metal-mirror cavities discussed in the previous section demonstrated the possibility of reaching the ultrastrong coupling regime with high-concentration CNT films despite their inherent high surface roughness, by exploiting the lamination method developed at UWM. However, the absorption losses of metallic mirrors limit the quality factor that can be obtained, and prevent the use of high peak pump intensities. Our initial research objectives included nonlinear optical characterization of the cavities and attempting to reach the polariton condensation threshold, which would both require optical pumping with femtosecond laser pulses. For these experiments, another series of microcavities was designed, using dielectric mirrors. The design of the mirrors is a standard DBR quarter-wave stack, with 8 to 11 pairs of high- and low-index layers. The mirrors use a $N + 1/2$ pair structure (with the last layer being a high-index layer) to position the cavity mode electric field maximum at the center of the cavity structure.

Since DBR cavities have larger mode volumes than metallic-mirror cavities, the light-matter coupling strength is reduced [12]. The structure of the cavity was slightly modified to optimize the light-matter coupling, by evaporating an additional spacer layer of magnesium fluoride (MgF_2) on the bottom DBR substrate. The CNT film is deposited on the MgF_2 spacer, and the PVAc spacer/bonding layer is spin-coated on top. The top DBR substrate is then bonded to the PVAc layer using the hot press lamination process. With this "quasi-symmetrical" geometry where the CNT film is centered between two spacer layers of closely-matched refractive indices, the CNT overlap with the cavity mode electric field is maximized.

With the optimized structure and high-quality DBR mirrors, CNT polariton cavities were fabricated with $\hbar\Omega_R$ between 50meV and 100meV, detunings between -200meV and -50meV, and polariton linewidths between 2meV and 10meV. These cavities were used for CW and pulsed-excitation photoluminescence measurements (Chapter 4) and nonlinear transmission spectroscopy measurements (Chapter 5). Due to the high quality factor of the cavity mode and the non-negligible absorption losses of the CNT material, the reflectance contrast of the LP mode was much smaller in DBR DBR cavities than in the gold-mirror cavities, especially when the detuning was close to zero. This made the measurement of spectra with good signal-to-noise ratio (SNR) more challenging, and is discussed further in the relevant chapters.

CHAPTER 4 PHOTOLUMINESCENCE MEASUREMENTS ON CNT THIN FILMS AND MICROCAVITIES

In this chapter, we discuss measurements of the photoluminescence emission from CNT thin films and polariton microcavities. Using femtosecond pulse non-resonant excitation, we find no evidence of polariton condensation in the microcavities, both in ambient conditions and at cryogenic temperatures. Furthermore, we observe that polariton PL emission intensity is strongly suppressed when using a pulsed pump when compared to a CW pump of the same average power. We measure the exciton-exciton annihilation rate constant in the CNT thin film material, and find that a simple rate equation model can reproduce the fluence dependence of the PL emission intensity both in the bare films and in the polariton microcavities. Finally, we observe a rapid photoinduced degradation of the PL emission in vacuum-filtered films, while the absorption spectrum remained unchanged.

4.1 Measurement of exciton-exciton annihilation in CNT thin films

The confinement of carriers due to the one-dimensional nature of CNTs gives the excitons their high binding energy and high mobility, but also increases the probability of exciton-exciton interactions. In particular, exciton-exciton annihilation (described in Chapter 2) has been observed to be a dominant contribution to the exciton dynamics of single-walled carbon nanotubes [3] [72].

We characterized exciton-exciton annihilation in a 100 nm-thick drop-cast (6,5)CNT:PFO-BPy thin film with a mass loading of 43%. Photoluminescence emission spectra were measured under non-resonant excitation of the S_{11} exciton using 200fs pump pulses at 808nm from an optical parametric amplifier. A sequence of spectra were measured with increasing pump fluence. To verify that there was no photodegradation of the material, after each measurement, the fluence was lowered to the lowest value, and the emission spectrum was compared to the first measurement. The measured fluence range corresponds to the widest range that could be used, with the lowest value determined by the noise floor of the detector and the highest value determined by the material damage threshold.

The pump pulse creates a very high localized density of excitons "instantly" (i.e. much faster than the exciton lifetime) which can then either decay by themselves, or decay through exciton-exciton annihilation. As the pump fluence is increased, the measured PL emission saturates (Figure 4.1) as the contribution of EEA to the total decay rate increases.

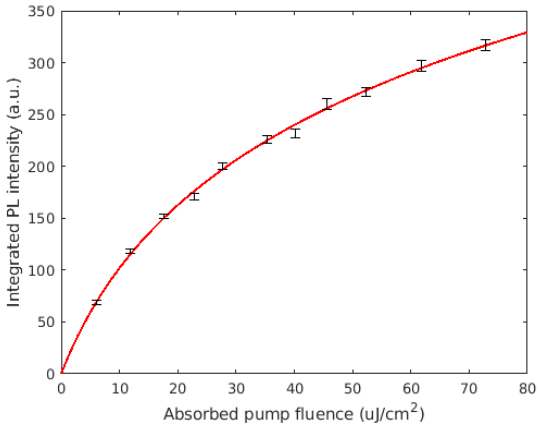

Figure 4.1 Integrated PL emission intensity as a function of pump fluence (black) and fitted rate equation model (red). The fitted EEA coefficient is $\gamma = (5.53 \pm 1.04) \cdot 10^{-8}$ cm^3/s.

Although EEA dynamics in carbon nanotubes have been described using multi-level rate equation models [3] and time-dependent annihilation rates to take into account exciton diffusion [72], we find that our experimental results are well-fitted by a simple rate equation model considering only the S_{11} exciton population, with a time-independent annihilation rate. The rate of decay of the exciton density $n(t)$ is given by the sum of the linear decay and EEA terms :

$$\frac{\mathrm{d}n}{\mathrm{d}t} = -\frac{n(t)}{\tau} - \gamma n^2(t) \tag{4.1}$$

Where $\tau = (4.19 \pm 0.11)$ ps is the linear exciton lifetime (measured from pump-probe spectroscopy of an identical drop-cast film [73]) and γ is the EEA coefficient.

The initial exciton density $n(t=0) \equiv n_0$ can be estimated from the absorbed pump photon density, making the approximation that every absorbed pump photon creates a S_{11} exciton.

$$n_0 = \frac{F_a}{\hbar\omega_p} \tag{4.2}$$

where F_a is the absorbed pump fluence and $\hbar\omega_p$ is the pump photon energy. Note that in the calculation of the absorbed pump fluence F_a, we use the linear absorption of the CNT film, without including a saturable absorption term. We do not have a measured value for the saturation intensity at 808nm for this material, but extrapolating from measurements at other wavelengths on a similar film [58] we estimate that it would be on the order of 10 GW/cm^2, while the peak intensity at the highest fluence in this measurement was 1.5 GW/cm^2.

The solution of differential equation 4.1 is

$$\frac{1}{n(t)} = \left(\frac{1}{n_0} + \gamma\tau\right) e^{t/\tau} - \gamma\tau \tag{4.3}$$

Since the detector in the experiment is much slower than the exciton dynamics, the measured signal is proportional to the total number of excitons generated from the pulse, given by the time integral of $n(t)$.

$$\mathrm{PL} \propto \int_0^\infty n(t)\,\mathrm{d}t = \frac{1}{\gamma}\log\left(1 + n_0\gamma\tau\right) \tag{4.4}$$

We find that the measured PL intensity is well-reproduced by equation 4.4, with a fitted EEA coefficient $\gamma = (5.53 \pm 0.93) \cdot 10^{-3}$ cm^2/s. This is comparable to the value reported in other low-dimensional semiconductors, for example $\gamma = 3.35 \cdot 10^{-4}$ cm^2/s in $(\mathrm{PEA})_2\mathrm{PbI}_4$ perovskite [74], $\gamma = 1.8 \cdot 10^{-3}$ cm^2/s in ZnSe/CdSe quantum wells [75], and $\gamma = 4.3 \cdot 10^{-2}$ cm^2/s in monolayer molybdenum disulfide [76].

4.2 PL of CNT microcavities

The angle-resolved photoluminescence of polariton microcavities provides complementary information to the angle-resolved reflection data discussed in the previous chapter. The polaritons decay through their photonic component, with the emitted light momentum corresponding to the polariton momentum. It follows that the photoluminescence intensity emitted at a certain angle is proportional to the population of the polariton state at the corresponding momentum (scaled by the photon fraction $|C_p|^2$ of the polariton state). Therefore, the angular distribution of photoluminescence intensity carries information about the polariton state occupation statistics. This is particularly important in the measurement of polariton condensation. The condensate state is characterized by a macroscopic occupation of the ground state, which is clearly visible in the angle-resolved photoluminescence spectra as a sharp increase in PL intensity at zero angle.

4.2.1 Steady-state photoluminescence

CW-pumped polariton PL emission spectroscopy was mostly used as a diagnostic tool to check sample quality. The defects introduced during CNT ink processing and aging of the samples after fabrication reduce the CNT exciton photoluminescence quantum yield [46]. This makes the PL intensity a sensitive indicator of sample degradation (degradation mechanisms affecting the PLQY are discussed further in section 4.2.4). However, even in freshly-prepared samples, the PLQY was very low, and required several seconds of integration with high detector gain and a strong pump to obtain spectra with sufficient SNR. The absolute PLQY of the dropcast and vacuum-filtered films was too low to be measured with the available equipment, but is likely on the order of 0.1% [54] when freshly-prepared, and degrades over time. The CW PL intensity was also used to check for spot damage after measurements, by comparing the spectra at the same sample position pre- and post-measurement. A typical angle-resolved spectrum is shown in Figure 4.2.

4.2.2 Polariton PL emission under CW and short-pulse nonresonant excitation

As one of the research objectives of the project was to demonstrate polariton condensation, most of the PL measurements performed on our microcavity samples were performed with femtosecond pulse excitation, in order to create the very high polariton densities required to reach the condensation threshold. However, with the very first measurements, we observed

that the PL emission intensity was strongly suppressed when the samples were excited with femtosecond pulses, compared with CW pumping at the same wavelength and average intensity (Figure 4.3a). This posed a significant challenge for pulsed-excitation measurements, as the PL emission intensity was already very low even in the CW case (due to the low photoluminescence quantum yield of carbon nanotubes).

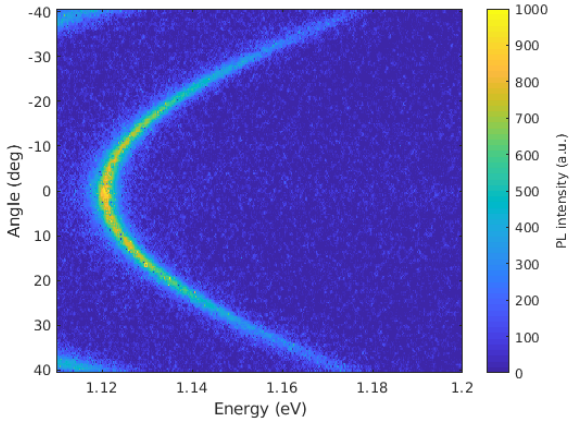

Figure 4.2 Angle-resolved photoluminescence emission spectrum of a CNT DBR microcavity under CW excitation with a 532nm laser.

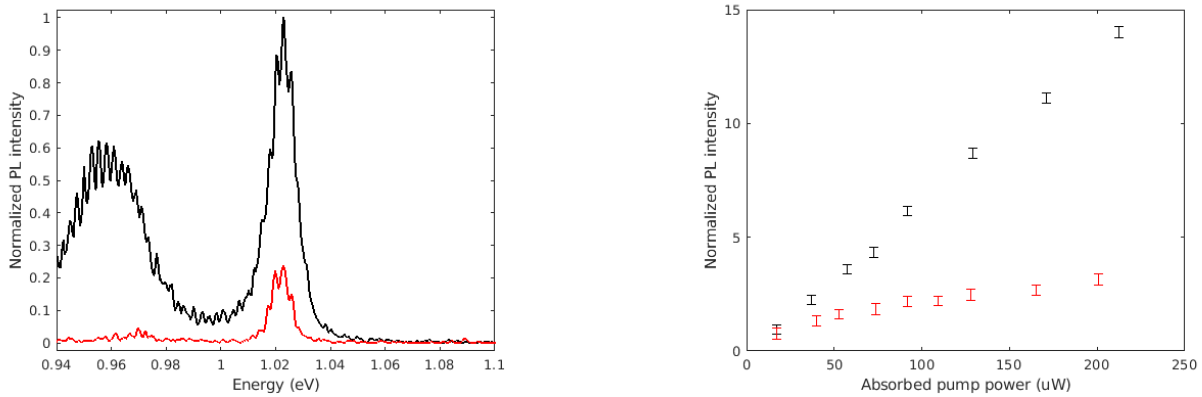

(a) (b)

Figure 4.3 Comparison of polariton PL emission between a CW pump (black) and 200fs pulses at 100kHz repetition rate (red), for the same average power, wavelength, and laser spot size. (a) PL spectrum at zero angle for an average absorbed power $P_a = 200\ \mu$W. The polariton mode is the peak at 1.02eV; the other peak is PL leakage from the DBR mirror side lobe and was not included in the calculation of integrated PL intensity. (b) Integrated PL intensity at zero angle as a function of average absorbed pump power.

The low PL emission intensity severely limited the usable range of pump fluence. In all of our samples, the difference between the lowest possible fluence that still allowed a PL signal to be measured with sufficient SNR and the onset of photoinduced damage to the measurement spot was a factor of 5-10. With such a narrow range, it is difficult to properly characterize nonlinear phenomena.

To determine whether the observed suppression of PL intensity can be explained by exciton-exciton annihilation, we calculate the ratio of exciton densities in the CW and pumped cases. In the CW excitation case, the rate equation describing the exciton density is

$$\frac{\mathrm{d}n}{\mathrm{d}t} = \frac{I_a}{\hbar\omega_p} - \frac{n(t)}{\tau} \tag{4.5}$$

where I_a is the absorbed pump intensity. We have neglected to include the EEA term in the above equation, as the exciton density under CW excitation is too low for EEA to be significant. The steady-state solution (as $t \to \infty$) is

$$n_{\mathrm{CW}} = \frac{I_a \tau}{\hbar\omega_p} \tag{4.6}$$

For an absorbed intensity of 12 W/cm^2 (corresponding to the highest-measured intensity in Figure 4.3b), the steady-state exciton density is $n_{CW} = 2.04 \cdot 10^8$ cm^{-2}.

In the pulsed pump case with the same average absorbed intensity, the absorbed fluence is 120 μJ/cm^2, and the initial exciton density is $n_0 = 4.88 \cdot 10^{14}$ cm^{-2}. Using equation 4.4 for the total exciton density generated by one pulse and multiplying by the pulse repetition rate $f_{\mathrm{rep}} = 100$ kHz, we can calculate the average exciton density generated by the pulsed pump.

$$n_{\mathrm{fs}} = \frac{f_{\mathrm{rep}}}{\gamma} \log\left(1 + n_0 \gamma \tau\right) \tag{4.7}$$

As expected, in the limit $\gamma \to 0$, the calculated exciton density is the same as that of the CW pump case. When $\gamma = 5.53 \cdot 10^{-3}$ cm^2/s, we find $n_{\mathrm{fs}} = 4.64 \cdot 10^7$ cm^{-2}. The exciton density is reduced by a factor of 4.4 compared to the CW case. This matches the experimental results of Figure 4.3, where the PL was suppressed by a factor of 4.23 ± 0.41 at the far end of the fluence range. We can conclude that the weak PL emission observed when pumping the polariton cavities with femtosecond pulses can be entirely explained by the large exciton-exciton annihilation rate in carbon nanotubes.

The experimental results in Figure 4.3 are typical of what was observed in pulsed-pump PL experiments on the CNT microcavity samples (the same saturation behaviour, low PL emission intensity, and low damage threshold were observed in cavities with various values of Rabi splitting and detuning). In all cases, the characteristic nonlinear increase in polariton PL emission intensity and narrowing of the polariton emission linewidth that occur at the condensation threshold could not be observed.

4.2.3 Cavity PL fluence dependence at low temperature

As we have seen in Chapter 2, the polariton condensation threshold is proportional to temperature. As we were unable to observe signatures of condensation in the PL emission at room temperature, we performed measurements in a closed-cycle helium cryostat (Advanced Research Systems DE-204S) at temperatures from 5K to 250K.

For practical reasons (the cryostat was not located on the same optical table as the InGaAs camera and spectrometer), the low-temperature PL measurements were not angle-resolved. Because of the minimal working distance imposed by the spacing between the sample holder and cryostat window, long focal length lenses were used for pump injection and PL collection. The pump beam (680nm, 50fs pulses, 100kHz repetition rate) was focused with a $f = 200$mm lens to a spot size of approximately 200μm, and incident on the sample at a 30 degree angle. The PL emission around zero degrees was collected with a $f = 100$mm lens, using a 12mm iris to limit the numerical aperture. The collected PL was coupled into a 400μm-core multimode optical fiber to bring the collected PL signal to the entrance slit of the spectrometer. The setup for low-temperature PL measurements is illustrated in Figure 4.4.

For 12 temperatures between 4.6K and 275K, the PL emission spectrum was measured at five different pump fluences (again, the maximum pump fluence was limited by the sample damage threshold). The lower polariton PL emission shifts to higher energy as the cavity is cooled (Figure 4.5) due to thermal contraction of the multilayer structure reducing the effective cavity length. The position of the sample drifted with changes in temperature, and it was necessary to realign the collection optics and the multimode fiber coupling every time the cryostat temperature setpoint was modified.

As a result, the absolute intensity of the measured PL can not be compared between datasets taken at different temperatures, as the collection efficiency was not the same. However, the pump power dependence of the PL intensity can be compared (since the collection efficiency does not change during the power sweep, and the pump laser spot size is unaffected by small changes in sample position).

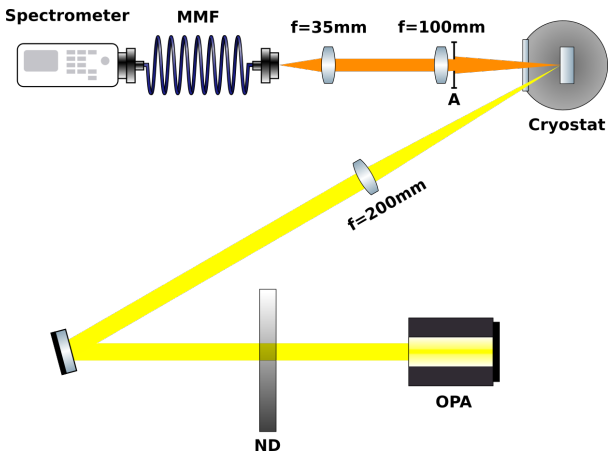

Figure 4.4 Experimental setup for low-temperature PL measurements. OPA: Optical parametric amplifier. ND : variable neutral density filter. A : Aperture. MMF : Multimode fiber.

We observe no significant changes in the pump power dependence of the PL emission intensity over the entire range of temperature from 4.6K to 275K (Figure 4.6a). We observe PL emission saturation in all the datasets, with a constant saturation power independent of temperature (Figure 4.6b). Even at the the lowest measured temperature of 4.6K, where the polariton condensation threshold is expected to be reduced by a factor of ≈ 64 compared with room temperature, there was no qualitative change to the shape of the PL emission power dependence.

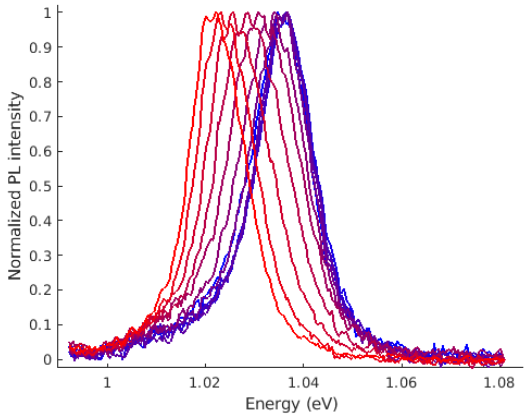

Figure 4.5 Polariton PL emission spectrum at zero angle at temperatures from 4.6K to 275K (increasing temperature from blue to red).

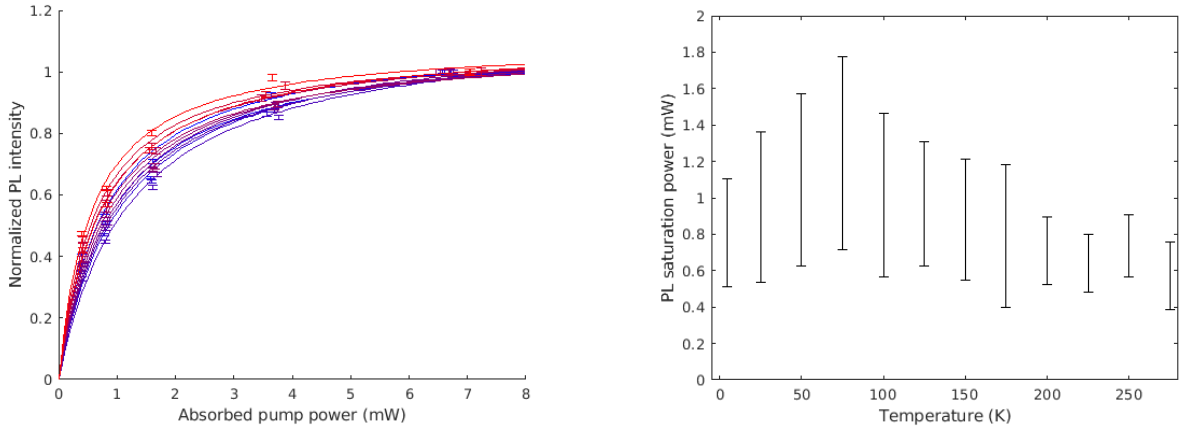

(a) (b)

Figure 4.6 (a) Power dependence of polariton PL emission intensity at temperatures from 4.6K to 275K (increasing temperature from blue to red). The curves are fits of the data to a saturation model $kP/(1 + P/P_s)$. (b) Fitted saturation power of the polariton PL emission as a function of temperature.

After the low-temperature measurements were done, when removing the sample from the cryostat, we found that the microcavity had delaminated. This is likely due to the large mismatch of coefficients of thermal expansion between the glass substrates and the PVAc bonding layer. Given that this makes the measurement a destructive procedure for our samples, and that there were no significant changes to the PL spectra or PL power dependence with temperature motivating further investigation, we did not perform any other low-temperature experiments.

4.2.4 Photoinduced degradation of PL emission in vacuum-filtered films

The first microcavities fabricated for the project used drop-cast films made from CNT ink with ODCB solvent(see Chapter 3). When these samples were first received, the photostability of PL emission under CW pumping was measured (Figure 4.7) and we found that at pumping intensities below the damage threshold, the PL emission intensity from bare films and microcavity polaritons was stable over a timescale of an hour (while the typical duration of a single PL measurement is under a minute).

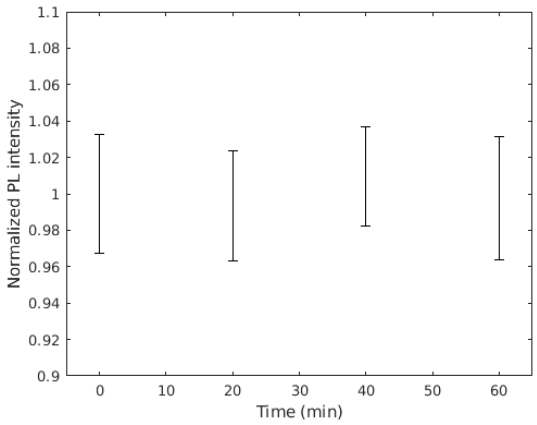

Figure 4.7 Polariton PL emission intensity over time for a DBR-mirror cavity using a drop-cast CNT film. The sample was under CW excitation by a 532nm laser at an absorbed intensity of 3.1 kW/cm^2.

This was assumed to be the case for all CNT films, and this assumption was not re-verified when the fabrication process was changed to vacuum-filtered films using CNT ink in toluene. Much later, we found that the PL emission from vacuum-filtered films actually showed a rapid degradation over a timescale of seconds when excited with a CW pump at an inten-

sity that was previously confirmed to be safe for drop-cast films. The time dependence of the decrease in PL follows a biexponential decay curve (Figure 4.8a), suggesting that there are two different mechanisms contributing to the photodegradation, a fast one ($\tau_1 = 41.5$ seconds) and a slower one ($\tau_2 = 4.9$ hours). Interestingly, while the PL emission is strongly suppressed, the polariton mode energy and linewidth remain unaffected (Figure 4.8b). This indicates that the mechanism at play does not change the absorption spectrum of the material. If the degradation mechanism acted to reduce the absorption of the S_{11} transition, it would reduce the light-matter coupling strength and shift the lower polariton mode to higher energies (Rabi contraction).

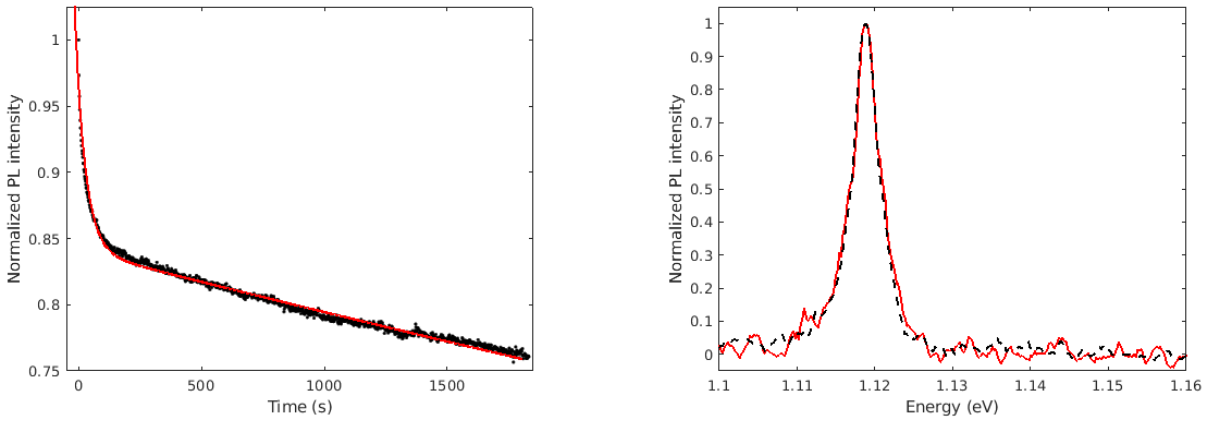

(a) (b)

Figure 4.8 (a) Polariton PL emission intensity over time for a DBR-mirror cavity using a vacuum-filtered CNT film, and fitted biexponential decay model with $\tau_1 = 41.5 \pm 0.3$ seconds and $\tau_2 = 4.90 \pm 0.04$ hours. The sample was under continuous CW excitation by a 532nm laser at an absorbed intensity of 0.36 kW/cm^2. (b) Normalized PL spectra before (black) and after (red) the PL intensity has decayed by 42% from continuous excitation.

It is likely that the degradation mechanism suppresses the PLQY of CNT excitons. Due to the high mobility of excitons in carbon nanotubes, a low density of exciton-quenching defects is sufficient to significantly suppress the PLQY [48], which would reduce the polariton occupation rate given that radiative pumping is the dominant process for polariton population in CNT microcavities [61].

It has been previously observed that excitation of the S_{11} or S_{22} transitions in the presence of oxygen greatly increases the rate of formation of sp^3 defects which act as exciton quenching sites [51]. Although all samples were stored under nitrogen between measurements, the CNT ink preparation, thin film fabrication, and cavity lamination were done in ambient atmosphere, and dissolved oxygen in the solvents might have remained trapped in the final samples. It is not clear why the samples using drop-cast CNT films were much more stable than the vacuum-filtered films using the same CNTs and wrapping polymer. At the time the phenomenon was noticed in vacuum-filtered films, we did not have any freshly-made drop-cast films to do a side-by-side comparison. Further investigation into the mechanisms of photoinduced degradation will be critical for enabling the use of high-concentration CNT thin films in photonics applications.

In summary, we have performed measurements of the photoluminescence emission of CNT excitons and CNT microcavity polaritons, using CW and femtosecond nonresonant excitation. We find that the polariton PL emission in the steady-state is very weak, due to the low PLQY of the CNT excitons. Under femtosecond pulse excitation, the PL emission is suppressed even further as EEA becomes an important nonradiative decay channel for excitons. This was confirmed by measurements of the EEA coefficient of the CNT material. Because of these two factors, we were unable to observe polariton condensation even at reduced temperature. We also observed rapid photoinduced degradation of the PL intensity in vacuum-filtered CNT films, which we attribute to the formation of sp^3 defects with efficient exciton quenching.

CHAPTER 5 NONLINEAR RESPONSE OF A POLARITON CNT MICROCAVITY UNDER PULSED RESONANT EXCITATION

After the CNT microcavity design, fabrication and characterization process was sufficiently optimized, samples could be obtained with CNT concentrations far exceeding what had been previously reported in the literature, while maintaining a high quality factor. The nonlinear response of these samples to a very intense resonant short pump pulse was characterized using angle-resolved transmission spectroscopy, and dramatic changes in the polariton energy dispersion could be observed, in addition to the expected energy blueshift due to polariton-polariton interactions.

To investigate the mechanisms behind the observed intensity-dependent changes in the measured angle-dependent spectra, numerical models were developed. First, a time-domain wave optics model using the Duffing model of nonlinear optical polarization allowed us to reproduce the polariton mode energy shift at normal incidence, but was unable to fully explain the features in the experimental data. Additional simulations using the transfer-matrix method and a frequency-domain finite-element wave-optics model allowed us to rule out different possible causes and finally explain the remaining features as being caused by a Kerr lensing effect occurring inside the cavity.

5.1 Nonlinear characterization of CNT polariton microcavities

As discussed in previous chapters, angle-resolved spectroscopy is the main tool used to characterize polariton microcavities, providing information on energy dispersion and polariton population statistics. The experiments presented thus far used it to probe the cavities in the linear regime, where the polariton density is low and polariton-polariton interactions are negligible. Most of the measurements were also performed using continuous-wave excitation, so that the system was observed in the steady-state regime. Here, we consider the case of a very strong resonant excitation, creating a high density of polaritons, such that polariton-polariton interactions become significant and blueshift the polariton mode energy. By necessity, the excitation must be delivered in an ultrashort pulse, such that the peak intensity is high enough to observe a nonlinear response, but the average intensity is low enough to avoid damaging the sample from excessive heating.

5.1.1 Experimental setup

Both reflection and transmission measurements were attempted, but obtaining artefact-free reflection spectra of the cavities with sufficiently high signal-to-noise ratio was challenging, as the contrast of the polariton mode in the samples was very small. In transmission, the probe light that is not resonant with the polariton mode is reflected away from the sample and never enters the setup, giving a spectrum with a low background. In reflection, the probe light that is not resonant with the mode is reflected towards the setup, where scattering and unwanted reflections on optical surfaces add artefacts and noise, making the task of resolving a small dip in a large background even more difficult. To get the best accuracy in fitting the polariton mode energy, the cavities' nonlinear optical response was measured in transmission.

The experiment used the same setup as the linear reflectivity and PL measurement (Figure 3.16), with some changes. To maximize the collected signal, the beamsplitter between the collection objective and the microscope tube lens is removed. This shifts the Fourier-space image slightly, and alignment of the Fourier lens L2 has to be adjusted when the setup is configured for transmission measurements. A periscope and microscope objective on a three-axis translation stage were added to focus the probe beam on the sample from the top side (with the collection objective on the bottom side). A supercontinuum light source was built to generate broadband short pulses with tunable spectral width and fluence.

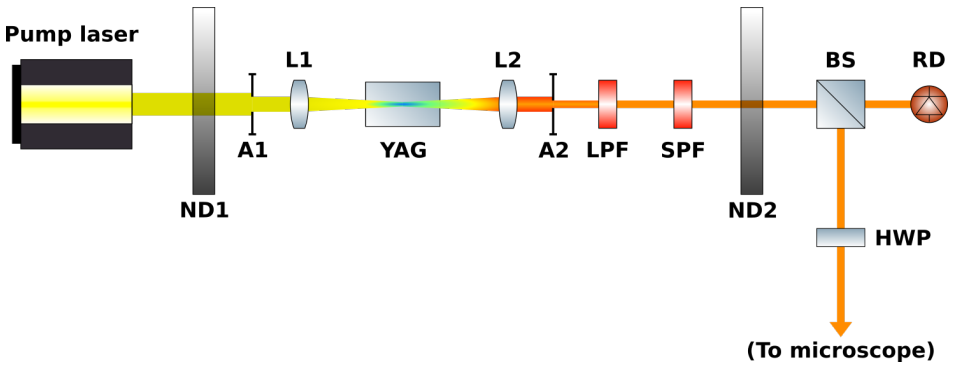

Figure 5.1 Setup for the supercontinuum probe generation. ND1 : Variable neutral density filter (manual). A1, A2 : Iris apertures. L1 : $f = 100$mm focusing lens. YAG : 5mm-thick YAG crystal. L2 : $f = 35$mm collimating lens. LPF : 1050nm longpass filter. SPF : 1150nm shortpass filter. ND2 : Variable neutral density filter (servo-controlled). BS : non-polarizing 50:50 beamsplitter. RD : Reference detector (Germanium photodiode). HWP : Achromatic half-waveplate.

Supercontinuum light source

In order to excite the polariton mode resonantly, a source of ultrashort optical pulses with tunable energy and sufficiently large bandwidth is required. Initial experiments used a Light Conversion ORPHEUS-F optical parametric amplifier as a probe, but the bandwidth (approximately 7nm) of the pulses was not well-suited to the measurement for the following reasons :

- Depending on the sample, the LP mode linewidth ranges between 3 and 5nm. To measure the transmission spectrum with good SNR, the probe should be significantly broader spectrally than the mode. Otherwise, there is not enough light intensity to accurately measure transmission in the wings of the transmission peak.

- The LP mode shifts to higher energy as the angle increases. The probe should also spectrally overlap with the LP mode at these higher angles, if we wish to measure the blueshift over a range of angles.

- The polariton mode is expected to shift to higher energy due to nonlinear effects (polariton blueshift, introduced in section 2.1.4). The probe must be spectrally broad enough to continue to overlap with the mode as it shifts, to continue to efficiently excite the mode. Otherwise, the nonlinear shift could be underestimated by the measurement (optical limiting).

A widely-used method to obtain broadband probe pulses for ultrafast spectroscopy is supercontinuum (SC) generation in a bulk transparent medium [77]. For this experiment, a 5mm long yttrium-aluminium garnet (YAG) crystal was used to generate a supercontinuum from 1030nm, 290fs pump pulses at a 100kHz repetition rate. The SC generation setup is illustrated in Figure 5.1.

The pulse energy, spot size, and numerical aperture of the pump are critical parameters to obtain a stable SC filament [78] [79]. A variable reflective attenuator is used to control the pump pulse energy, and an iris controls the pump beam diameter. The parameters that yielded the most stable SC spectrum were a beam diameter of 3.75mm and a pump pulse energy of 540nJ. The pump is focused into the YAG crystal using a $f = 100$mm achromatic doublet.

The SC light exiting the crystal is collimated by a $f = 35$mm achromatic doublet lens, and filtered by a pair of edgepass filters (1050nm longpass and 1150nm shortpass) to eliminate the unconverted 1030nm pump and avoid overheating the sample by exciting it with light outside of the cavity mirror stopband. The pulse energy after the filters (total energy in the band 1050-1150nm) was 70nJ. When setting up the SC probe, we ensured that there was no out-of-band leakage through the edgepass filters by dispersing the SC beam with a prism, and checking with a thermal power sensor that all of the SC power was refracted to the same angle.

The spectrally-filtered SC beam is then attenuated by a motorized variable reflective attenuator, and is divided in two by a 50:50 non-polarizing beamsplitter plate. Half of the beam is used as the probe for the experiment. It passes through a half-wave plate to align its polarization with the analyzer polarizer in the detection optics. The probe is then routed *via* a periscope to the microscope top objective, where it is focused on the sample.

The other half of the beam is used as a reference, and its average power is measured by a germanium photodiode. As the spectral responsivity curve of this sensor is quite flat in the wavelength range 1050-1150nm [80], the measured power value does not need to be corrected to account for the broad SC spectrum. The sensor's saturation behaviour was characterized by measuring the deviation between photodiode-measured power and thermal sensor-measured power for a range of pulse energies, and it was determined that below a pulse energy of 50nJ, the germanium photodiode was accurate within 5%. During the polariton blueshift experiment, the pulse energy in the reference beam was never increased above 5nJ.

The generated probe spectrum (Figure 5.2) is distinctly asymmetric due to the drop-off of SC generation efficiency as the frequency offset from the pump increases [79] and the sharp cut-off of the longpass filter at 1050nm. The probe intensity peaks at 1060nm and has a FWHM of 25nm, with the red-side shoulder decreasing much less sharply than the blue side.

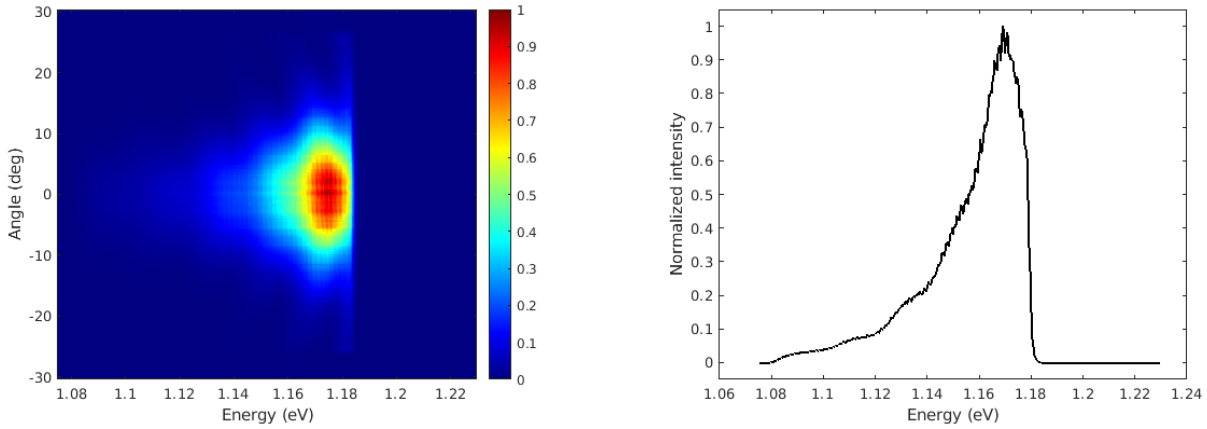

(a) (b)

Figure 5.2 (a) Angle-resolved spectrum of the supercontinuum probe. (b) Probe spectrum at normal incidence.

Procedure for nonlinear blueshift measurement

The procedure for the blueshift measurement is derived from the general procedure for angle-resolved spectroscopy (see section 3.2.6), with a few additional steps.

The transmission measurement is very sensitive to defects in any part of the cavity. Since the probe light must propagate through the entire thickness of the sample, a dust particle, crack or pinhole in any of the layers (including the substrate back surfaces) will cast a shadow that will appear as a dark stripe artifact in the angle-resolved spectra. In the initial sample loading procedure, after a defect-free spot in the CNT layer is located, the focus of the collection objective is shifted up and down to examine each layer as well as the substrate back surfaces in the dark-field imaging mode. Only spots that are defect free through the entire thickness of the sample are selected for measurement.

The probe spot alignment is done by attenuating the SC probe to a very low pulse energy (typically 0.02nJ), configuring the setup for real-space imaging, and adjusting the top objective position to center and focus the probe spot on the camera's field of view. This is first done without a sample loaded, and the angle-resolved spectrum fo the probe is recorded to serve as a transmission baseline. The supercontinuum intensity and spectrum are stable over a time scale of a few hours, so the baseline measurement is typically done at the beginning of each day, or when switching samples, but not for every single measurement.

Each time the baseline is measured, the reference to sample power ratio is also measured by placing a germanium photodiode power sensor at the sample position in the microscope and recording the measured power at the reference detector and at the sample position. This ratio is normally about 0.44 but can vary by a few percent when the top objective alignment is adjusted. For the ratio measurement, the sensor is not placed at the focal plane of the top objective but rather a few millimeters away, to avoid saturating the photodiode with a high localized peak intensity.

After loading a sample, the top objective focus must be re-adjusted, since propagation through the glass substrate will shift the focal plane slightly compared to propagation in free space.

To perform the blueshift measurement, the probe pulse energy is set to the lowest value that allows measurement of a spectrum with sufficient SNR (about 0.05nJ). The power read by the reference detector is recorded, and a background spectrum is measured with the probe shutter closed. The shutter is then opened and a transmission spectrum is measured. The shutter is closed, and the probe pulse energy is increased. This sequence is repeated for a range of probe pulse energies. As the probe pulse energy is increased, the camera integration time is decreased to avoid saturation. Finally, the probe pulse energy is decreased again to the first (lowest) value, and a final transmission spectrum is measured. The overlap between the first and last spectra shows whether there has been any sample damage during the measurement. If the first and last transmission spectra do not overlap, the dataset is discarded and the experiment is repeated in a different spot on the sample, reducing the maximum probe energy used. When setting up the experiment, we confirmed that the lowest probe pulse energy of 0.05nJ does not degrade the sample even after several minutes of continuous excitation.

5.1.2 Samples under investigation

The cavities used in the nonlinear polariton blueshift experiment used vacuum-filtered (6,5) CNT:PFO-BPy films with a very high mass loading of 63%. The mirrors were 11.5-pair SiO_2/Ta_2O_5 DBRs with a design wavelength of 1000nm, fabricated by Intlvac Canada by ion-beam sputtering on 0.7mm thick borosilicate glass substrates. To maximize the overlap of the CNT film with the cavity mode electric field, two spacer layers were used : an evaporated MgF_2 spacer on the bottom mirror, and a spin-coated PVAc spacer on the top mirror.

The two cavities used identical mirrors and CNT layers of similar thickness, but different spacer thicknesses in order to study the nonlinear response at two different exciton-photon detunings. The linear characterization techniques described in section 3.2 were used to measure the layer thicknesses in both samples (Table 5.1) and fit the linear angle-resolved spectra with the polariton energy dispersion model (Table 5.3). Both cavities had a large Rabi splitting on the order of 100meV and were in the negative detuning regime, with cavity MC1 at a large negative detuning of −84meV and cavity MC2 at a more moderate negative detuning of −45meV.

Table 5.1 Measured layer thicknesses in the two CNT microcavities used in the nonlinear blueshift experiment.

Sample	MgF_2 thickness (nm)	CNT thickness (nm)	PVAc thickness (nm)
MC1	224	43	177
MC2	172	35	181

Table 5.2 Measured polariton energies and linewidths of the two CNT microcavities used in the nonlinear blueshift experiment.

Sample	LP energy at $k_y = 0$ (meV)	LP FWHM at $k_y = 0$	LP Q-factor
MC1	1121	2.98	377
MC2	1160	5.75	202

Table 5.3 Fitted polariton parameters of the two CNT microcavities used in the nonlinear blueshift experiment.

Sample	Rabi splitting $2\hbar\Omega_R$ (meV)	Detuning Δ (meV)
MC1	139	-84
MC2	106	-45

Z-scan measurement of the CNT thin film material

To be able to model the nonlinear response of the microcavity, the nonlinear optical response of the CNT material must first be known. This was characterized using Z-Scan measurements (see section 3.2.4). The Z-scan measurements and the fitting of the data to the analytical model in reference [70] were performed by Pierre-Luc Thériault.

When the microcavities were received from UWM, a bare vacuum-filtered CNT film on glass substrate (fabricated in the same batch and assumed to have the same linear and nonlinear optical properties as the films inside the cavities) was provided as a reference sample for characterization. The linear optical dispersion and film thickness were first measured by ellipsometry and absorbance spectroscopy, before the Z-scan measurements.

Some preliminary Z-scan measurements were taken at a wavelength of 1110nm (close to the LP mode wavelength of the MC1 cavity) at two different peak intensities : $6.2\,\mathrm{GW/cm^2}$ and $25\,\mathrm{GW/cm^2}$. The results from these measurements (Table 5.4, Figures 5.3, 5.4) had a good signal-to-noise ratio and showed that at 1110nm, there is no detectable nonlinear absorption at low peak intensity, two-photon absorption at high peak-intensity, and that the Kerr coefficient is negative and saturates quickly as the peak intensity is increased.

Table 5.4 Z-scan measured Kerr coefficients at 1110nm for the reference CNT film of cavities MC1 and MC2.

Peak intensity $I_0(\mathrm{GW/cm^2})$	Kerr coefficient $n_2(\mathrm{m^2/W})$
6.2	$(-2.372 \pm 0.049) \cdot 10^{-14}$
25	$(-1.222 \pm 0.103) \cdot 10^{-14}$

These preliminary Z-scan measurements were done soon after the samples were fabricated, but before the nonlinear blueshift measurements were performed. After starting the nonlinear measurements of the cavities, we attempted to perform additional Z-Scan measurements at 1070nm (close to the LP mode wavelength of the MC2 cavity) and at 1110nm (to measure lower peak pulse intensities closer to what was used in the experiment). Unfortunately, the CNT film had degraded despite being stored under a dry nitrogen atmosphere. The Z-scan data at 1070nm (Figure 5.5) was very noisy and showed significant variation between measurement spots on the film.

We can observe significant saturable absorption at 1070nm as the probe transmission was always increased at the focus (even for very low peak intensities), but the transmission contrast in the open-aperture data did not follow a consistent trend as the peak intensity was increased and varied by a large factor between different spots on the sample, so a value for the one-photon saturable absorption intensity $I_{s,1PA}$ could not be extracted.

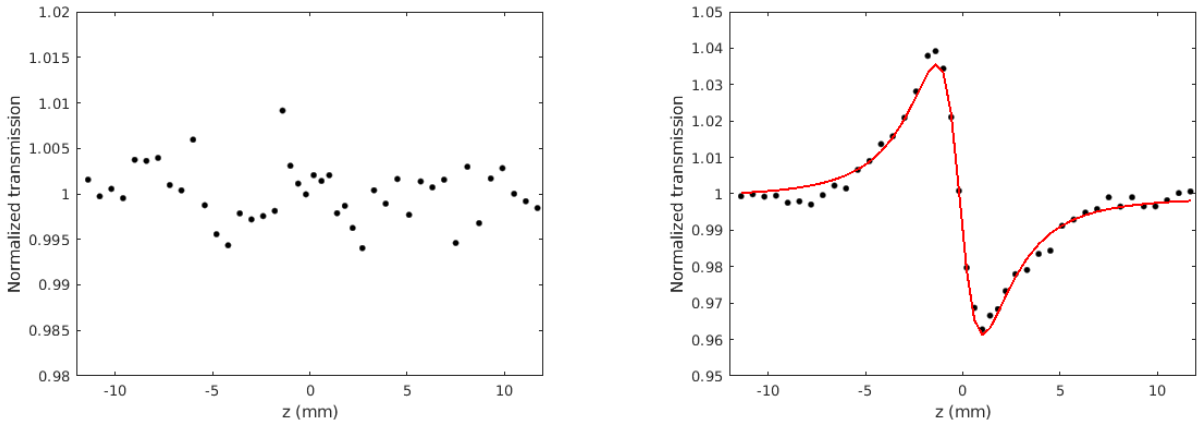

(a) (b)

Figure 5.3 Z-scan data (black) and fitted model (red) for the reference CNT film at 1110nm and $I_0 = 6.2\,\mathrm{GW/cm^2}$. (a) OA trace, showing no significant nonlinear absorption effects (No fitted model is shown for the open-aperture data as there are no visible features). (b) CA/OA trace, showing a strong signature of a negative Kerr effect with fitted $n_2 = (-2.372 \pm 0.049) \cdot 10^{-14}\mathrm{m^2/W}$.

We will focus the numerical modelling efforts in section 5.3.5 on cavity MC1, as it is the only one where we have a good measurement of the Kerr coefficient in the CNT material. The peak intensities in the cavity nonlinear blueshift experiments are lower than what was used in the Z-scan preliminary measurements, and the actual Kerr coefficient is likely slightly higher. The measured Kerr coefficients can be fitted with a saturation model $n_2(I_0) = n_2(0)/(1+I_0/I_{s,\,Kerr})$ to find a baseline Kerr coefficient $n_2(0) = -3.375 \cdot 10^{-14}$ m^2/W and a Kerr saturation intensity $I_{s,\,Kerr} = 14.19$ GW/cm^2. This is consistent with previous Z-scan measurements performed in our group on drop-cast CNT films at 1060nm and 1200nm [58]. However, in the absence of additional data points at other I_0 values, the saturation model is over-fitted and cannot reasonably be used. Instead, we will use the value measured at 6.2 GW/cm^2 in the numerical model, and ignore the saturation of the Kerr effect.

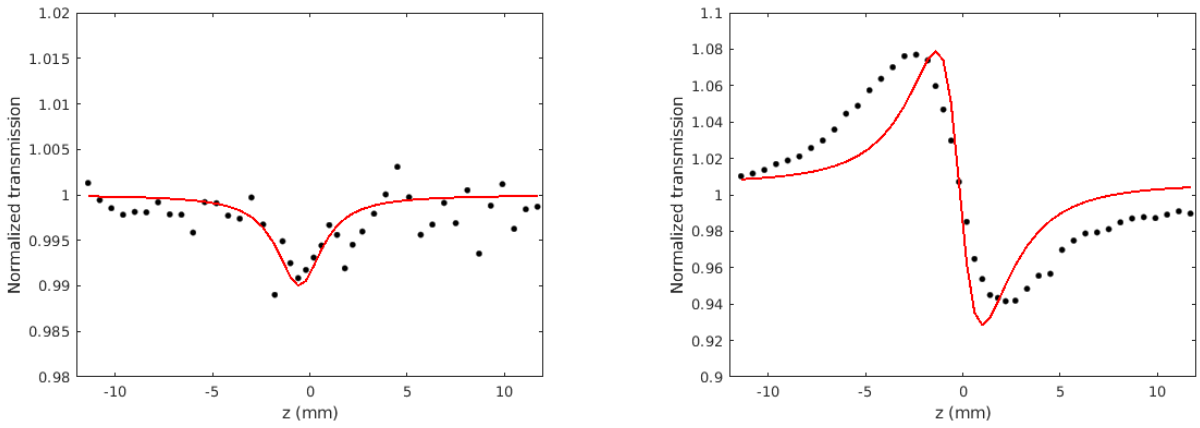

(a) (b)

Figure 5.4 Z-scan data (black) and fitted model (red) for the reference CNT film at 1110nm and $I_0 = 25\,\mathrm{GW/cm^2}$. (a) Open-aperture trace, showing a signature of two-photon absorption with fitted $\beta = 0.398 \pm 0.042\mathrm{cm/MW}$. (b) Closed-aperture trace, showing a strong signature of a negative Kerr effect with fitted $n_2 = (-1.222 \pm 0.103) \cdot 10^{-14}\mathrm{m^2/W}$.

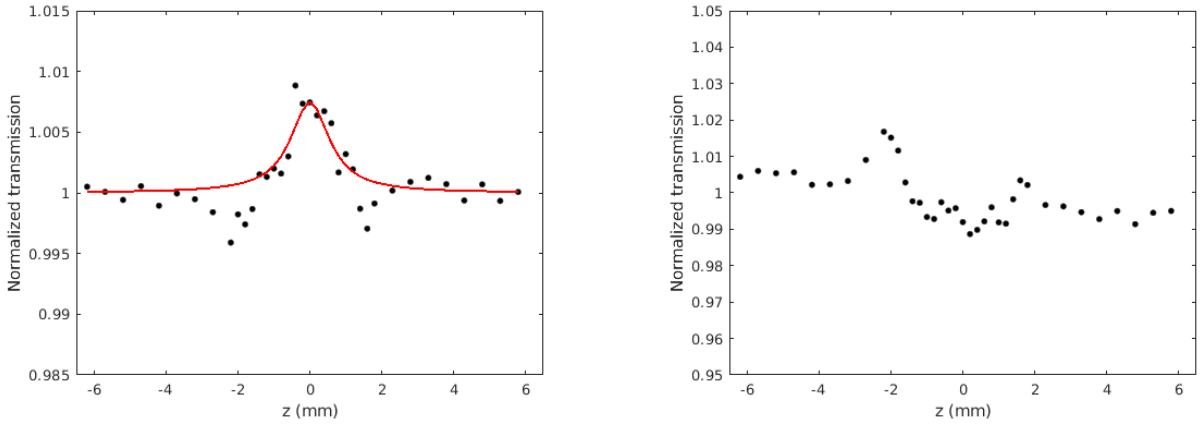

(a) (b)

Figure 5.5 Example Z-scan data and fitted model for the reference CNT film at 1070nm and $I_0 = 2.71\,\mathrm{MW/cm^2}$. Other spots in the same film measured at this wavelength and peak intensity showed different nonlinear response, indicating the material had degraded. (a) Open-aperture trace, showing a signature of saturable absorption with fitted $I_s = 2.95 \pm 0.31\mathrm{MW/cm^2}$. (b) Closed-aperture trace. A good fit could not be obtained on this dataset.

5.1.3 Measurement results and discussion

Both cavities exhibited strong changes in the angle-resolved transmission spectrum as a function of incident fluence. In addition to the expected positive energy shift of the polariton mode, we observed several other features, which dominated the measured spectra and made it difficult to resolve the change in energy. These features are qualitatively different between samples MC1 and MC2; we will discuss the measurement results for both microcavities separately.

Cavity MC1 (large negative detuning)

In the angle-resolved transmission spectra for cavity MC1 (Figure 5.6), the most striking change is the decrease in LP mode contrast at normal incidence, and the increase around 16 degrees. This was not expected from the simple model of a microcavity containing a Kerr medium, where the mode dispersion should remain essentially the same, but shift to higher energy as the refractive index is modulated by the Kerr effect.

The redistribution of transmitted intensity towards a high angle when the incident fluence is increased was observed in all measured spots in the cavity, and absent from the control spots (regions in the cavity that contained no CNTs, and were otherwise identical). This shows that the effect is caused by the nonlinear optical response of the CNT film and not a measurement artifact or scatter from a defect in the sample. The mechanism for this effect was not obvious, and required additional numerical modelling to explain (see section 5.4).

The blueshift of the polariton mode is not apparent in the angle-resolved spectra of Figure 5.6. In order to show it more clearly, spectra at normal incidence and at 16 degrees were fitted with an asymmetrically-broadened Lorentz lineshape (Figure 5.7), and the fitted mode energy, linewidth and contrast could be plotted as a function of incident probe fluence (Figure 5.8).

For both angles, the polariton mode shifts to higher energy as the fluence increases, with a larger blueshift observed at 16 degrees (Figure 5.8a). In the polariton description of the cavity, this would be explained by the fact that polaritons interact with each other through their excitonic component : as the angle is increased, the detuning is reduced, which increases the Hopfield coefficient corresponding to the excitonic part of the polariton state,

thereby increasing the polariton-polariton interaction strength. In the classical nonlinear optics description, the equivalent explanation is that the cavity mode energy increases at higher angles, which brings it closer to the exciton absorption peak, and the Kerr coefficient increases close to a resonance in the material.

At both angles, the polariton mode blueshift showed saturation behaviour, and the dependence of the blueshift on the incident probe fluence was fitted (Figure 5.10) to a simple saturation model $E_{LP}(F) = E_0 + \frac{k \cdot F}{1+F/F_{sat}}$. The fitted slope k was 6.6 times larger at 16 degrees than at normal incidence, and the saturation fluence was roughly the same around 4 mJ/cm^2(the confidence intervals of the fitted saturation fluence overlap between the two datasets). For the normal incidence case, the maximal blueshift reached before risking sample damage was $\Delta E = 0.52$ meV, and at 16 degrees $\Delta E = 2.29$ meV. These energy shifts are comparable to what has been reported in perovskite polariton microcavities below the condensation threshold [81].

The variation in LP mode contrast is drastically different between the two angles (Figure 5.8c). At normal incidence, the contrast is suppressed with increasing probe fluence, down to 6% of its original value. At a 16 degree angle, the contrast initially increases by a factor of 3, until the incident fluence reaches 4.5 mJ/cm^2 where the trend reverses and the contrast decreases again, while always remaining larger than the linear value.

The effect of increasing probe fluence on polariton mode linewidth was also different between the two angles : at normal incidence, a slight broadening was observed, while at 16 degrees there was a reduction in linewidth of about the same size.

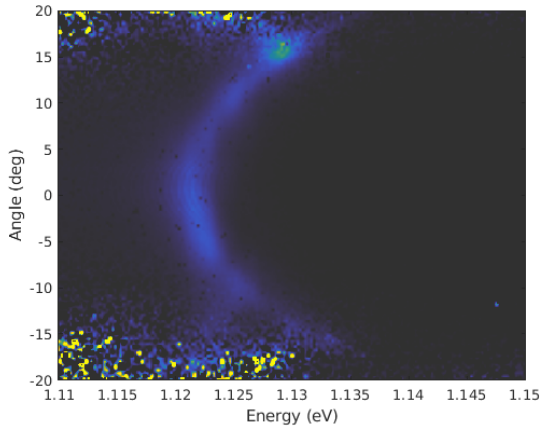

(a) 0.307 mJ/cm^2

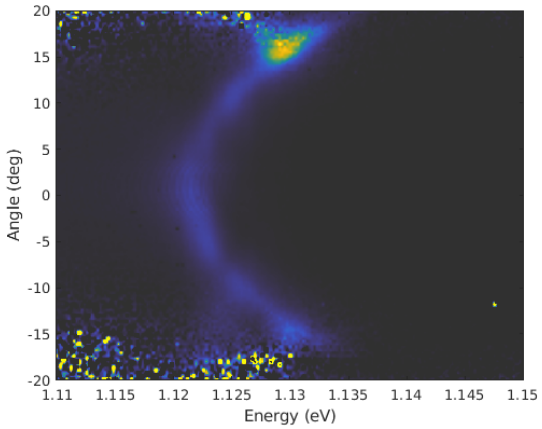

(b) 1.528 mJ/cm^2

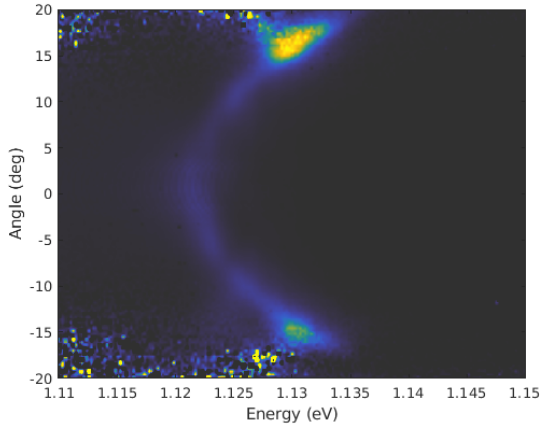

(c) 2.758 mJ/cm^2

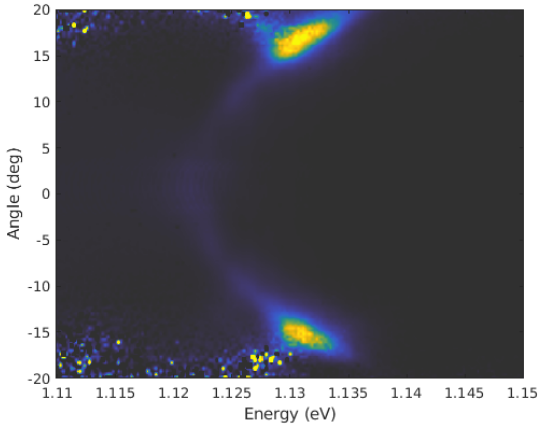

(d) 5.375 mJ/cm^2

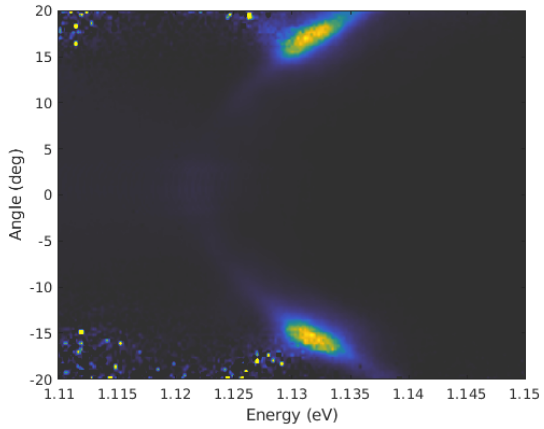

(e) 9.259 mJ/cm^2

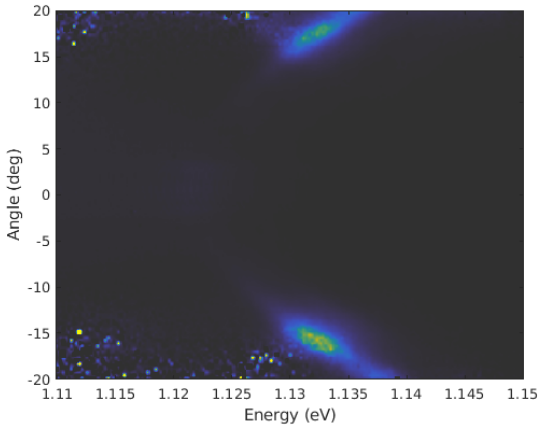

(f) 15.600 mJ/cm^2

Figure 5.6 Angle-resolved transmission spectra at different probe fluences for cavity MC1. All plots use the same colourscale, ranging from 0 to 0.125.

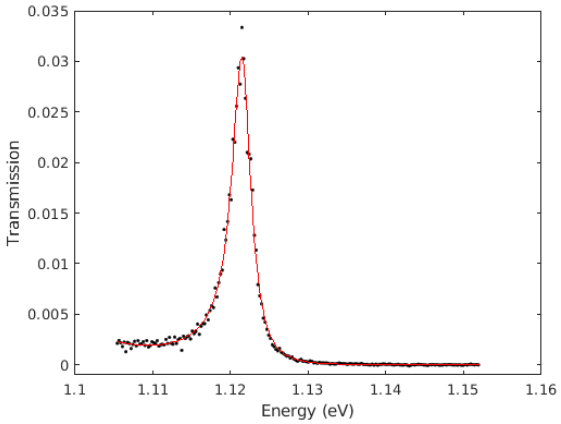

Figure 5.7 Example of a measured transmission spectrum for cavity MC1 at normal incidence (black) and the fitted asymmetrically-broadened Lorentz peak (red).

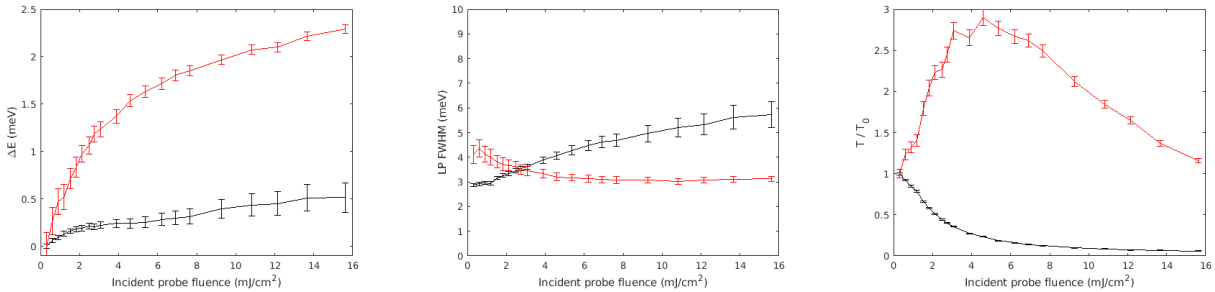

(a) Energy shift (b) Linewidth (c) Contrast modulation

Figure 5.8 Dependence of the fitted LP mode parameters on the incident fluence for cavity MC1 at normal incidence (black) and 16 degrees (red). The error bars correspond to the 95% confidence interval of the fit parameters.

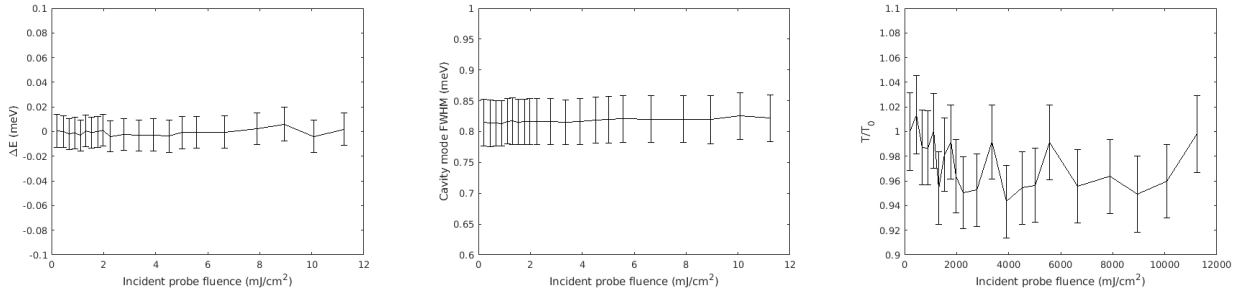

(a) Energy shift (b) Linewidth (c) Contrast modulation

Figure 5.9 Dependence of the fitted cavity mode parameters on the incident fluence for the control measurement of cavity MC2 (measurement spot without CNT film) at normal incidence. The error bars correspond to the 95% confidence interval of the fit parameters. All cavity mode parameters are unaffected by an increase in the incident fluence (within the confidence interval).

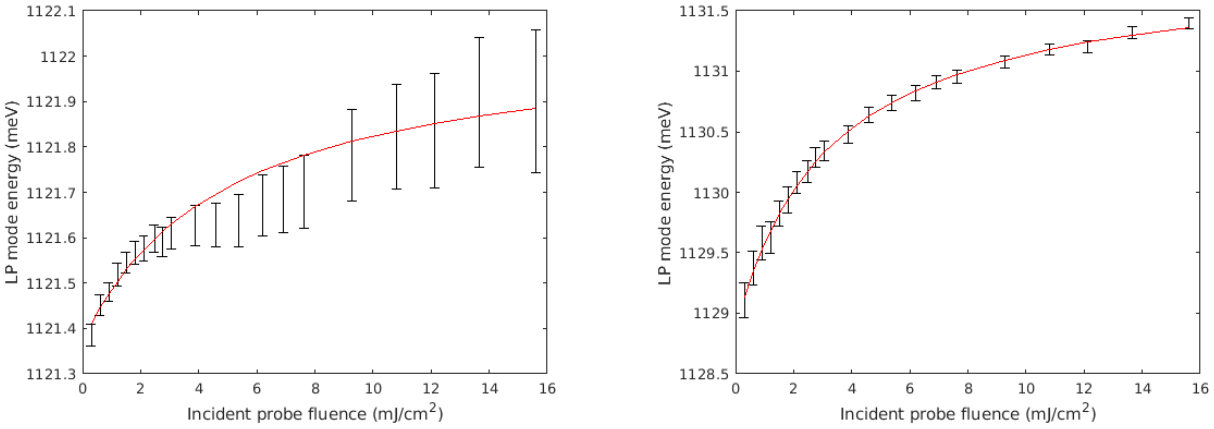

(a) Normal incidence (b) 16 degrees

Figure 5.10 LP mode energy in cavity MC1 (black) fitted to a saturation model (red) for two different angles. Fitted parameters for (a) $E_0 = 1121.37 \pm 0.04$ meV, $k = 0.14 \pm 0.05$ meV $\cdot$ cm^2/mJ and $F_{sat} = 4.98 \pm 2.18$ mJ/cm^2. Fitted parameters for (b) $E_0 = 1128.88 \pm 0.07$ meV, $k = 0.92 \pm 0.09$ meV $\cdot$ cm^2/mJ and $F_{sat} = 3.26 \pm 0.33$ mJ/cm^2

Cavity MC2 (moderate negative detuning)

In the angle-resolved transmission spectra for cavity MC2 (Figure 5.11), there are also dramatic changes with increasing fluence, which are qualitatively different from what was observed in MC1. There is again a reduction of the LP mode contrast (Figure 5.12c). This is accompanied by significant broadening of the mode at normal incidence (Figure 5.12b). However, unlike in the case of MC1, the contrast at high angle decreases everywhere, instead of concentrating the energy at a particular angle. Furthermore, on the low-energy side of the mode, the contrast is decreased below the linear value. This makes it impossible to properly fit the LP mode energy at high angle with a Lorentz lineshape, as the transmission spectrum deforms significantly and changes from a peak to a dip with increasing fluence (5.14).

Since the Z-scan measurements of the bare films at 1070nm suggest that there is significant saturable absorption in addition to the Kerr nonlinearity, it is not surprising that the nonlinear response of the CM2 cavity is qualitatively different than that of MC1 (where there were no nonlinear absorption effects). However, the presence of saturable absorption, and the fact that it could not be well-characterized, would make the modelling of the nonlinear response of MC2 very difficult.

The LP mode energy initially increases sharply with the incident probe fluence, but saturates at a low fluence and starts to decrease, before gradually increasing again with a much smaller slope (Figure 5.12a). This could be due to the presence of both the refractive (Kerr) nonlinear effect, which will shift the mode to higher energies, and the saturable absorption which would tend to shift the mode energy down (as the exciton transition saturates, the exciton-photon coupling is decreased, which reduces the splitting between the LP and UP modes; this effect is sometimes called "Rabi contraction" [82]). These two competing effects will have different saturation intensities, which would complicate the form of the intensity dependence of total blueshift beyond a simple linear or linear-with-saturation model. Nonetheless, the same saturation model that was used to fit the blueshift of cavity MC1 could be used on the normal-incidence spectra from cavity MC2, if the fit was restricted to the low-fluence range below the inflection point (Figure 5.13). The fitted slope k of the polariton blueshift was 27 times larger than for the normal-incidence data from cavity MC1, which is consistent with the fact that the LP mode energy in MC2 is closer to the exciton energy. The maximum blueshift observed in cavity MC2 at normal incidence was $\Delta E = 2.29$ meV.

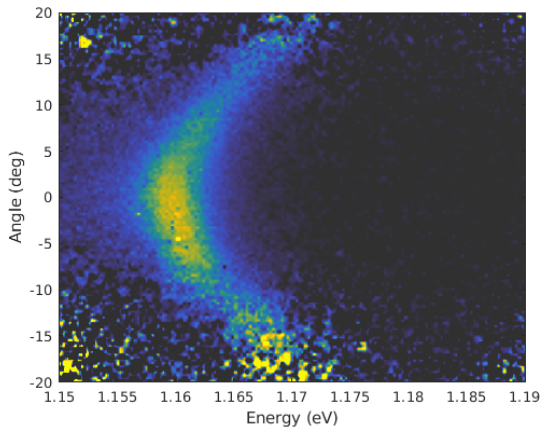

(a) 0.619 mJ/cm^2

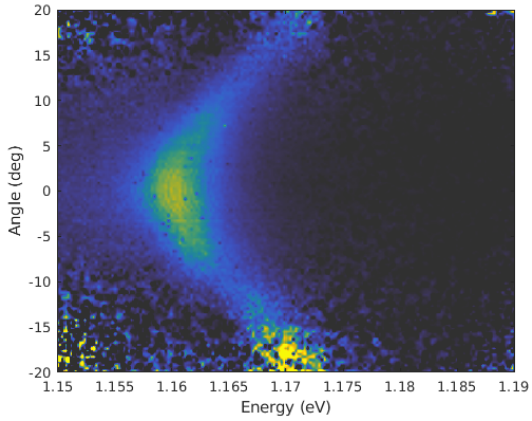

(b) 1.217 mJ/cm^2

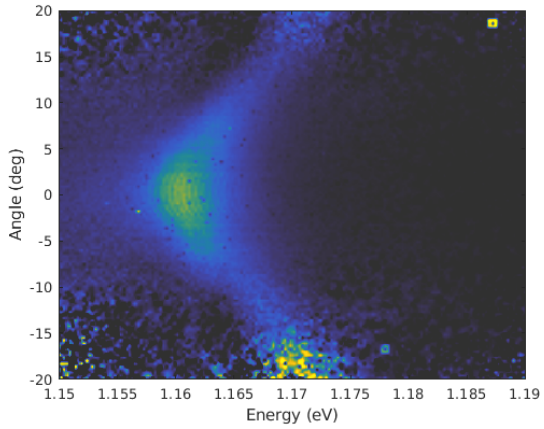

(c) 1.843 mJ/cm^2

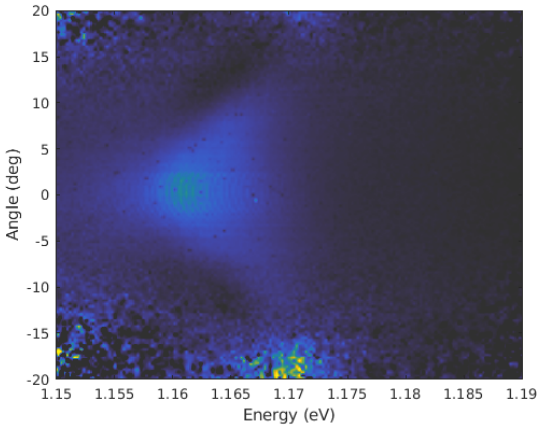

(d) 4.912 mJ/cm^2

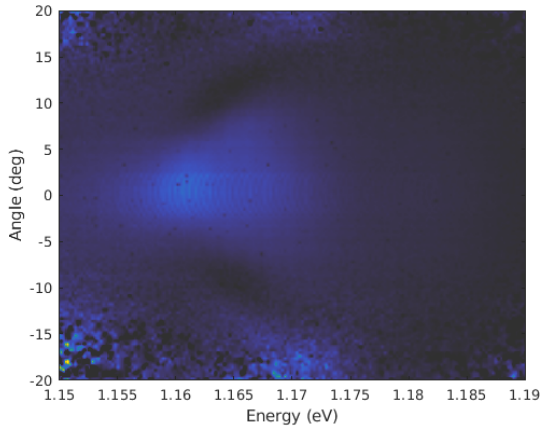

(e) 15.277 mJ/cm^2

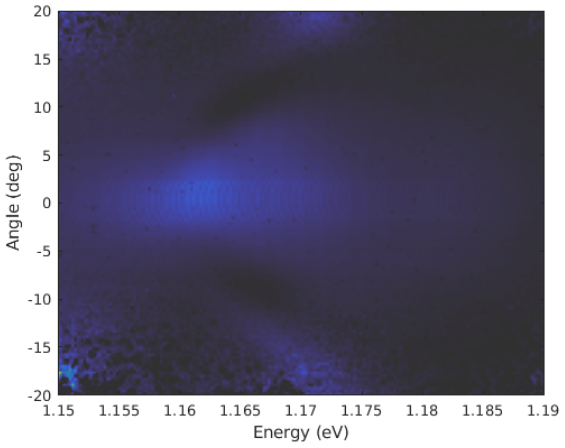

(f) 30.065 mJ/cm^2

Figure 5.11 Angle-resolved transmission spectra at different probe fluences for cavity MC2. All plots use the same colourscale, ranging from 0 to $1.25 \cdot 10^{-4}$.

At normal incidence, the LP mode linewidth increases up to a factor of two from its initial value, and saturates at about the same rate as the mode energy (Figure 5.12b). Finally, the contrast of the LP mode decreases in a similar manner as what was observed for cavity MC1, although not to the same extent (Figure 5.12c).

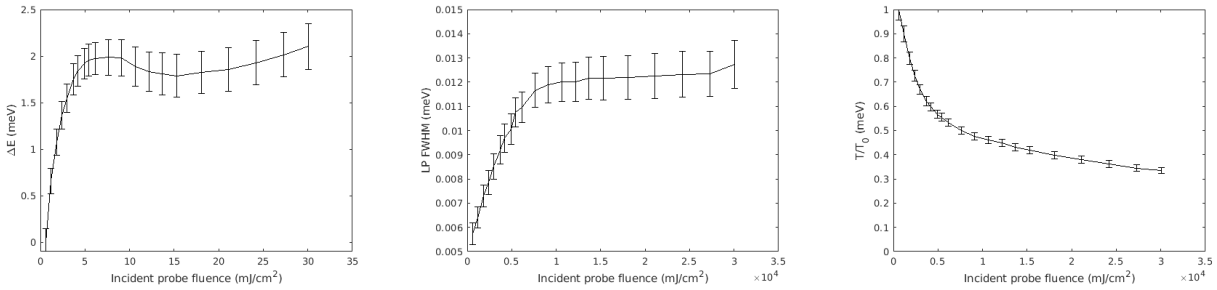

(a) Energy shift (b) Linewidth (c) Contrast modulation

Figure 5.12 Dependence of the fitted LP mode parameters on the incident fluence for cavity MC2 at normal incidence. The error bars correspond to the 95% confidence interval of the fit parameters.

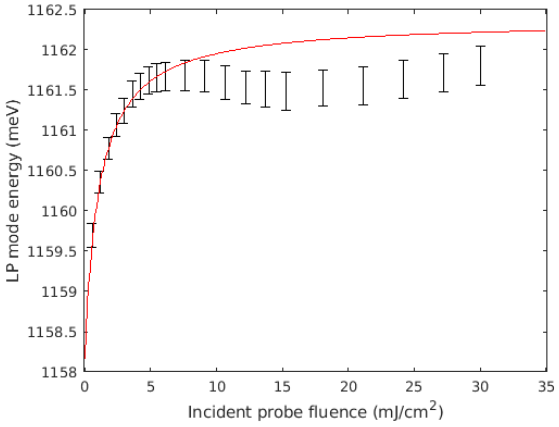

Figure 5.13 LP mode energy at normal incidence in cavity MC2 (black) fitted to a saturation model (red). The model is fitted to the first 10 datapoints only, before the inflexion point. Fitted parameters : $E_0 = 1158.17 \pm 0.47$ meV, $k = 3.84 \pm 1.46$ meV $\cdot$ cm^2/mJ and $F_{sat} = 1.09 \pm 0.33$ mJ/cm^2.

.

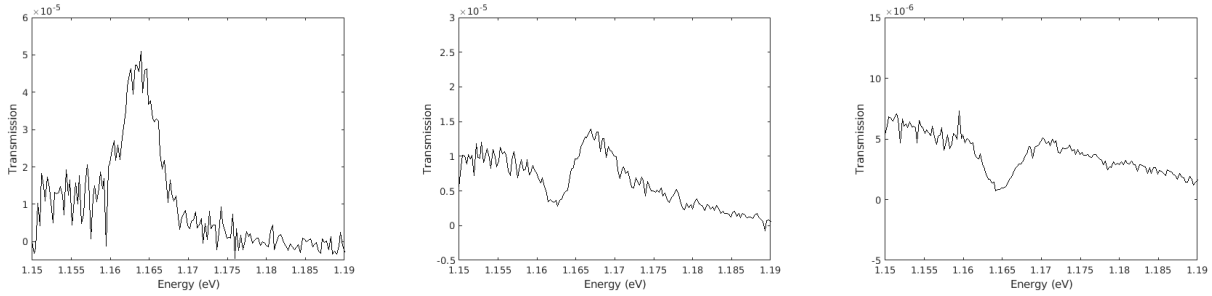

(a) 0.618 mJ/cm^2 (b) 6.155 mJ/cm^2 (c) 30.07 mJ/cm^2

Figure 5.14 Changes in the shape of the 10 degree transmission spectrum of cavity MC2 at three selected fluences.

5.2 Heat diffusion modelling

When a nonlinear response is observed in a power sweep experiment, it is important to rule out thermal effects. If the absorbed power from the probe pulses is significant, local heating of the measurement spot could change the optical properties of the materials, or thermal expansion could increase effective layer thicknesses. In a cavity, this would tend to shift the mode to lower energies, as the effective cavity length would increase. This could partially or completely mask the nonlinear blueshift we are trying to measure.

A common way to reduce the contribution of thermal effects is to perform the measurement at a low pulse repetition rate, typically below a few hundred Hz [83] [84]. Because the thermal effects depend on the average power absorbed at the pump spot, they will increase with increasing repetition rate. The Kerr effect depends only on the peak amplitude of the electric field, and will remain the same for a given pump fluence. Therefore, if the observed blueshift were unaffected by changes in pulse repetition rate, we could be confident that the contribution of thermal effects is negligible.

In the case of polariton blueshift measurement, it was not practical to perform the experiment at a low repetition rate, because of the very low transmitted light intensity of the sample. Using a repetition rate of 100kHz, the signal-to-noise ratio of the transmission spectrum ranged from 5 to 85 depending on probe fluence. If the repetition rate were decreased to 1 kHz to reduce spot heating, for an equivalent probe fluence the signal would be reduced by a factor of 100 and be impossible to resolve in the noise floor, much less fit the peak center energy accurately.

Therefore, instead of directly measuring the contribution of thermal effects, it was necessary to estimate spot heating by numerical modelling.

5.2.1 Simulation setup

Using the COMSOL Multiphysics finite-element modelling software, a simple simulation was implemented to solve the Fourier heat diffusion equation for a 2D axisymmetric geometry. The modelled structure was simplified compared to the actual cavity. Since the thermal properties of the SiO_2 and Ta_2O_5 in the dielectric mirror stacks are similar to those of the underlying glass substrate [85], they were not included in the model, and only the central part of the cavity was modelled. This consists of a 200nm MgF_2 spacer, 50nm CNT:PFO-BPy film and 200nm PVAc spacer. The thin film stack is surrounded on both sides by 50um thick glass substrates, and the lateral size of the model is 50um. The substrate dimensions were increased until the temperature gradient was negligible at the outer boundary of the model, so that the substrates could be considered infinitely large. The outside boundaries of the model were fixed to a temperature of 300K using a Dirichlet boundary condition. The initial temperature of the films and substrates was also set to 300K.

The material parameters needed as model inputs are the thermal conductivity κ, the specific heat capacity c_p, and the density ρ. For the borosilicate glass substrates [86] and the evaporated MgF_2 spacer [87], all these values are easily found in the manufacturer's datasheet. For the PVAc polymer, the data can be found in a handbook of material properties [88]. However, for the CNT:PFO-BPy film, the material properties have not been directly measured and must be estimated.

Measured or simulated thermal properties for PFO-BPy-wrapped (6,5)CNT films were not available in the literature, but published values for similar-composition samples can be used as an approximation. Avery *et al.* measured an in-plane thermal conductivity at 300K of 16.5 $\mathrm{W/m \cdot K}$ in PFO-BPy wrapped (10,8) vacuum-filtered CNT films of roughly the same concentration and thickness as what was used in our experiments [89]. They did not measure the out-of-plane thermal conductivity or the specific heat capacity. The thermal conductivity of CNT films is generally anisotropic, with reported ratios κ_x/κ_z ranging from 1.3 to 32, depending on the film composition and fabrication method [90] [91] [92]. In this simulation, we do not model anisotropic heat transport in the CNT film.

Pradhan *et al.* measured the specific heat capacity of randomly-oriented mixed-chirality single-wall carbon nanotube thin films [93] : $c_p = 720(\mathrm{J/kg \cdot K})$. Finally, the density of the CNT:PFO-BPy films can be estimated as follows : The density of a single (6,5)CNT is easily calculated, given that both the diameter [94] and the number of carbon atoms per unit length [95] are precisely known. This computes to a density of $4.02\mathrm{g/cm^3}$. The density of the bulk PFO-BPy polymer has not been published in the scientific literature or in the supplier specification, but the density of the related polymer PFO is $0.88\mathrm{g/cm^3}$ [96]. Using these two values, and the CNT mass loading ratio of the film of 63% (calculated from absorption measurement of the CNT ink), the bulk density of the CNT:PFO-BPy film is estimated to be $1.73\mathrm{g/cm^3}$.

The maximal absorbed power in the measured spot is calculated by integrating the product of the CNT cavity absorption spectrum (from a transfer-matrix model) and the probe power spectral density. Since the cavity absorption spectrum depends on incidence angle, the integration must be done over the probe injection angle as well as over the wavelength. The largest average incident probe power used in the experiment was 227μW, of which 0.83μW was absorbed in the CNT layer and contributed to the heating of the measured spot. A heat source with a Gaussian distribution of FWHM 3um and a total power of 1uW was added to the model.

Table 5.5 Values of the material parameters used in the heat diffusion model

Material	κ (W/m $\cdot$ K)	c_p (J/kg $\cdot$ K)	ρ (g/cm^3)
MgF_2	0.33	1000	3.18
Poly-(vinyl acetate)	0.159	1183	1.19
CNT film	16.5	720	1.73
Glass substrate	1.114	858	2.51

5.2.2 Results

The steady-state solution of the numerical model showed a rise in temperature of 0.076K at the center of the pump spot, for an absorbed power of 1μW (Figure 5.15). The peak temperature value can then be used to estimate the change in the cavity's transmission spectrum.

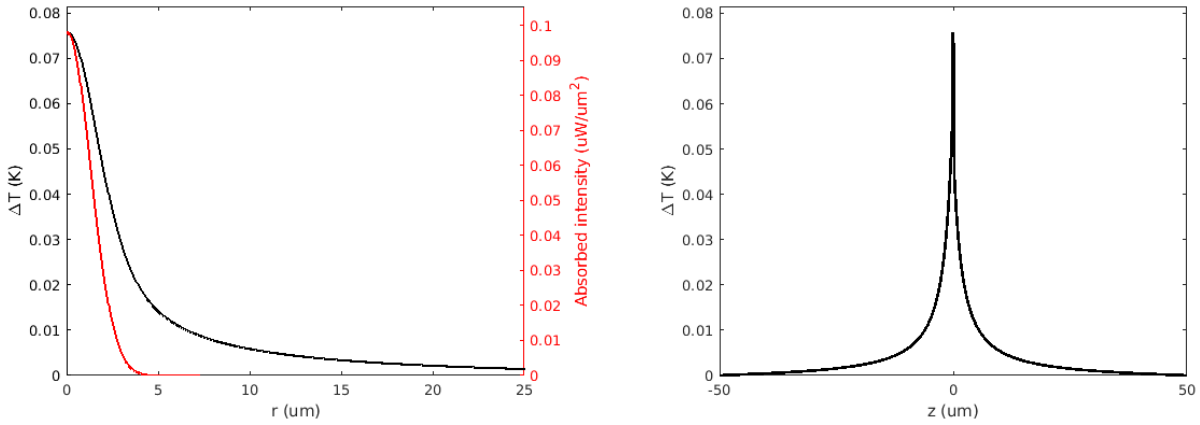

(a) (b)

Figure 5.15 (a) Absorbed intensity distribution for a total absorbed power of 1μW (red curve) and in-plane temperature profile in the CNT film (black curve). (b) Out-of-plane temperature profile.

When the temperature of a material is increased, two competing effects contribute to a change in optical path length : thermal expansion of the material will increase the physical path length, and the thermo-optic effect will reduce the refractive index, partially compensating the increase in optical path length [97]. To make a conservative estimate of the upper bound of polariton mode energy shift expected from thermal effects, we will neglect the thermo-optic effect, and consider only thermal expansion.

The coefficient of thermal expansion (CTE) of all the inorganic materials in the cavity is on the order of 10^{-6} K^{-1} [86] [98] [85]. The CTE of PVAc polymer is two orders of magnitude larger at $2.8 \cdot 10^{-4}$ K^{-1} [88]. Therefore, thermal effects on the inorganic layers in the cavity are not considered in the simulation. The coefficients of thermal expansion for CNT:PFO-BPy films or polyfluorene polymers in general (PFO, PFO-BPy, or other derivatives) could not be found in the published literature.

Because carbon nanotubes exhibit negative thermal expansion [99], CNT-containing composite films tend to have a smaller CTE than the bulk host polymer [100] [101] [102]. To make the most conservative estimate on the upper bound of thermal expansion, this effect is neglected. Since the CTE of the host polymer is not known, the CNT:PFO-BPy film is considered to have the same CTE as the PVAc film in the simulation. This seems a reasonable approximation for two reasons : First, in the range above cryogenic temperatures but below the glass transition temperature, many polymers have similar coefficients of thermal expansion on the order of $10^{-4}K^{-1}$ [88]. Second, since the CNT:PFO-BPy film is four times thinner than the PVAc spacer film, its contribution to the total thermal expansion will be relatively small.

In order to simulate the effect of thermal expansion on the cavity absorption spectrum, the transfer-matrix model of the cavity was modified to increase the thickness of the CNT and PVAc films as a function of temperature. For the CNT film, since the light absorption depends on the number of nanotubes (which remains constant), as the film thickness increases, the imaginary part of the refractive index is reduced proportionally, to keep the total absorption constant.

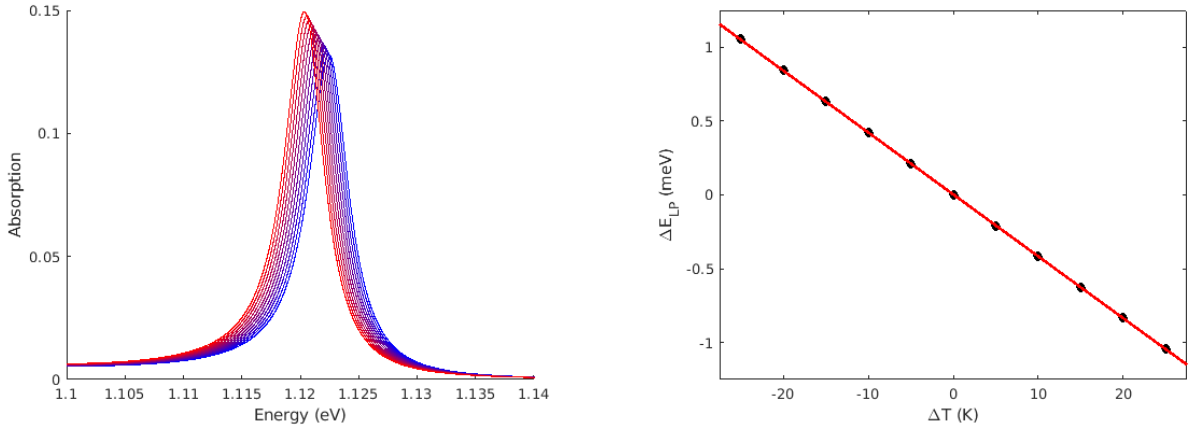

(a) (b)

Figure 5.16 (a) TMM-calculated cavity absorption spectra at normal incidence for temperature shifts from -25K (blue) to +25K (red) (b) Center energy of the LP mode (black) as a function of temperature shift, and linear fit (red) with a slope of -42 μeV/K.

The simulated temperature range was ±25K around ambient. The lower polariton mode absorption peak was fitted with a Lorentz lineshape for each temperature, and the dependence of the mode energy on temperature was fitted to a linear function with a slope of -42 μeV/K (Figure 5.16).

According to the simulation results, the 0.076 K rise in temperature from the absorbed probe power at the highest fluence used in the experiment would lead to a -3.18 μeV shift in polariton mode energy. This is two orders of magnitude smaller than the nonlinear blueshift observed in the experiment, and one order of magnitude smaller than the narrowest confidence interval in the mode energy measurements. We can conclude that thermal expansion at the probe spot did not have a significant contribution to the observed experimental spectra.

5.3 Time-domain modelling of polariton nonlinear response

Given the many features in the measured angle-resolved spectra, it is difficult to directly interpret the nonlinear response and identify the mechanisms involved. To help investigate the polariton microcavity's behaviour under strong resonant excitation, we first developed a numerical model of the nonlinear response in the time-domain. This allowed us to verify that the polariton nonlinear blueshift could be well explained by the Kerr effect (which was the measured dominant contribution of the nonlinear response of the CNT material). We then performed additional simulations to test assumptions regarding the effect of changes in pump pulse duration and spectral shape. Finally, we used a frequency-domain model of a simplified structure to show that the other features in the data could be explained by the presence of an induced gradient of the refractive index inside the cavity.

5.3.1 Kerr nonlinearity in the time domain : the Duffing model

To verify that the observed polariton blueshift is consistent with the measured optical nonlinearity of the CNT thin film material, a numerical model of the cavity nonlinear response was implemented using the COMSOL Multiphysics software [103]. While nonlinear transfer-matrix methods exist [104] and have been used to model polariton microcavities [105], they are not well-suited to model our polariton blueshift experiment. TMM models are expressed in the frequency domain, and calculate the optical response at a single well-defined frequency (making the assumption that the system being modelled is in steady-state equilibrium under CW excitation). In the case of the polariton blueshift experiment, the optical probe is a broadband pulse, with many frequencies contributing to the nonlinear polarization. Crucially, the probe pulse duration is on the order of the polariton mode lifetime, which means that the system does not have sufficient time to reach a steady state. To accurately model the microcavity's response to a transient excitation, it is necessary to explicitly compute the time evolution of the electric field. This is achieved using the finite element method (FEM) to solve Maxwell's equations. The linear dispersion, absorption, and nonlinear polarization of the CNT material are represented in the time domain using the Duffing model.

To properly reproduce the cavity's optical response, both its linear (refractive index dispersion and absorption spectrum) and nonlinear (Kerr effect) properties must be modelled. This is straightforward to do in the frequency domain : The linear dispersion and absorption can both be represented by a Lorentz oscillator model of the material polarization, and the Kerr

effect can be taken into account by adding a nonlinear polarization term. In the instantaneous Kerr effect approximation, the Kerr coefficient n_2 is considered a constant (independent of frequency). Previous measurements in our group [58] have shown that n_2 can be expected to vary relatively slowly with frequency in the range 1050-1150nm covered by the probe in this experiment, making it possible to use this approximation.

The frequency-domain Lorentz model of the material susceptibility is :

$$\chi(\omega) = \frac{f_L \omega_L^2}{\omega_L^2 - \omega^2 - i\omega\gamma_L} \tag{5.1}$$

Where f_L is the Lorentz oscillator strength, ω_L is the Lorentz oscillator frequency, and γ_L is the Lorentz oscillator damping rate.

This can be translated to the time domain as [106] the following differential equation for the material polarization :

$$\frac{\partial^2 P}{\partial t^2} + \gamma_L \frac{\partial P}{\partial t} + \omega_L^2 P(t) = \epsilon_0 f_L \omega_L^2 E(t) \tag{5.2}$$

Similarly, as described in section 2.3, the instantaneous Kerr effect is described in the frequency domain as

$$n(\omega) = n_0 + n_2 I(\omega) \tag{5.3}$$

Where n_0 is the linear index, n_2 is the Kerr coefficient and $I(\omega)$ is the local intensity at a given frequency. This can also be written in the time domain as a differential equation for the material polarization [107] :

$$P(t) = \epsilon_0 (n_0^2 - 1) E(t) + 2\epsilon_0 n_0 n_2 I(t) E(t) \tag{5.4}$$

which is an approximate expression where the term $(n_2 I(t))^2$ has been dropped from the expansion of $(n_0 + n_2 I(t))^2$, and is therefore only valid when $n_2 I(t) \ll 1$ (always the case in nonperturbative nonlinear optics). The intensity is $I(t) = |E|^2/2\eta$ where η is the wave impedance of the material.

The Duffing model is an extension of the Lorentz model which adds a nonlinear restoring force to the classical harmonic oscillator. It can be expressed in the time domain as [107] :

$$\frac{\partial^2 P}{\partial t^2} + \gamma_L \frac{\partial P}{\partial t} + \omega_L^2 e^{\alpha |P(t)|^2} P(t) = \epsilon_0 f_L \omega_L^2 E(t) \tag{5.5}$$

where α is a nonlinearity coefficient. We can make a small-signal approximation where $e^{\alpha|P|^2} \approx 1 + \alpha P^2$ (dropping the higher-order terms of the expansion) to lower the computational cost of solving the model, leading to equation 5.6.

$$\frac{\partial^2 P}{\partial t^2} + \gamma_L \frac{\partial P}{\partial t} + \omega_L^2 (1 + \alpha |P(t)|^2) P(t) = \epsilon_0 f_L \omega_L^2 E(t) \tag{5.6}$$

To relate the value of α in the Duffing model to the value of n_2 in the nondispersive instantaneous Kerr model, we consider the Duffing model in the nondispersive limit, where $\gamma_L \to 0$ and $\omega_L \to \infty$. In this case, equation 5.6 reduces to the form

$$P(t) + \alpha (P(t))^3 = \epsilon_0 f_L E(t) \tag{5.7}$$

From equations 5.4 and 5.7, the following relation between α and n_2 can be derived (valid in the small-signal regime) [107]:

$$\alpha = -\frac{n_0 n_2}{\epsilon_0^2 f_L^3 \eta} \tag{5.8}$$

One of the limitations of the Duffing model is that due to the approximations in the derivation above, the calculated material polarization starts to deviate significantly from the frequency-domain Kerr model when the refractive index nonlinear modulation $\Delta n / n_0$ in increased above the order 10^{-2} [108]. Therefore, the Duffing model as derived here is usable only in the perturbative regime of nonlinear optics.

Also, the Duffing model as used in the existing literature can only describe the real part of the third order nonlinear polarization (corresponding to the Kerr effect), and not the imaginary part (corresponding to either two-photon absorption or saturable absorption). From Z-scan measurements at the MC2 mode energy (close to the S_{11} transition), we know that there is

significant saturable absorption. In order to apply the same numerical modelling strategy to cavity MC2, it would have been necessary to extend the Duffing model to account for saturable absorption. Since we were unable to measure consistent Z-scan data for the CNT film at 1070nm, we would not have had accurate values to use in such an extended Duffing model, and so we did not develop one. However, this remains a promising idea to be developed in the future in order to accurately model nonlinear polariton cavities operating close to the exciton resonance, where both refractive and absorptive nonlinear effects play an important role.

5.3.2 Approximation of the CNT dispersion with a single-oscillator Lorentz model

For the material nonlinear response to be accurately represented by the Duffing model, it must first be described in terms of Lorentz oscillators. The full optical dispersion of the CNT film derived from fits to ellipsometry and absorbance data is expressed as a sum of many Lorentz oscillators plus background terms describing the asymptotic dispersion towards zero and infinite frequencies. This model would be cumbersome to translate to the time-domain Duffing formulation. However, in the experiment the probe spectrum is restricted to a relatively narrow band between 1050 and 1150 nm. Therefore, the cavity response will be accurately modelled as long as the CNT material dispersion is accurate within that band.

A single-oscillator Lorentz dispersion model with a background permittivity term was able to approximate the measured CNT material dispersion near the LP mode wavelength at 1106nm (figure 5.17). The real part of the dispersion is well-reproduced, but the imaginary part does not overlap as well with the model due to the trion absorption peak near 1140nm.

Table 5.6 Coefficients for the Lorentz model fitted to the CNT material dispersion in the band 1050-1150nm

Coefficient	Description	Fitted value
f_L	Oscillator strength	0.39696
ω_L	Center frequency	$2\pi \cdot$ 304.8978 THz
γ_L	Damping rate	$2\pi \cdot$ 7.4082 THz
ϵ_∞	Background permittivity	2.6206

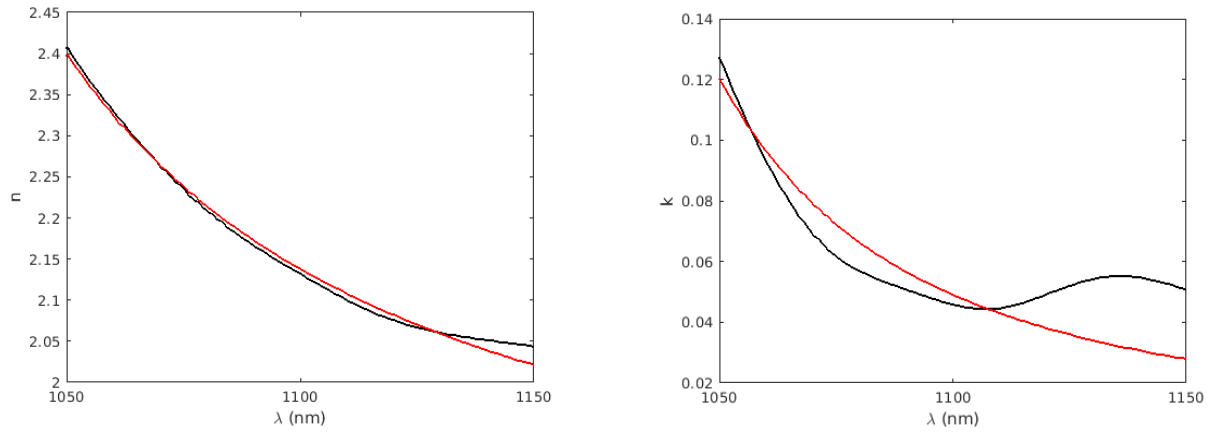

(a) (b)

Figure 5.17 (a) Real part of the CNT refractive index near the MC1 mode wavelength. Ellipsometer-measured dispersion in black, fitted Lorentz model in red. (b) Imaginary part of the CNT refractive index near the MC1 mode wavelength.

5.3.3 Validation of the Duffing model implementation

To check that the Duffing model as implemented in COMSOL Multiphysics with the parameters in table 5.6 properly reproduces the measured linear dispersion and shows the expected nonlinear change in refractive index, a simple model was set up to simulate light propagation through a CNT thin film.

Given that the standard formulation of the Duffing model does not use a background permittivity, it was necessary to slightly adapt it to properly account for ϵ_∞, with a modified definition of α :

$$\alpha = -\frac{n_0 n_2}{\epsilon_0^2 \left(f_L + \epsilon_\infty - 1\right)^3 \eta} \tag{5.9}$$

Where the linear index $n_0 = 2.139$ is set to the value at the LP mode resonance wavelength of 1106nm, and the Kerr coefficient $n_2 = -2.372 \cdot 10^{-14}$ m^2/W is set to the Z-scan measured value at 1110nm and the lowest measured peak intensity of 6.2 GW/cm^2 (see section 5.1.2).

Numerical setup

The model geometry is defined in two dimensions and consists of a single rectangular domain (50nm wide and 1000nm high). The left boundary is the input interface, configured as a source for a right-propagating plane wave. The right boundary is configured with a scattering boundary condition (SBC) to absorb all incident energy. The top and bottom boundaries are configured as perfect magnetic conductors. In the center of the domain, a probe records the time-dependent electric field $E(t)$ and displacement field $D(t)$.

A differential equation node was created in the COMSOL model to model the material induced polarization $\vec{P}(t)$ according to the Duffing model as defined in equations 5.6 and 5.9. The displacement field used by the solver was defined as $\vec{D}(t) = \epsilon_0\epsilon_\infty\vec{E}(t) + \vec{P}(t)$ to account for the background permittivity.

The domain is meshed with a swept mesh of rectangular elements (a single element in the transverse direction, 5nm wide elements in the propagation direction) and the solver time step size is set to 0.005fs. This value was chosen to ensure that the Courant-Friedrich-Lévy (CFL) number, defined as the fraction of a mesh element traversed by the wave during a time step, remained below 0.2 to ensure stable convergence of the solver and accurate results.

After the simulation, the recorded $E(t)$ and $D(t)$ fields are Fourier-transformed to obtain $E(\omega)$ and $D(\omega)$, which are then used to calculate the refractive index with

$$n(\omega) = \sqrt{\frac{D(\omega)}{\epsilon_0 E(\omega)}} \tag{5.10}$$

Results

Two series of simulations were run. The first series modelled the propagation of a continuous-wave signal of wavelength 1100nm for increasing intensity. In the small-signal regime, the refractive index modulation is linear with the intensity, and the index decreases as the intensity increases, as expected for a negative Kerr coefficient (Figure 5.18). However, the simulated n_0 and n_2 when using the coefficients in table 5.6 and equation 5.9 respectively were slightly different from the expected values, likely because of the approximations used in deriving the Duffing model.

By manually adjusting the values of f_L and α by a small amount, both the linear index and the slope of the nonlinear index modulation could be corrected to match the expected values. The optimized values are noted in table 5.7. At intensities beyond 0.1 GW/cm^2, the simulated refractive index starts to noticeably deviate from equation 5.3 with an error $(n_{Duffing} - n_{Kerr})/n_{Kerr} > 10^{-3}$.

Table 5.7 Optimized coefficients for the Duffing model of the CNT material

Coefficient	Optimized value
f_L	0.396447
α	$1.39115 \cdot 10^5$ m^4/C^2

The second series of simulations modelled the propagation of a broadband short pulse (λ_0 = 1100nm, FWHM$_t$ = 500fs, FWHM$_\omega$ = 16THz), for increasing peak intensity (Figure 5.19). At very low peak intensity, the Kerr effect contribution is negligible, and the calculated dispersion exactly overlaps with the frequency-domain Lorentz model of equation 5.1 with the coefficients of Table 5.6 (with a relative error $\Delta n/n < 10^{-4}$ between the Duffing-calculated and Lorentz dispersions). As the peak intensity is increased, the refractive index decreases below the linear value. The peak index modulation occurs at 1095nm, close to but not exactly at the pulse center wavelength (where the intensity is highest). This offset is caused by higher-order dispersion of the probe pulse, which distorts the pulse temporal envelope shape as it propagates.

This simple model validates the implementation of the Duffing model in the COMSOL Multiphysics FEM software, as both the linear dispersion and nonlinear refractive index modulation of the CNT material show the expected behaviour.

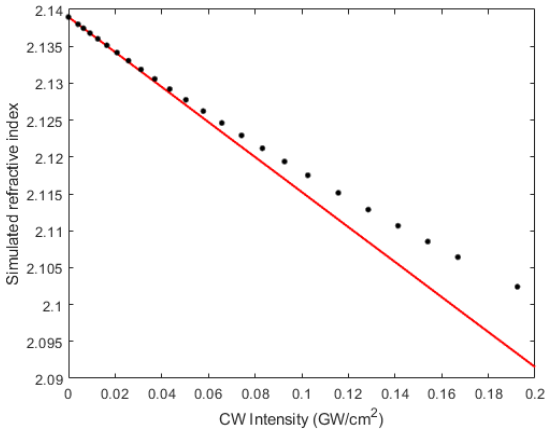

Figure 5.18 Simulated refractive index at 1100nm for the Duffing model under CW excitation, for a range of probe intensities. The red curve plots equation 5.3 with $n_0 = 2.139$ and $n_2 = -2.372 \cdot 10^{-14}$ m^2/W.

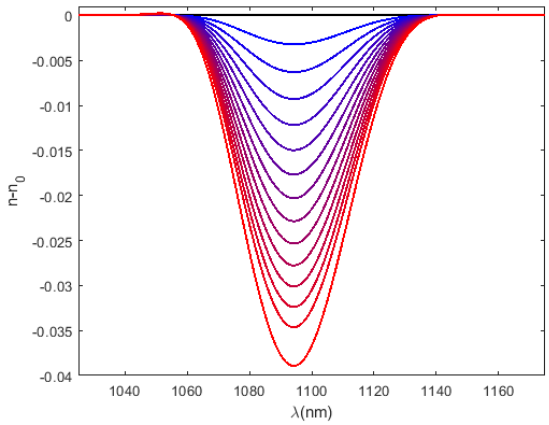

Figure 5.19 Refractive index modulation calculated with the Duffing model for increasing peak pulse intensity (black curve : linear regime (1 V/m), coloured curves : 0.01 to 0.1 GW/cm^2 peak amplitude, increasing from blue to red).

5.3.4 Probe pulse spectral and temporal envelope

To define a time-domain numerical model of the blueshift experiment, the probe pulse has to be expressed as a function $E_{in}(t)$. While the spectrum of the incident probe is accurately known from the baseline probe transmission measurement, the temporal envelope and the spectral phase are not.

Ideally, these would have been measured using a Frequency-Resolved Optical Gating (FROG) system, but this was not available at the time the experiment was performed.

An approximation of the pulse duration was derived in the following manner. The chirp of the supercontinuum pulse at the output of the YAG crystal is known from Kerr-gate pump-probe measurements [109] and is approximately linear with a value of $2.5 \cdot 10^{-3}$ rad/fs^2. When propagated through all the optics between the YAG crystal and the sample (collimating doublet lens, two edgepass filters, variable attenuator, and 20X microscope objective), the probe pulse accumulates a group delay dispersion[1] (GDD) of approximately 4000 fs^2 which stretches the pulse and slows the chirp down to $2 \cdot 10^{-4}$ rad/fs^2.

We attempted to match the center frequency, linewidth, and spectral shape asymmetry of the probe pulse (Figure 5.2) with a linearly-chirped sinusoidal wave, using various analytical expressions for asymmetric temporal envelopes, but a satisfactory solution could not be found. Ultimately, the probe pulse $E_{in}(t)$ was simply defined as a Gaussian-envelope linearly-chirped sinusoidal wave:

$$E_{in}(t) = E_0 \cdot \exp\left(-\ln(2)\frac{(t-t_0)^2}{(\sigma_t/2)^2}\right)\sin(\omega_0(t-t_0) + \frac{\xi}{2}(t-t_0)^2) \tag{5.11}$$

with the coefficients listed in Table 5.8. This definition does not accurately reproduce the entire spectral shape (Figure 5.20) of the probe. However, it approximately matches the intensity and slope near the LP mode wavelength at 1106nm. We expect that the cavity's nonlinear response will be relatively insensitive to the intensity at frequencies far from resonance, since the off-resonance components of the probe will be mostly reflected by the first DBR mirror and will not significantly contribute to the intracavity field. Similarly, the nonlinear response can be expected to be relatively unaffected by the exact shape of the temporal envelope, because the pulse width is much shorter than the mode lifetime. Both of these assumptions will be tested in section 5.3.5 with additional simulations.

[1]Exact GDD values at the 1100nm wavelength could not be obtained in the literature or from the optics manufacturers, except in the case of the longpass filter [110]. For the shortpass filter, the GDD was assumed to be the same as for the longpass. For the lenses, the GDD was estimated from the glass thickness, using the specified GVD values from the glass manufacturer [86] [111] [112].

Table 5.8 Coefficients for the analytical expression of the incident probe pulse $E_{in}(t)$

Coefficient	Description	Value
E_0	Peak amplitude	(Variable)
t_0	Amplitude temporal envelope center	1500fs
σ_t	Amplitude temporal FWHM	566fs
ω_0	Center frequency	$2\pi \cdot 282.823$ THz
ξ	Linear chirp	$2 \cdot 10^{-4}$ rad/fs^2

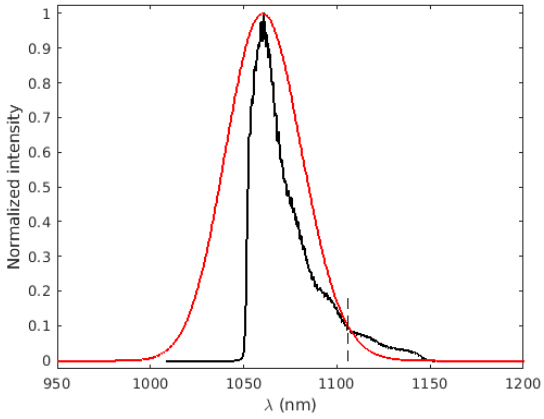

Figure 5.20 Measured (black) vs analytical time-domain definition (red) spectrum of the SC probe pulse. The thin dashed line marks the LP mode wavelength at 1106nm.

5.3.5 Modelling of the nonlinear response for cavity MC1

Cavity geometry and material parameters

The layer thicknesses in the cavity were determined using the linear characterization techniques described in section 3.2. The refractive indices in all materials except the CNT layer were set to a constant value (the value at the LP mode wavelength), and the dispersion of the CNT layer was represented by the Duffing model developed in the previous section. The glass substrates at either end of the structure were modelled with a thickness of 100nm, but were effectively of infinite thickness due to the SBC on the outside boundaries.

Numerical setup

The numerical setup (Duffing model differential equation, meshing, solver settings) was identical to the one used for the Duffing model validation simulations, with the exception of the incident pulse, which is defined using equation 5.11 with the coefficients in Table 5.8. The mesh element size was kept at 5nm for the CNT layer but increased to 25nm in the other layers. A point probe is configured to record $E_{out}(t)$, the electric field in the output substrate.

The simulation is run for a total time of 10ps, sufficiently long for the incident pulse to be completely reflected, absorbed or transmitted, with negligible stored energy remaining in the cavity. This takes approximately three hours with the available computing power (AMD Ryzen Threadripper 3970X 3.70GHz). After the simulation, the input field $E_{in}(t)$ and transmitted field $E_{out}(t)$ are Fourier-transformed, and the transmission spectrum is calculated :

$$T(\omega) = \frac{|E_{out}(\omega)|^2}{|E_{in}(\omega)|^2} \tag{5.12}$$

Results

With a weak intensity probe pulse ($E_0 = 1$ V/m), the calculated normal-incidence transmission spectrum in the linear regime can be compared with the measured spectrum for the lowest probe fluence (Figure 5.21). While the energy of the LP mode is well-reproduced by the model, the linewidth is slightly overestimated and the contrast of the transmission peak is not accurate. The contrast of the simulated mode is 4.85 times lower that what was observed experimentally. This difference is present in both time-domain and frequency-domain models; The TMM and COMSOL-calculated spectra overlap perfectly with each other, bu not with the experimental data. There are two likely contributing factors to these differences between the model and the sample. First, the absorption spectrum of the CNT layer could not be fully reproduced by a single-oscillator Lorentz model, due to the additional absorption peak near 1140nm (attributed to trion absorption). Specifically, at the mode wavelength of 1106nm, the real absorption is slightly lower than in the Lorentz model. This accounts for the narrower linewidth of the mode in the experimental results. Second, the models of the DBR mirrors use a "perfect" stack where all the high-index layers and low-index layers are identical. In the actual DBRs, unavoidable variations in thickness during manufacturing and scattering losses due to surface roughness reduce the reflectivity compared to the ideal case.

The polariton mode of cavity MC1 lies close to the DBR stopband edge, where small errors in layer thickness can cause a large drop in reflectivity. This would account for the higher transmission contrast seen in the experimental data.

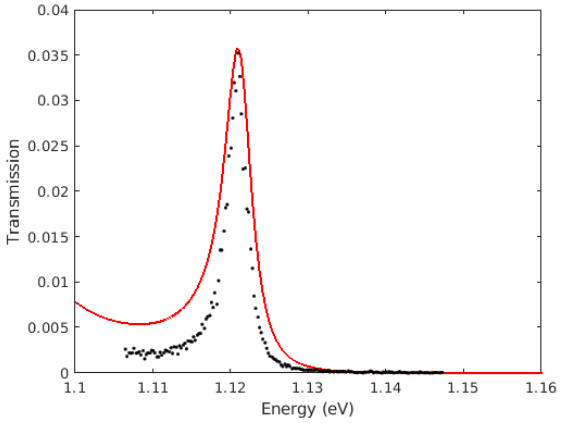

Figure 5.21 Simulated (red) and measured (black) normal-incidence transmission spectra for cavity MC1 in the linear regime. A scaling factor of 4.85 was applied to the simulated data to match the peak transmission value.

With stronger probe pulses (peak intensity ranging from 0.02 to 1.5GW/cm^2), we can observe a blueshift of the LP mode energy as the probe intensity is increased (Figures 5.22, 5.23a). This is qualitatively consistent with what was observed in the experimental measurements of cavity MC1 (Figure 5.8a), although the simulated blueshift shows a linear dependence with probe fluence over the whole simulated range, while the measured blueshift saturates.

We would not expect the saturation of the blueshift to be reproduced by the model, as it relates to saturation of the Kerr coefficient at high intensities, an effect that is not predicted by the simple Kerr model of equation 5.3.

The mode linewidth and contrast are not well-reproduced by the model; in the simulation, the linewidth slightly decreases and the contrast increases as the mode shifts to higher energy. This is the opposite of what was observed experimentally, where the mode was broadened by about 50% and the contrast suppressed by 94% at the maximum blueshift of 0.52meV. The increase in contrast in the time-domain Duffing model of the cavity is also inconsistent with the TMM simulations where the mode energy was shifted by thermal effects (Figure 5.16). In the TMM results, the contrast was suppressed as the mode shifts to higher energies,

although not as much as what was observed experimentally. When the peak intensity is increased an order of magnitude further (well beyond the limit where the Duffing model ceases to reproduce the Kerr model properly) the simulated peak transmission becomes larger than unity, which is obviously unphysical.

At the highest simulated peak intensities, the shape of the transmission spectrum starts to change significantly with a new peak appearing on the low-energy side of the mode. This happens as the peak intensity in the CNT layer is increased above the threshold of 0.1GW/cm^2 where the Duffing model starts to significantly deviate from the Kerr model.

The changes in transmission spectra at the high end of the simulated peak intensities are indicative of the model's failure to properly capture the nonlinear response of the material beyond the small-signal regime.

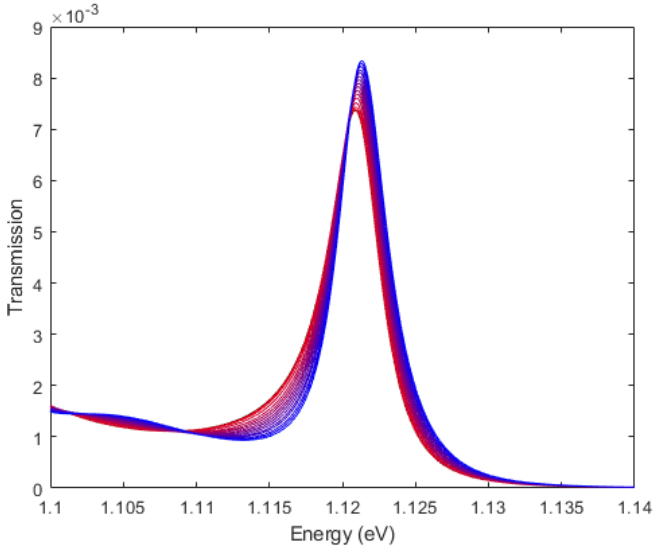

Figure 5.22 Cavity MC1 simulated normal-incidence transmission spectra in the linear regime (black) and at peak pulse intensities from 0.02 to 1.5GW/cm^2 (increasing from red to blue).

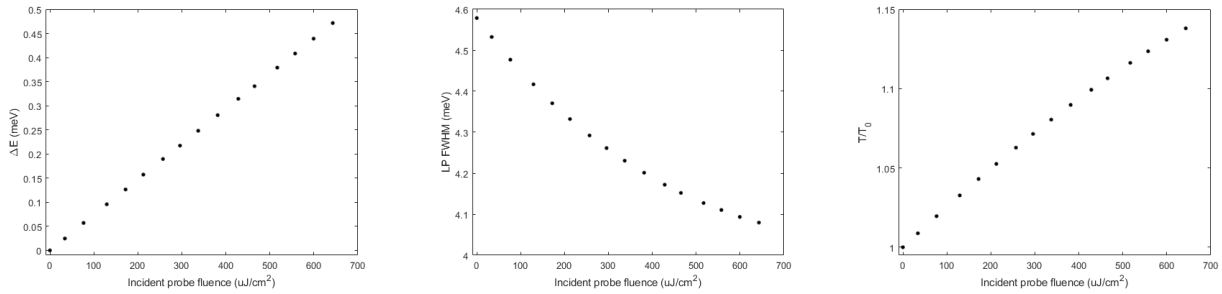

(a) Energy shift (b) Linewidth (c) Contrast modulation

Figure 5.23 Simulated LP mode parameters for cavity MC1 as a function of incident probe fluence.

Sensitivity of the model to probe pulse duration

To verify our assumption that the cavity response would not be highly sensitive to changes in pulse duration, a series of simulations was run with resonant probe pulses (spectral FWHM of 10THz or about ten times wider than the LP mode) of different temporal widths, starting with a FWHM of 100fs and progressively increasing the dispersion until the FWHM reached 1600fs. As the probe pulse was stretched to longer durations, its peak intensity was proportionally reduced in order to keep the fluence constant. For each pulse duration, five simulations were run with increasing pulse fluence, and the LP mode blueshift as a function of incident probe fluence was fitted to extract the slope. The results show that the slope of the blueshift with respect to probe fluence increases by only 4.4% (Figure 5.24) as the pulse is temporally stretched by a factor of 16. This justifies the approximation of only considering the probe fluence in modelling the experiment, when the exact temporal envelope width is not known. We can also observe that the variation of the nonlinear response with probe pulse duration is steeper at low pulse durations, and more moderate as the probe pulse becomes much longer than the mode lifetime of approximately 300fs.

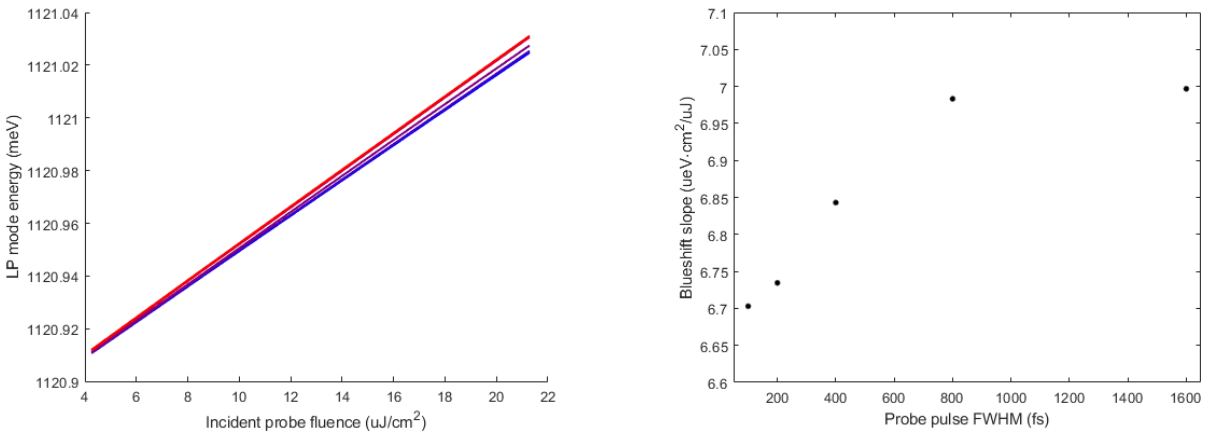

(a) (b)

Figure 5.24 (a) Simulated LP mode energy in cavity MC1 as a function of incident probe fluence, for probe pulse FWHM from 100fs to 1600fs (increasing pulse duration from blue to red). (b) Slope $\mathrm{d}(\Delta E)/\mathrm{d}F_0$ of the simulated LP mode blueshift in cavity MC1 as a function of probe pulse.

Sensitivity of the model to off-resonance pumping

The second assumption made to simplify the model was that the cavity response would be dominated by the on-resonance frequency components of the probe pulse. To verify this, a series of simulations was run to model the nonlinear response of the cavity to a probe pulse with a spectral width of 5THz and a peak intensity of 0.1 GW/cm^2, with the center frequency detuned from the LP mode by 0 to 10THz. We can observe that the blueshift drops off rapidly as the detuning is increased, following the decrease of the spectral overlap between the probe pulse and the intracavity field (Figure 5.25). This supports our assumption that only the on-resonance frequency components of the probe contribute significantly to the nonlinear blueshift.

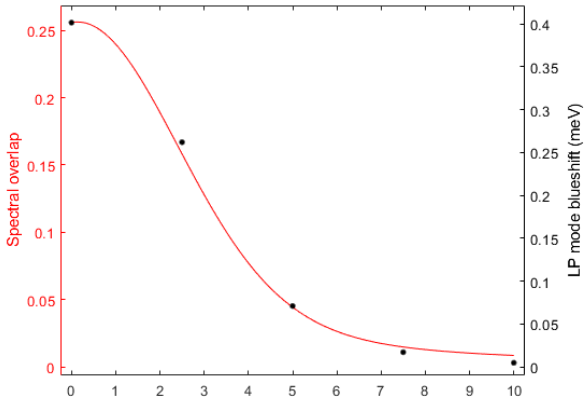

Figure 5.25 Simulated LP mode blueshift for cavity MC1 as a function of probe detuning (black). Spectral overlap between the probe and the LP mode intracavity field as a function of probe detuning (red curve).

Comparing the simulated and measured nonlinear blueshift

Using the two assumptions verified above, we can define a straightforward way to compare the experimental results with the time-domain numerical model, even if the model did not accurately reproduce the probe pulse spectrum and temporal envelope. The precise intensity envelope $I(t)$ of the probe in the experiment is not known, but the total pulse fluence is, as well as the probe spectrum $S(\omega)$. As we have shown above, the fluence is the important quantity determining the size of the LP mode blueshift, and off-resonance components of the probe do not significantly contribute to the nonlinear response.

If the total fluence of the probe F_0 is corrected by a factor representing the fraction of total fluence that is on-resonance with the LP mode, the resulting "effective fluence" F_{eff} should allow comparison of the nonlinear response between datasets with different probe spectra.

In the experiment, the probe intensity was distributed over a wide angular range (Figure 5.2a). For the measurement of the normal-incidence spectra, the transmitted signal at zero angle was integrated over a width of five pixels to improve the SNR. The definition of effective fluence for the experimental measurement must take into account the overlap of the angular intensity distribution of the probe with the angular integration region, in addition to the spectral overlap of the probe with the polariton mode.

We define F_{eff} as

$$F_{eff} = F_0 \left(\frac{\int_{\omega_1}^{\omega_2} \int_{-0.01084}^{0.01084} S(k_y, \omega) \, \mathrm{d}k_y \, \mathrm{d}\omega}{\int_0^{\infty} \int_{-0.65}^{0.65} S(k_y, \omega) \, \mathrm{d}k_y \, \mathrm{d}\omega} \right) \tag{5.13}$$

where $S(k_y, \omega)$ is the angle-resolved spectrum of the probe, the integration bounds $k_y \in [-0.65, 0.65]$ correspond to the numerical aperture of the collection objective and $k_y \in [-0.0184, 0.0184]$ defines the region of Fourier-space integrated to calculate the normal-incidence spectrum. The integration bounds ($\omega_1 = 2\pi \cdot 269.9554\text{THz}$, $\omega_2 = 2\pi \cdot 272.6138\text{THz}$) correspond to the $1/e^2$ width of the simulated LP mode intracavity intensity spectrum, containing approximately 86% of the total intracavity optical power.

The value of F_{eff} for the experiment is easily calculated by numerical integration of the measured probe angle-resolved spectrum. In the definition of F_{eff} for the numerical model, the integration in Fourier space is not necessary, as the model uses a plane wave excitation (all the incident fluence is at normal incidence).

When the polariton mode blueshift as a function of effective fluence is plotted for the experimental and numerical results (Figure 5.26), we can observe the overlap of the model with the small-signal behaviour of the cavity. The value of $\mathrm{d}(\Delta E)/\mathrm{d}F_{eff} = 34.76 \pm 0.04 \ \mu\text{eV} \cdot \text{cm}^2/\mu\text{J}$ for the simulated data agrees with $\mathrm{d}(\Delta E)/\mathrm{d}F_{eff} = 33.87 \pm 1.73 \ \mu\text{eV} \cdot \text{cm}^2/\mu\text{J}$ for the experimental data (in the range of fluence below the saturation threshold in the experimental data).

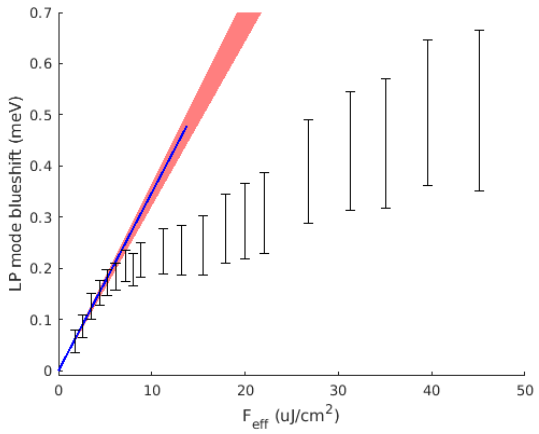

Figure 5.26 Measured (black) and simulated (blue) blueshift of cavity MC1 as a function of effective probe fluence. The red shaded region indicates the confidence interval of the linear fit to the first five points of the measured data. The fitted slope is $(\mathrm{d}(\Delta E)/\mathrm{d}F_{eff})_{\mathrm{exp}} = 33.87 \pm 1.73\ \mu\mathrm{eV} \cdot \mathrm{cm}^2/\mu\mathrm{J}$ for the experimental data and $(\mathrm{d}(\Delta E)/\mathrm{d}F_{eff})_{\mathrm{sim}} = 34.76 \pm 0.04\ \mu\mathrm{eV} \cdot \mathrm{cm}^2/\mu\mathrm{J}$ for the numerical model.

5.4 Modelling of the fluence-dependent changes in LP mode contrast

Additional numerical modelling was performed to elucidate the origin of fluence-dependent changes in the angle-resolved transmission spectral map observed in the experiment, especially the large reduction in mode contrast which could not be reproduced in the FEM time-domain model.

5.4.1 Non-linear absorption

Our first hypothesis was that there might be two-photon absorption in the CNT material, too small to be measured by the Z-scan method but causing a sufficient increase in cavity absorption losses to suppress the quality factor at high peak probe intensity. The noise floor and dynamic range of our Z-scan setup allows the reliable detection of a change in transmission on the order of $5 \cdot 10^{-3}$. This can be translated into a lower bound for the detectable change in the imaginary part of the refractive index. Beer-Lambert's law of absorption gives the transmission coefficient of the CNT thin film in the linear regime :

$$T_0 = \exp\left(-\frac{4\pi L k_0}{\lambda_0}\right) \tag{5.14}$$

Where L is the thickness of the material, k_0 is the imaginary part of the linear refractive index, and λ_0 is the vacuum wavelength. If a nonlinear effect modulates the value of k_0 by a small amount Δk, the transmission will change to a new value T', according to the new absorption $k_0 + \Delta k$. The quantity measured by the Z-scan method is the relative change in transmission $\Delta T/T_0 = (T_0 - T')/T_0$. The absolute change in transmission ΔT is :

$$\Delta T = \exp\left(-\frac{4\pi L k_0}{\lambda_0}\right) - \exp\left(-\frac{4\pi L(k_0 + \Delta k)}{\lambda_0}\right) \tag{5.15}$$

We can do a series expansion of this expression around $\Delta k = 0$ and discard the higher-order terms (assuming the perturbative nonlinear optics regime where $\Delta k \ll 1$).

$$\Delta T = \frac{4\pi L}{\lambda_0}\Delta k \exp\left(-\frac{4\pi L k_0}{\lambda_0}\right) + \mathcal{O}(\Delta k^2) \tag{5.16}$$

The expression for the relative change in transmission then reduces to

$$\frac{\Delta T}{T_0} = \frac{4\pi L}{\lambda_0}\Delta k \tag{5.17}$$

From this expression, knowing the film thickness $L = 35.6$nm and the wavelength $\lambda_0 = 1110$nm, we can calculate that the minimal detectable $\Delta T/T_0$ of $5 \cdot 10^{-3}$ corresponds to $\Delta k = 0.0124$.

To estimate how sensitive the transmission contrast of the lower polariton mode would be to 2PA, a series of TMM simulations was run. The microcavity structure was defined using the parameters for cavity MC1 from Table 5.1 and the ellipsometer-measured optical dispersion for all materials, except the CNT layer. For the CNT layer, a small Δk was added to the true material dispersion, simulating the additional absorption losses from 2PA. A range of Δk from zero to 0.025 were simulated.

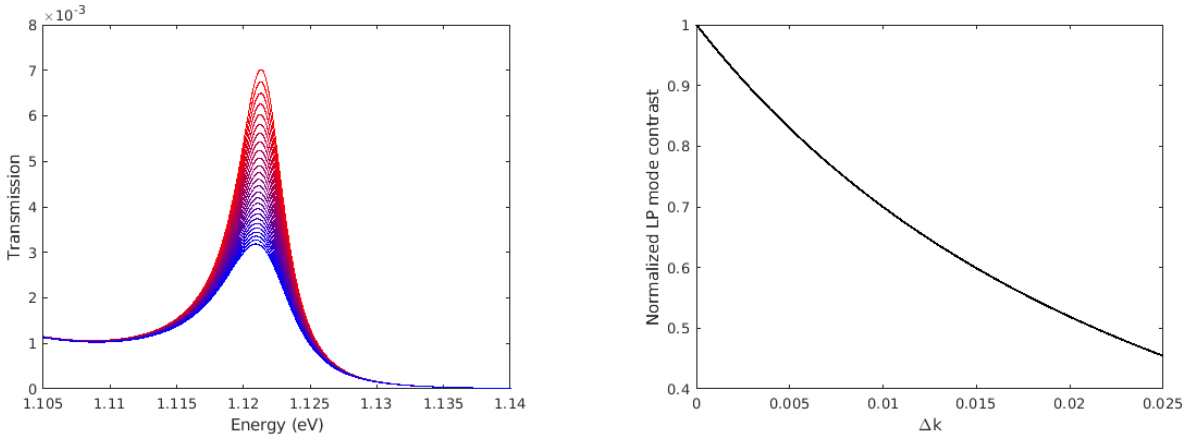

(a) (b)

Figure 5.27 (a) TMM-simulated normal-incidence transmission spectra for cavity MC1, with an absorption offset Δk from zero to 0.025 added to the CNT layer (increasing Δk from red to blue). (b) TMM-simulated normalized LP mode transmission contrast as a function of Δk.

The results (Figure 5.27) show that quite a large change in absorption is required to significantly affect the LP mode transmission contrast. Over a range of Δk from zero to 0.025 (twice the calculated minimum detectable modulation of the absorption for our Z-scan setup), the LP mode contrast is reduced by only 55%. In the experiment, the mode contrast was reduced by about 95%. Based on these results, two-photon absorption cannot account for the observed changes in LP mode transmission contrast.

The relatively low sensitivity of the mode contrast to changes in the material absorption can be explained by the fact that in the MC1 cavity, the absorption losses are large and dominate the mirror losses. The total losses of the system are therefore approximately proportional to the absorption. In a regime where the absorption losses are smaller than or equal to the mirror losses, a small change in absorption can lead to a dramatic change in the cavity mode quality factor, an effect exploited in cavity-enhanced absorbance spectroscopy.

Another argument against the nonlinear absorption hypothesis is that while it could possibly have explained the observed reduction in transmission contrast at normal incidence, it could not have explained the simultaneous increase at higher angles.

5.4.2 Four-wave mixing

Another possible explanation for the redistribution of transmitted intensity from zero angle to 16 degrees is a four-wave mixing process (see section 2.3). If light at the bottom of the polariton dispersion can be converted to light at another frequency and higher angle, this would account for the depletion of intensity at zero angle and the corresponding observed increase at 16 degrees.

To determine if this is possible in our sample, we plot the energy dispersion of the lower polariton cavity (Figure 5.28).

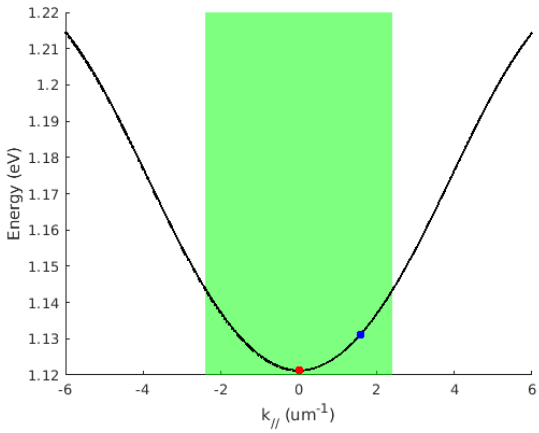

Figure 5.28 Energy dispersion of the lower polariton mode in cavity MC1. The blue dot marks the state where intensity is depleted, and the red dot marks the state where intensity is increased. The green shaded region indicates the range of momenta that can be injected by the supercontinuum probe.

For a wave mixing process to explain the observed experimental features, it should convert at least one photon at the energy $E_0 = 1.121$ eV and momentum $k_{\|} = 0$ indicated by the red marker on the figure, and produce at least one photon at the energy $E_s = 1.131$ and momentum $k_{\|} = 1.58\ \mu\text{m}^{-1}$ corresponding to the blue marker. This process will only be possible if energy and momentum are both conserved (that is, the sum of the energies of the destroyed and created photons should be equal, and the sum of the momenta of all four photons involved in the wave mixing process should be zero). We will examine all possible combinations of destroyed and created photons to see if any of them satisfy these conditions.

We can first consider the degenerate pump case where two $k_{\|} = 0$ photons are converted to two photons at different energies (signal and idler). If the signal photons has energy $E_s = 1.131$ eV, the idler photon must have an energy of $E_i = 1.111$ eV and an in-plane momentum of $k_{\|} = -1.58\ \mu\text{m}^{-1}$. Such a state does not exist on the lower polariton dispersion curve.

The case where two $k_{\|} = 0$ photons and one photon at some energy E_p are converted to one photon at the blue market position can be immediately dismissed, as this would require E_p to be negative.

We then consider the more general case where one $k_{\|} = 0$ photon and another photon at some other energy E_p are converted to a signal and idler photon, where the signal photon has an energy $E_s = 1.131$ eV. The value of E_p is restricted to the range of states that can be excited by the supercontinuum probe, and the energy of the idler photon cannot exceed 1.217eV (the mode energy when the angle of incidence reaches 90 degrees). Within these constraints, there are no possible combinations of E_p and E_i that satisfy energy conservation. This also exclude the case where one $k_{\|} = 0$ photon and one photon with energy E_p are converted to a pair of photons at a degenerate energy E_s.

Finally, we can consider a process converting one $k_{\|} = 0$ photon and a pair of degenerate photons at some energy E_p to one photon at the energy $E_s = 1.131$ eV. This would require the degenerate pump photons to have an energy $E_p = 50$ meV and an in-plane momentum $k_{\|} = -0.79\ \mu\text{m}^{-1}$. Again, such a state does not exist on the polariton dispersion curve.

From these arguments, we can conclude that four-wave mixing processes cannot explain the observed features in our experiment.

5.4.3 Intracavity Kerr lens

The third hypothesis that was examined hinged on the fact that while the optical probe in the experiment was focused to a small spot with a Gaussian spatial intensity profile, the time-domain FEM model used a plane wave to reduce the computational cost. The meshing also used a single mesh element in the direction transverse to the propagation of the wave. This meant that it was effectively a 1D model, and did not reproduce the modulation of the refractive index in the transverse direction.

In reality, the tightly focused probe beam creates a negative Kerr lens at the measurement position, which we can expect to perturb the cavity mode, and would affect the angle-resolved transmission. While the case of an intracavity Kerr medium has been thoroughly described in the context of modelocking lasers [113], that is not equivalent to the case we consider here. In the typical treatment, the cavity is large and the beam is relatively wide, and the formalism of Gaussian beams with the paraxial approximation can be used. In our case, both the cavity length and the probe focal spot size are on the order of the wavelength, requiring a wave-optics approach.

A time-domain wave-optics simulation of the intracavity Kerr lens using the Duffing model was not practical, due to the heavy computational cost that would result from meshing the transverse direction over the whole geometry. To attempt to gain insight into the qualitative behaviour of the angle-dependent transmission when a transverse refractive index modulation is present, a much simpler frequency-domain toy model was simulated instead.

Numerical setup

The toy model consisted of a purely photonic cavity (no semiconductor material) using two 5-pair DBR mirrors ($n_H = 2.5,\ n_L = 1.5$, design wavelength 1000nm) and a center layer with $n_C = 1.5$. The cavity mode wavelength at normal incidence was chosen to coincide with the DBR design wavelength. All materials were absorptionless and dispersionless. The cavity was surrounded by vacuum on both sides with $n_S = 1$, and all the outside boundaries of the geometry were configured as SBCs. The left boundary was also configured as a source for a Gaussian beam focused to a spot size of $3\mu m$, with the focal plane in the center of the cavity. The entire geometry was meshed with 25nm-size triangular elements.

The model was solved in the frequency domain using a direct solver, for a range of frequencies around the resonance (955-1005nm with a 0.1nm step). For each solution, the spatial Fourier transform of the position-resolved electric field intensity at the output boundary $|E(x_{out}, y)|^2$ was computed to obtain the angle-resolved intensity $|E(k_y)|^2$. In this manner, the angle-resolved spectral intensity map of the transmitted light was obtained.

To calculate the angle-resolved transmission, a baseline simulation was run with the same geometry and meshing, but setting the refractive index of all the domains to $n_S = 1$, simulating the propagation of the probe beam through free space. Then, the angle-resolved spectral intensity map of the cavity model was divided by that of the baseline model to produce the angle-resolved transmission spectral map (Figure 5.30a) showing the parabolic energy dispersion of the cavity mode.

In order to model the intracavity Kerr lens without having to explicitly add a Kerr term to the model, the nonlinear modulation of the refractive index was approximated using the linear solution for the electric field intensity distribution. The electric field intensity transverse profiles at the center of the cavity for all simulated wavelengths were averaged together to give the effective intensity distribution when excited with a spectrally flat light source (Figure 5.29a). Finally, the intracavity Kerr lens can be approximated by manually introducing a transverse refractive index modulation in the cavity center layer according to the effective field intensity distribution (Figure 5.29b).

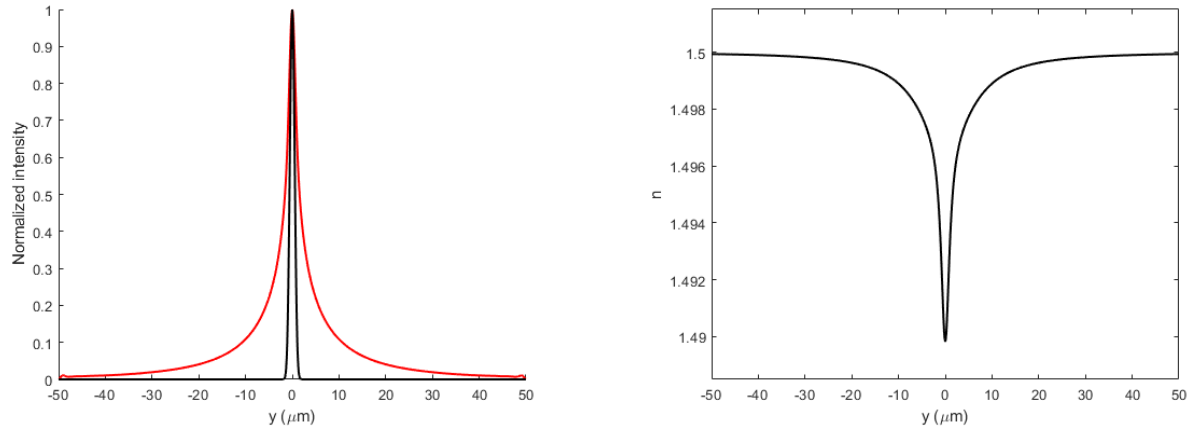

(a) (b)

Figure 5.29 (a) Wavelength-averaged transverse intensity profile in the center layer of the baseline model (black curve) and cavity model (red curve). Probe spot FWHM 3 μm. (b) Transverse refractive index profile applied to the center layer of the cavity model (modulation depth $\Delta n = -0.01$).

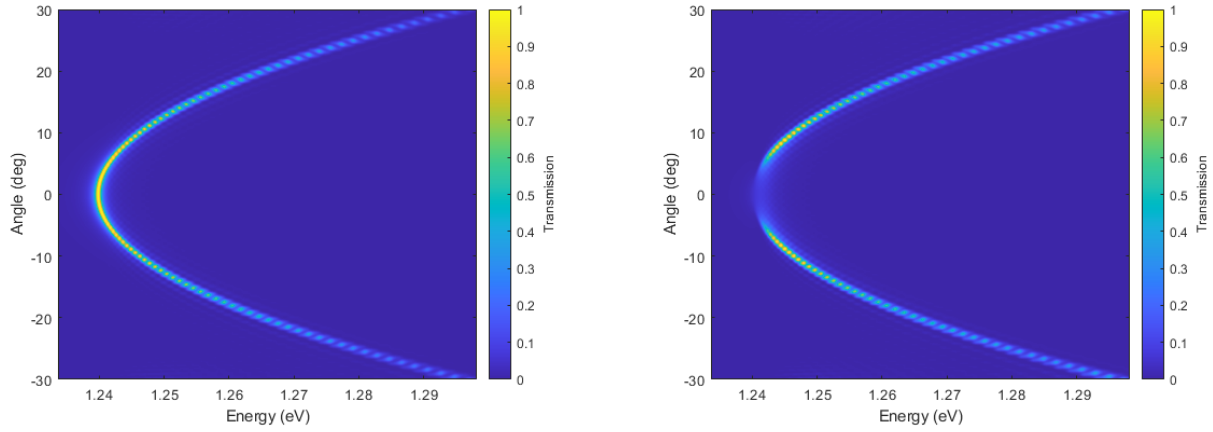

(a) (b)

Figure 5.30 (a) Simulated angle-dependent transmission for a 5-pair DBR cavity with an uniform refractive profile index in the center layer (b) Simulated angle-dependent transmission for the same cavity, with a modulation of the refractive index profile in the center layer (modulation depth $\Delta n/n_0 = -0.01$). The fast oscillations in the transmission intensity are interference artifacts arising from the finite size of the modelling domain and imperfect absorption by the SBC outside domain boundaries.

Results

When the angle-resolved transmission spectral map is recalculated with this modulation, an effect qualitatively very similar to what was observed in the experiments appears (Figures 5.30b, 5.31). As the refractive index modulation increases, shifting the mode energy up, the transmission at normal incidence is suppressed, the mode linewidth at normal incidence is broadened, and the transmission at higher angle increases. A modulation amplitude of $\Delta n/n_0 = -0.002$ is sufficient for the effect to appear in the simulated angle-dependent transmission spectra; modulation depths of up to $\Delta n = 0.01$ were simulated in order to demonstrate the changes more clearly.

The experimentally observed behaviour at high angle (linewidth narrowing, increased blueshift) is not perfectly reproduced, but this is not unexpected given the approximations used in this very simple model (no material dispersion, no energy dependence of the nonlinear response, nonlinear index modulation calculated from the linear electric field distribution). Nevertheless, the fact that this very simple model was able to reproduce the most important unexplained features in our experimental data supports the hypothesis that the intracavity negative Kerr lens causes significant changes in the cavity mode energy dispersion.

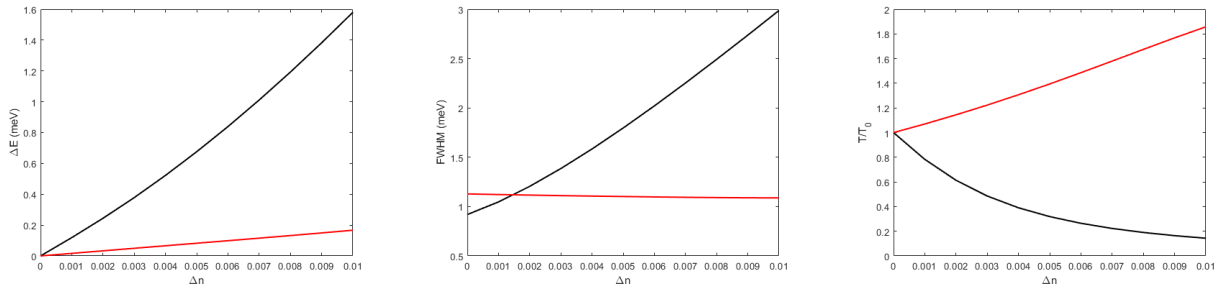

(a) Energy shift (b) Linewidth (c) Contrast modulation

Figure 5.31 Simulated cavity mode parameters at normal incidence (black) and 9 degrees (red) for the simple DBR cavity as a function of the refractive index transverse modulation depth.

This simulation was computed in the frequency-domain, calculating the propagation of a single frequency at a time, and would not have shown wave-mixing effects dependent on phase-matching between different frequencies.

To our knowledge, the effect observed here has not been previously described in the literature. It occurs in the specific case of a microcavity with a highly-nonlinear Kerr material being excited with a focused spot of broadband light, and becomes properly apparent only in angle-resolved transmission spectroscopy measurements.

The dramatic change in the angular and spectral transmission pattern could have applications as an optical switch, beam steering device or as an optically tunable spectral filter, and merits further investigation with more advanced numerical modelling. As the effect does not seem to depend on the cavity being in the strong-coupling regime, microcavities could be fabricated using only low-absorption dielectric materials, with a suitable low-loss and high Kerr-coefficient material such as amorphous silicon carbide [114] in the cavity center. If the absorption losses are low enough, the effect could be visible under CW excitation without thermal damage to the measurement spot, which would considerably reduce the complexity of numerical modelling of the results; a nonlinear 2D transfer-matrix formulation similar to [105] could be used to simulate a full 2D model of the microcavity including the Kerr effect and the Gaussian intensity profile of the probe beam. If a time-domain simulation is necessary, using the finite-difference time-domain (FDTD) method would be more resource-efficient and could allow a full 2D model to be solved in a reasonable amount of time[2]. There are FDTD models of the Kerr effect in Lorentz-dispersive materials which have been shown to be numerically stable, computationally-efficient, and accurate in the perturbative regime [115]. Both of these strategies are promising approaches for future numerical experiments to study the effect of a strong negative Kerr lens integrated into an optical microcavity, and examine its potential application to the development of new photonic devices.

[2]In this work, FEM modelling was used instead of FDTD for practical reasons of software license availability.

CHAPTER 6 SIMULATION OF COHERENT POLARITON DYNAMICS IN PEROVSKITE MICROCAVITIES

This chapter discusses a different project, led by our collaborator Dr. Wei Bao at the University of Nebraska-Lincoln. Dr. Bao's group developed a process for the *in-situ* growth of large defect-free single crystals of lead cesium bromide perovskite semiconductor material in high-quality-factor optical microcavities. This allowed them to measure high quality images of the real-space and Fourier space photoluminescence over large length scales, and to observe hydrodynamic phenomena characteristic of polariton condensates. In particular, the transition between normal flow and scatterless superfluid flow around a defect was observed at the polariton condensation threshold, and Čerenkov supersonic flow could be observed when polaritons were created with a sufficiently large in-plane momentum.

The author's contribution to this project was the numerical modelling of the experiments by implementing the driven-dissipative Gross-Pitaevskii equation in the COMSOL Multiphysics FEM software. Real-space time-integrated images of the polariton density were generated using the model for different sets of parameters corresponding to the experimental conditions, and showed a good agreement with the features observed experimentally.

The experiments and simulations presented in this chapter were published in reference [20] :

K. Peng, R. Tao, L. Haeberlé, Q. Li, D. Jin, G.R. Fleming, S. Kéna-Cohen, X. Zhang, and W. Bao, "Room-temperature quantum fluids in halide perovskites", Nature Communications, vol. 13, no. 7388 (2022). DOI : 10.1038/s41467-022-34987-y

Dr. Bao's group later demonstrated a XY Hamiltonian quantum simulator [116] based on a lattice of polariton condensates using high-quality perovskite microcavities. That work was supported by numerical models based on the ones developed in our group and discussed below.

6.1 Background

6.1.1 Metal halide perovskite semiconductors

Metal halide perovskites are a class of semiconductor materials with the chemical structure ABX_3 where A is an organic or alkali metal cation, B is a metal (typically lead or tin) and X is a halogen. Their electronic and optical properties have been extensively studied, as they are particularly well-suited to optoelectronic applications such as photovoltaic cells and light-emitting diodes [117] [118]. Many of the same properties also make them a promising material for exciton-polariton experiments [119] : they have a direct band gap with a large oscillator strength, a high exciton binding energy allowing experiments to be performed at room temperature, and a high exciton-exciton nonlinear interaction strength. These properties can be tuned to a certain extent by the choice of the A, B, and X components. In addition, metal halide perovskites are fabricated by solution processing, making experiments cheaper and faster than materials that require ultrahigh-vacuum slow crystal growth.

The specific perovskite material used in the experiments discussed in this chapter is cesium lead bromide ($CsPbBr_3$), with a band gap of 2.4eV and exciton binding energy of 36meV [120].

6.1.2 Microcavity fabrication and linear characterization

The microcavities were fabricated using a similar approach to what was done for our CNT laminated microcavities. High-quality DBR mirrors (SiO_2/Ta_2O_5, nine pairs) were grown on fused quartz wafers by electron beam evaporation. An array of square gold pillars was then patterned on top of the DBR surface, and two patterned wafers were aligned and joined together by thermal compression in a wafer bonding machine. The bonded wafers were then diced into cm-sized chips for individual microcavity fabrication. Each chip consists of a pair of high-quality mirrors, kept parallel and at a controlled spacing by the gold pillars. The quality factor of the empty cavities after wafer bonding and dicing was measured at approximately 900.

High-quality, large-size single crystals of cesium lead bromide ($CsPbBr_3$) were then grown inside of the empty cavities, using the inverse temperature crystallization method. A precursor solution of lead bromide and cesium bromide in dimethyl sulfoxide (DMSO) is prepared and allowed to fill the cavity by the capillary effect.

The cavity is then slowly heated on a hotplate, where the inverse temperature dependence of $CsPbBr_3$ in DMSO causes crystals to grow from the precursor solution. The method can produce single-crystal plates hundreds of micrometers wide, fully filling the gap between the mirrors (confirmed by measuring the crystal thickness by AFM on a debonded chip) and very low defect density (confirmed by a high PLQY and long PL lifetime). Crystals were also grown in "control" cavities using bonded quartz wafers without the reflective DBR coating, to perform absorption and photoluminescence measurements.

The polariton dispersion of the perovskite microcavities was measured using angle-resolved transmission spectroscopy (Figure 6.1). An interesting feature can be observed in the polariton energy dispersion : Due to the optical birefringence of the perovskite crystal, the effective cavity length is different for light polarized along the two in-plane principal axes of the crystal, lifting the degeneracy of the TE and TM modes at normal incidence. A full treatment of the light-matter coupling in this case needs to consider the TE-TM splitting at $k = 0$ in addition to the effective mass of the cavity photon in the TE and TM-polarizations. However, since all the experiments use a narrowband pump laser tuned to excite only the TE lower polariton, a simple coupled-oscillator model considering only the TE cavity mode is sufficient to describe the system. The exciton energy $E_X = 2406$meV is known from the absorption spectrum of a $CsPbBr_3$ single crystal grown in the same conditions as the microcavity crystal. The fitted parameters of the coupled-oscillator model are listed in table 6.1.

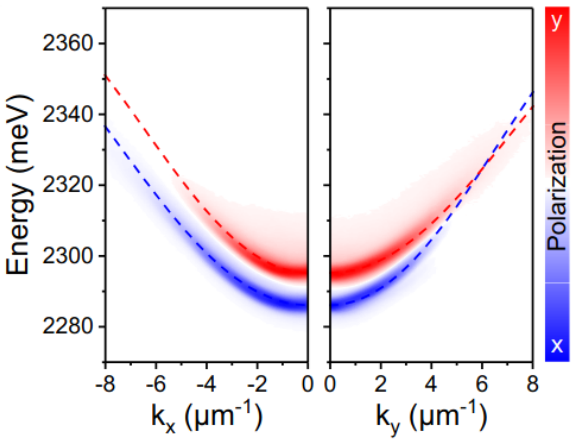

Figure 6.1 Angle-resolved transmission spectra of the microcavity, showing the TE-TM splitting due to the perovskite crystal's optical birefringence. The x and y directions are the crystal principal axes in the plane of the cavity. Reproduced from [20] under CC-BY 4.0 license.

Table 6.1 Fitted polariton parameters of the perovskite microcavity.

Parameter	Fitted value
Exciton-cavity mode detuning Δ	-71.1 meV
Rabi splitting $2\hbar\Omega_R$	151.4meV

6.1.3 Hydrodynamic measurements

The aim of the experiment was to observe and characterize two important nonlinear quantum hydrodynamic phenomena : superfluidity and Čerenkov supersonic flow. While room-temperature polariton condensation has been previously demonstrated in microcavities using $CsPbBr_3$ nanowires [121] and small single-crystal plates [122], superfluidity and supersonic flow had not been reported, because the observation of these hydrodynamic phenomena requires a very homogenous crystal over a much larger length scale.

Superfluidity is defined as the suppression of scattering in a quantum fluid [16]. When the polariton density is increased beyond the condensation threshold, polariton-polariton interactions will change the polariton energy dispersion, shifting it to higher energy and deforming its shape from a parabolic curve to a linear one [18]. This can be seen in plots of the polariton dispersion curve obtained by solving the GPE with the Bogoliubov approximation (Figure 6.2).

In this regime, superfluid flow is possible when the Landau criterion is respected : the group velocity v_p of the polariton fluid must be lower than the critical velocity of the system. The critical velocity here is the polariton speed of sound c_s (the speed at which polariton-polariton interactions can propagate energy through the fluid), which depends on the polariton density $|\Psi|^2$, polariton-polariton interaction potential g, and polariton effective mass m_{LP}.

$$c_s = \sqrt{\frac{g|\Psi|^2}{m_{LP}}} \tag{6.1}$$

When the Landau criterion is respected, there are no available states on the energy dispersion curve for polaritons to scatter to, and they propagate around obstacles without interacting with them.

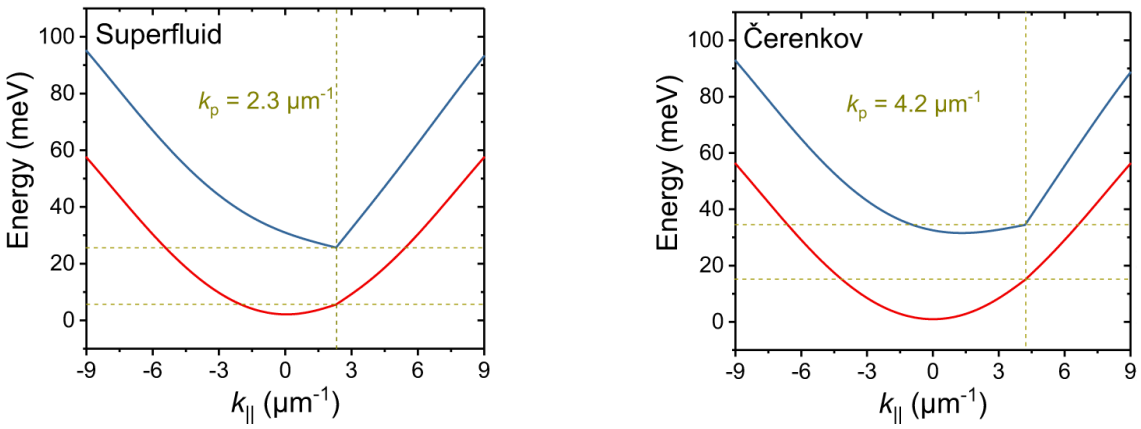

(a) (b)

Figure 6.2 Bogoliubov excitation spectra calculated at low (red) and high (blue) pump intensity. (a) When the $\mathbf{k}_p$ is small enough to fulfill the Landau criterion, there are no possible states for condensate polaritons to scatter to when encountering an obstacle. (b) When $\mathbf{k}_p$ is large enough to violate the Landau criterion, although the dispersion shape is still strongly modified by polariton-polariton interactions, there are lower-energy states that condensate polaritons can scatter to. Reproduced (adapted) from [20] under CC-BY 4.0 license.

Both v_p and c_s can be controlled experimentally. Using a resonant pump with an in-plane momentum k_p (determined by the incidence angle of the pump beam), the polariton group velocity is given by $v_p = \hbar k_p / m_{LP}$. The polariton density is tuned by simply changing the intensity of the pump with a variable attenuator, which in turns controls the polariton speed of sound c_s.

Two series of experiments were performed using two different pump wavevectors k_p. In both experiments, the pump energy was tuned to be slightly blue-shifted (by an amount $\approx$ 5meV) with respect to the polariton mode energy at k_p, in order to efficiently excite the lower polariton mode after its energy dispersion has been shifted by polariton-polariton interactions. A short-pulse pump (250fs pulses from an optical parametric amplifier) was used in order to allow the polariton state to evolve freely after the initial excitation. An localized defect was artificially created in the $CsPbBr_3$ crystal by burning a μm-sized spot with a tightly-focused nonresonant pump beam. The flow of the polariton fluid around this defect could then be observed using real-space and Fourier imaging in a transmission geometry, using one objective lens for the injection of the pump and another objective lens for the imaging.

In the first series of experiments, aiming to observe superfluid flow, the value of $k_p = 2.3\mu\text{m}^{-1}$ was sufficiently low to fulfill the Landau criterion. Images of the polariton density were measured at different values of pump fluence, and two regimes could be observed (Figure 6.3). At low fluence, there are parabolic interference fringes in front of the defect, caused by back-scattered polaritons, as well as a shadow trailing behind the defect. As the pump fluence is increased beyond the polariton condensation threshold, both of these features are strongly suppressed, indicating scatterless flow around the defect.

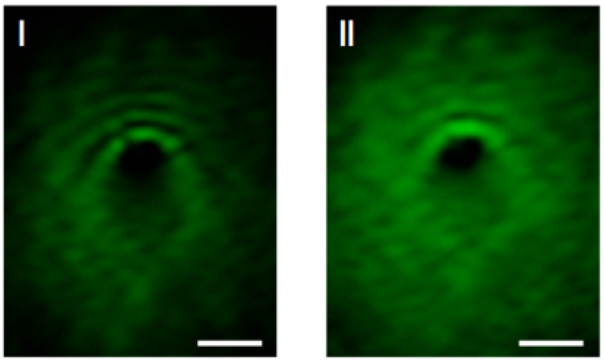

Figure 6.3 Real-space image of the polariton density for an injected pump wavevector of $k_p = 2.3\mu\text{m}^{-1}$ and a fluence of 0.07 (I) and 6 (II) $\mu\text{J/cm}^2$. Scale bar 5μm. Reproduced from [20] under CC-BY 4.0 license.

In the second series of experiments, aiming to observe Čerenkov supersonic flow, the value of k_p was increased to $4.2\mu\text{m}^{-1}$ in order to violate the Landau criterion. This time, as the pump fluence was increased, the interference fringes were not suppressed, but transitioned from a parabolic to a linear shape (Čerenkov pattern) characteristic of supersonic flow (Figure 6.4).

With increasing pump fluence, an increase of the aperture half-angle of the linear fringe pattern (Mach cone angle ϕ) was observed. ϕ is determined by the Mach number (the ratio between the fluid velocity and the sound velocity) according to the relation [16]

$$\sin\phi = \frac{c_s}{v_p} \tag{6.2}$$

The polariton speed of sound was calculated from the observed Mach cone angle in Figure 6.4 and determined to be 10.4 μm/ps, which confirms that the Landau criterion is violated since the polariton group velocity $v_p = \hbar k_p / m_{LP} = 17\mu$m/ps is larger than c_s.

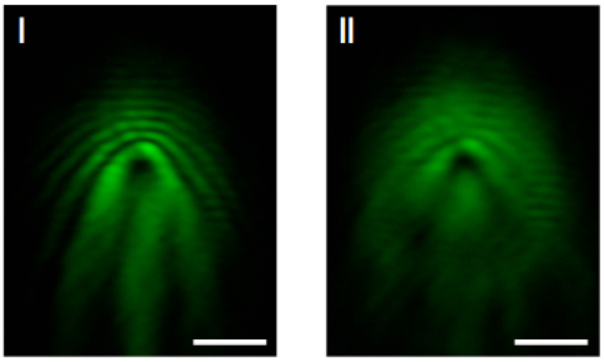

Figure 6.4 Real-space image of the polariton density for an injected pump wavevector of $k_p = 4.2\mu\text{m}^{-1}$ and a fluence of 0.06 (I) and 5.6 (II) $\mu\text{J/cm}^2$. Scale bar 5μm. Reproduced from [20] under CC-BY 4.0 license.

6.2 Numerical modelling of the polariton fluid dynamics

6.2.1 Driven-dissipative GPE

The Gross-Pitaevskii equation describes the dynamics of a fluid of weakly-interacting bosons (see section 2.1.4). In the case where the Rabi frequency Ω_R is much larger than the other energy scales of the system (polariton kinetic and interaction energies, LP-pump detuning), the GPE can be simplified [16] by only considering the time evolution of the lower polariton field $\Psi(\mathbf{r}, t)$:

$$i\hbar\frac{\partial\Psi(\mathbf{r},t)}{\partial t} = \left(\hbar\omega_{LP} - \frac{\hbar^2\nabla^2}{2m_{LP}} - \frac{i\hbar\gamma_{LP}}{2} + g|\Psi(\mathbf{r},t)|^2 + V(\mathbf{r})\right)\Psi(\mathbf{r},t) + \hbar P(\mathbf{r},t) \tag{6.3}$$

In equation 6.3, the lower polariton mode energy is described using a parabolic dispersion with the rest energy $\hbar\omega_{LP} = 2.2368$ eV and effective mass $m_{LP} = 2.56 \cdot 10^{-35}$ kg fitted from the measured angle-dependent transmission data. The polariton decay rate $\gamma_{LP} = 2.87$ ps^{-1} is calculated from the measured linewidth of the mode. The polariton-polariton interaction potential is parametrized by the constant $g = 0.5\ \mu\text{eV} \cdot \mu\text{m}^2$, which can be determined by the slope of the measured LP mode energy blueshift with respect to the polariton density. $V(\mathbf{r})$ is the potential of the scattering defect. Finally, the driving term $P(\mathbf{r}, t)$ represents the rate of creation of polaritons by the pump.

The pump pulse is expressed as a plane wave of frequency ω_p with a Gaussian temporal and spatial envelope and peak amplitude F_p :

$$P(\mathbf{r},t) = F_p e^{(i(\mathbf{k_p}\cdot\mathbf{r}-\omega_p t))}\ e^{-\frac{(t-t_0)^2}{2\sigma_t^2}}\ e^{-\frac{|\mathbf{r}|^2}{2\sigma_r^2}} \tag{6.4}$$

where the widths $\sigma_{t,r}$ are related to the FWHM by $\sigma = FWHM/(2\sqrt{2\ln(2)})$. The pump spot FWHM (fitted from the real-space images) was 16μm for the Čerenkov experiments and 24μm for the superfluidity experiment. The laser pulse temporal FWHM was 250fs.

The amplitude F_p of the driving term is related to the pump laser pulse peak intensity by the expression

$$F_p = C_p\sqrt{\frac{\gamma_{LP} I_0}{2\hbar\omega_p}} \tag{6.5}$$

derived from input-output theory [19] [123], where C_p is the Hopfield coefficient corresponding to the photon fraction of the lower polariton state at the pump momentum k_p (calculated from the coupled-oscillator model fitted to the measured angle-dependent transmission). The pump pulse peak intensity is calculated from the measured pump fluence F_0 with $I_0 = F_0/(\sigma_t\sqrt{\pi})$.

6.2.2 Numerical setup

To simulate the polariton hydrodynamic phenomena observed in the perovskite microcavities, equation 6.3 was implemented in the COMSOL Multiphysics FEM software using the General Form PDE interface. The lateral size of the simulation domain was set at 100μm. This provides a sufficient space for the polaritons created at the center of the domain to decay before reaching the edge, avoiding numerical artefacts from edge reflections in the results. Similarly, the total duration of the simulation is set to 3500fs, corresponding to five times the polariton lifetime after the end of the pump pulse, in order to let the polaritons from the pump pulse decay completely.

The scattering defect was modelled as a circular region in the center of the domain (diameter 0.8μm in the case of the Čerenkov simulations and 2.2μm for the superfluidity simulations) where the potential $V(\mathbf{r})$ was set to 50meV, about twice the polariton kinetic energy. This value was arbitrarily chosen to provide a sufficient potential barrier to induce scattering on the plariton fluid on the defect. Outside of the defect region, $V(\mathbf{r}) = 0$. In addition, since the cavity is damaged in the defect spot, the polariton decay rate in the defect region was set to $100 \cdot \gamma_{LP}$. Once again, this is an arbitrarily large value, in order to destroy the polaritons created by the pump inside the defect region.

The simulation domain was meshed with triangular elements with a maximal size of 100nm. The mesh element size and the polariton group velocity $v_{g,\,LP} = \hbar k_p / m_{LP} \approx 17\mu$m/ps determine the maximum size of time step that can be used by the solver to ensure numerical stability according to the CFL criterion (discussed in section 5.3.3). When using a solver step size of 1fs, the CFL number is 0.17 which is acceptable.

After the numerical model has been solved for a given pump fluence and wavevector, the solution $\Psi(\mathbf{r}, t)$ contains the time evolution of the polariton field complex amplitude. What was experimentally measured was the time-averaged intensity, as the detector response is much slower than the timescale of the polariton dynamics. To properly compare the simulation with the experimental data, the solution is integrated to give the time-averaged polariton density

$$|\Psi(\mathbf{r})|^2 = \frac{1}{T} \int_0^T \Psi^*(\mathbf{r}, t)\, \Psi(\mathbf{r}, t)\, \mathrm{d}t \tag{6.6}$$

where $T = 3500$fs is the total simulation duration.

6.2.3 Results

Superfluid flow

The first series of simulations aims to reproduce the superfluidity experiment, by using a pump wavevector of $2.3\mu\text{m}^{-}1$. The time-averaged polariton polariton density maps for pump fluences below and above the condensation threshold (Figure 6.5) clearly show the transition to superfluid flow. At low polariton density, the polaritons are back-scattered on the defect, leading to density oscillations in front of the defect from the interference between the forward-propagating and back-scattered polaritons. There is also a shadow or region of low polariton density behind the defect. When the pump fluence is increased, the intensity envelope of the interference wavefronts and length that the shadow extends in the wake of the defect are both reduced, This is a signature of the transition to a scatterless flow characteristic of the superfluid state. The difference is made more visible in one-dimensional cuts of the polariton density across the defect (Figure 6.6). Note that while the interference fringes and shadow are suppressed at high fluence, they do not disappear completely (this is also the case in the experimental data in Figure 6.3). This is mainly due to the fact that polariton density is integrated over time, and contains contributions from the leading and trailing edge of the pulse (below threshold) even when the peak intensity of the pulse is above threshold.

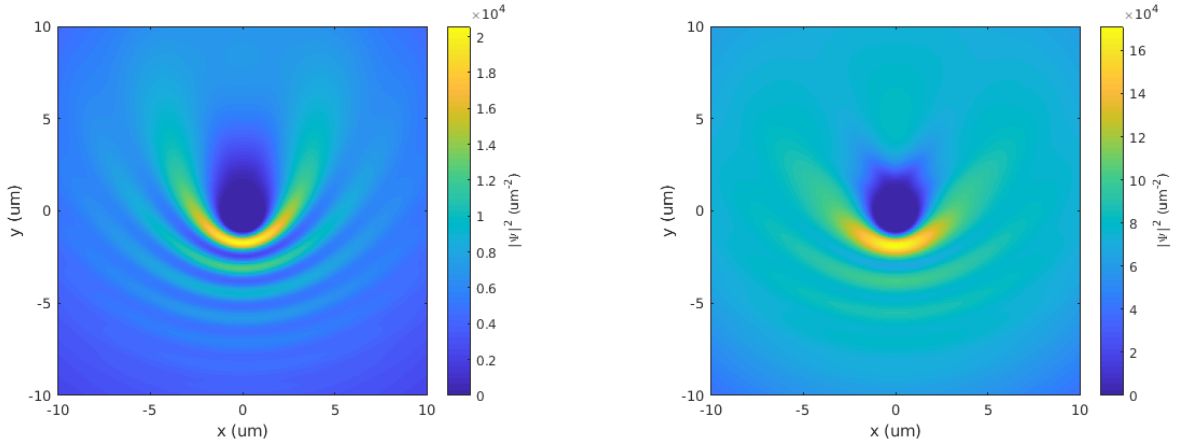

Figure 6.5 Simulated time-averaged polariton density $|\Psi(\mathbf{r})|^2$ for an injected pump wavevector of $k_p = 2.3\mu\text{m}^{-1}$ (a) below and (b) above the condensation threshold.

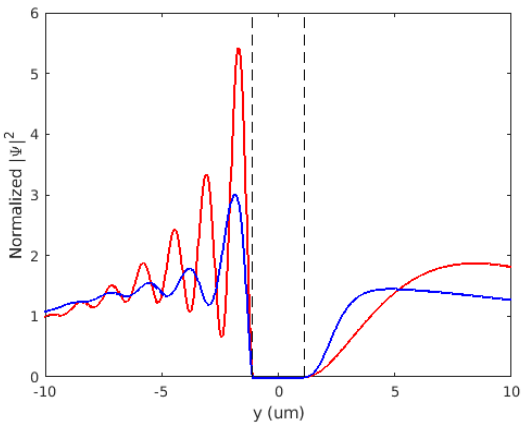

Figure 6.6 Normalized simulated time-averaged polariton density profile across the defect below (red curve) and above (blue curve) the condensation threshold. The pump in-plane momentum is $k_p = 2.3\ \mu\text{m}^{-1}$. The position of the defect (dashed black lines) is also shown for reference.

Čerenkov supersonic flow

The second series of simulations aims to reproduce the Čerenkov experiment, by using a pump wavevector of $4.2\mu\text{m}^{-1}$. The time-averaged polariton polariton density maps for pump fluences below and above the condensation threshold (Figure 6.9) show the transition from subsonic to supersonic flow. At low polariton density, a parabolic interference wavefront is produced in front of the defect, similar to the below-threshold results of the first simulation. As the pump fluence is increased, the interference fringes are not suppressed, but transition to a linear shape (Čerenkov pattern). The aperture angle of the Mach cone increases at higher pump fluence, as the higher polariton density translate to a higher speed of sound, and a higher c_s/v_p ratio.

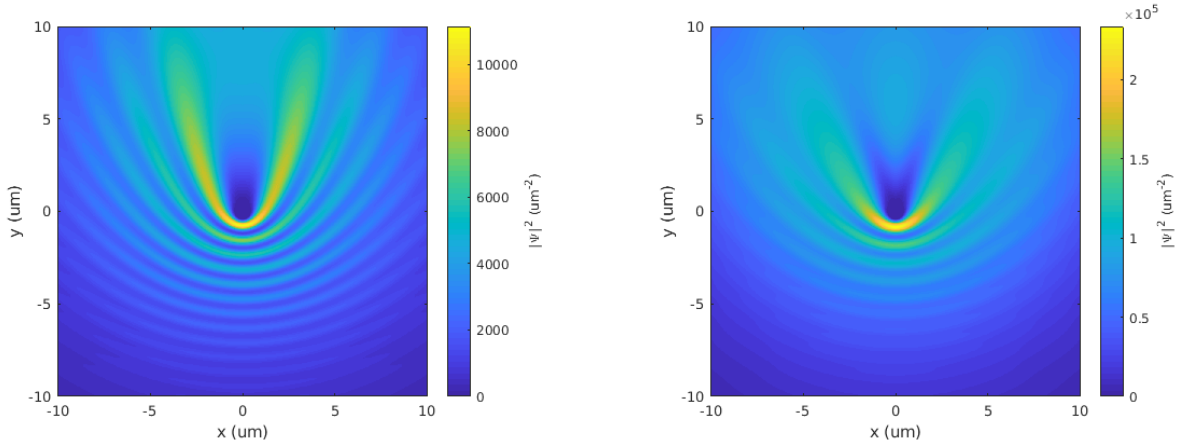

(a) (b)

Figure 6.7 Simulated time-averaged polariton density $|\Psi(\mathbf{r})|^2$ for an injected pump wavevector of $k_p = 4.2\mu\text{m}^{-1}$ (a) below and (b) above the condensation threshold.

6.2.4 Optimized simulation parameters

After we provided the initial simulation results, which qualitatively reproduced the observed features of the experimental data, Kai et al. [20] further refined the model by adjusting the polariton parameters m_{LP}, ω_{LP}, γ_{LP} to more accurate values. The results from the updated model (Figures 6.8, 6.9) show better quantitative agreement with the experimental data, with a remaining scale factor ~ 5 between the simulated and measured fluences. This is attributable to the approximations inherent to the calculation of the polariton density in the simulation, and to the fact that the numerical model uses the peak fluence, while the experimentally measured fluence is the mean value (averaged over the spot size). The aperture half-angle of the Mach cone in Figure 6.9b was 38 degrees, corresponding to a polariton speed of sound $c_s = 10.6\mu\text{m/ps}$ close to the experimentally-measured value. In the optimized model, small-amplitude (5meV) random fluctuations of the external potential $V(\mathbf{r})$ were added in order to better reproduce the appearance of the measured polariton density images.

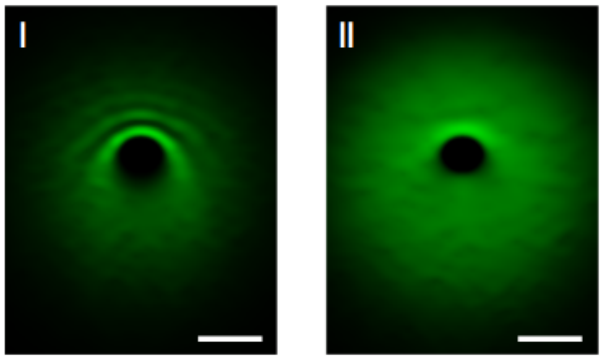

Figure 6.8 Simulated time-averaged polariton density $|\Psi(\mathbf{r})|^2$ with optimized polariton parameters and random fluctuations of $V(\mathbf{r})$ for an injected pump wavevector of $k_p = 2.3\mu\text{m}^{-1}$ and a fluence of 3.5 (I) and 35 (II) $\mu\text{J/cm}^2$. Scale bar 5μm. Reproduced from [20] under CC-BY 4.0 license.

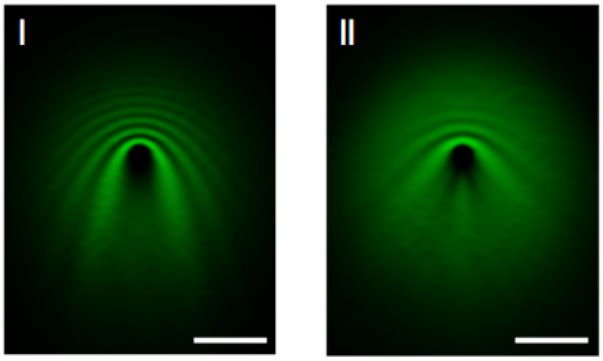

Figure 6.9 Simulated time-averaged polariton density $|\Psi(\mathbf{r})|^2$ with optimized polariton parameters and random fluctuations of $V(\mathbf{r})$ for an injected pump wavevector of $k_p = 4.2\mu\text{m}^{-1}$ and a fluence of 3.5 (I) and 35 (II) $\mu\text{J/cm}^2$. Scale bar 5μm. Reproduced from [20] under CC-BY 4.0 license.

6.3 Discussion

By using an in-cavity crystal growth method, Peng *et al.* were able to fabricate cavities containing sufficiently large and uniform single crystals of $CsPbBr_3$ to demonstrate superfluid and Čerenkov supersonic flow of a polariton fluid. The finite-element-model numerical simulation of the driven-dissipative Gross-Pitaevskii equation that we developed was able to reproduce the experimentally observed features of the real-space images for both polariton flow regimes, using the experimentally-measured values for the polariton dispersion and polariton-polariton interaction potential.

CHAPTER 7 CONCLUSION

7.1 Summary of Works

By exploiting a novel fabrication method developed by the Arnold group at UWM, very high concentration CNT thin films could be integrated into high quality factor optical microcavities. We have demonstrated ultrastrong coupling in metal-mirror cavities, with a normalized coupling exceeding the previous highest-reported value for Wannier-Mott excitons. We were also able to demonstrate strong coupling of the phonon-assisted K-dark exciton transition with the cavity mode.

In DBR-mirror cavities, we demonstrated the narrowest CNT polariton linewidth yet reported. We performed CW and pulsed PL measurements on the DBR cavities and found that the maximum attainable polariton density was severely limited by the large exciton-exciton annihilation rate. Due to these constraints, we could not reach the polariton condensation threshold, even at cryogenic temperatures. Furthermore, we observed rapid degradation of the polariton PL emission under continuous pumping, which we attribute to the photoexcited formation of quenching sp^3 defects.

Resonant excitation of DBR-mirror polariton cavities with a supercontinuum probe allowed us to observe nonlinear effects below the condensation threshold, such as a shift of the polariton energy with increasing fluence. A numerical time-domain model of the nonlinear optical response of the cavity was developed, and was able to reproduce the observed energy shift in the perturbative regime (before the saturation of the Kerr effect). However, other features in the measured angle-resolved spectra were not explained by the model, namely a broadening of the mode linewidth, a strong suppression of the transmission at normal incidence, and a increase of the transmission at larger angle.

Additional simulations allowed us to identify the mechanism driving these changes as the formation of an intracavity Kerr lens. The specific case of an intracavity Kerr lens in a microcavity excited by a diffraction-limited focused spot had not been previously reported in the literature, and merits further investigation.

Finally, an finite-element model implementing the driven-dissipative Gross-Pitaevskii equation was developed, and could fully reproduce the observed hydrodynamic phenomena experimentally observed by collaborators in a polariton condensate using a DBR microcavity containing a large defect-free $CsPbBr_3$ perovskite single crystal.

7.2 Limitations

The results of the photoluminescence and blueshift experiments show that the initial strategy aiming to maximize CNT concentration and cavity quality factor is not optimal for achieving the initial goal (demonstrating polariton condensation). The very high concentration used in our samples came with a number of drawbacks, including low reproducibility of film thickness, low uniformity, high scattering losses, and low PLQY. The high cavity mode quality factor combined with the high losses of the CNT material meant that the polariton mode contrast was very small. This made it very difficult to resolve the mode with good SNR with the available instruments.

One of the initial arguments motivating the use of CNTs for polariton microcavities was their high photostability compared with organic dyes. In our vacuum-filtered samples, we observed the opposite : the rapid and irreversible photoinduced degradation of PLQY is a major issue for polariton devices, and should be investigated further.

The developed time-domain-model of the polariton cavity with the Duffing equations is computationally expensive, and had to be defined on one dimension due to constraints on the available memory and processing power. To fully simulate the angle-resolved transmission spectrum, a two-dimensional description is required. The model needs to be considerably optimized to make this possible. A numerical approach based on the FDTD method is likely to prove faster and more efficient.

Finally, a better characterization of the nonlinear response of the CNT film material will be essential to build accurate models of the nonlinear response of CNT microcavities. In this work, only a few datapoints at one wavelength could be measured, as the material degraded in storage. However, in future experiments, this could be avoided simply by performing all the characterization immediately after sample fabrication.

If accurate measurements of the material nonlinear absorption can be obtained, the numerical model could be extended to include the imaginary nonlinear susceptibility, enabling the simulation of polariton cavities with close to zero detuning.

7.3 Future Research

To better determine the optimal parameters for CNT polariton microcavities, the influence of concentration on key metrics such as PLQY, exciton linewidth, background absorption, scattering losses, and uniformity/morphology should be systematically characterized. The constraints on the cavity quality factor could also be relaxed; it is not useful to have extremely reflective mirrors when the material absorption and scattering losses outweigh the mirror losses by several orders of magnitude. A cavity with moderate quality factor would allow easier measurement of the angle-resolved spectra and be cheaper to fabricate. Similarly, if reducing the CNT concentration improves the material properties and the ease of sample fabrication at the cost of reduced coupling strength, that could be an acceptable trade-off as long as we remain firmly in the strong-coupling regime.

The cause of the photoinduced PLQY degradation should be investigated, and side-by-side comparisons of the photostability of dropcast and vacuum-filtered films should be performed to confirm our observation that the degradation seems much worse in the vacuum-filtered material.

As the low PLQY of CNTs is a major limiting factor in achieving polariton condensation, it would be very interesting to use CNTs functionalized with sp^3 luminescent defects to improve the polariton population rate in our high quality factor DBR microcavities, as was demonstrated by Lüttgens et al. in metal-mirror microcavities [61].

The use of functionalized CNTs using engineered defect sites to localize the excitons also suggests the possibility of modifying exciton-exciton annihilation dynamics. For a given EEA cross-section, if the excitons are localized instead of diffusing freely along the tube, the annihilation rate should be reduced, but this has never been measured. A comparison of EEA coefficients between pristine and functionalized CNT thin films of identical concentration would be a relatively simple and potentially very impactful experiment.

Finally, the large observed changes in the transmitted angular intensity pattern of a nonlinear microcavity as a result of intracavity Kerr lensing are a novel effect that should be investigated further, although it is unrelated to strong light-matter coupling. Additional simulations accurately modelling the Kerr lens in a numerically self-consistent manner could determine if there are any useful applications for optical switching or optically actuated beam steering. A recently developed nonlinear transfer-matrix method that supports inhomogeneity in the transverse direction [105] would be well-suited to this problem.

REFERENCES

[1] D. N. Basov, A. Asenjo-Garcia, P. J. Schuck, X. Zhu, and A. Rubio, "Polariton panorama," *Nanophotonics*, vol. 10, no. 1, p. 549–577, Nov. 2020.

[2] N. W. Ashcroft and N. D. Mermin, *Solid state physics*. Brooks/Cole, 1976.

[3] J. Chmeliov, J. Narkeliunas, M. W. Graham, G. R. Fleming, and L. Valkunas, "Exciton-exciton annihilation and relaxation pathways in semiconducting carbon nanotubes," *Nanoscale*, vol. 8, pp. 1618–1626, 1 2016.

[4] S. Alvarado, P. Seidler, D. Lidzey, and D. Bradley, "Direct determination of the exciton binding energy of conjugated polymers using a scanning tunneling microscope," *Physical Review Letters*, vol. 81, no. 5, p. 1082–1085, Aug. 1998.

[5] P. Y. Yu and M. Cardona, *Fundamentals of Semiconductors: Physics and Materials Properties*. Springer Berlin Heidelberg, 2010.

[6] M. Soltani, S. Yegnanarayanan, and A. Adibi, "Ultra-high Q planar silicon microdisk resonators for chip-scale silicon photonics," *Optics Express*, vol. 15, no. 8, p. 4694, 2007.

[7] M. L. Gorodetsky, A. A. Savchenkov, and V. S. Ilchenko, "Ultimate Q of optical microsphere resonators," *Optics Letters*, vol. 21, no. 7, p. 453, Apr. 1996.

[8] W. Bogaerts, P. De Heyn, T. Van Vaerenbergh, K. De Vos, S. Kumar Selvaraja, T. Claes, P. Dumon, P. Bienstman, D. Van Thourhout, and R. Baets, "Silicon microring resonators," *Laser & Photonics Reviews*, vol. 6, no. 1, p. 47–73, Sep. 2011.

[9] S. Hu and S. M. Weiss, "Design of photonic crystal cavities for extreme light concentration," *ACS Photonics*, vol. 3, no. 9, p. 1647–1653, Aug. 2016.

[10] S. Kim, J. E. Fröch, J. Christian, M. Straw, J. Bishop, D. Totonjian, K. Watanabe, T. Taniguchi, M. Toth, and I. Aharonovich, "Photonic crystal cavities from hexagonal boron nitride," *Nature Communications*, vol. 9, no. 1, Jul. 2018.

[11] Thorlabs Inc., *Single-Crystal Supermirrors*, 2025. [Online]. Available: https://www.thorlabs.com/newgrouppage9.cfm?objectgroup_ID=14069

[12] A. Kavokin, J. J. Baumberg, G. Malpuech, and F. P. Laussy, *Microcavities*. Oxford University Press, 2017.

[13] C. Ciuti, P. Schwendimann, and A. Quattropani, "Theory of polariton parametric interactions in semiconductor microcavities," *Semiconductor Science and Technology*, vol. 18, no. 10, p. S279–S293, Sep. 2003.

[14] S. Kéna-Cohen, S. A. Maier, and D. D. C. Bradley, "Ultrastrongly coupled exciton–polaritons in metal-clad organic semiconductor microcavities," *Advanced Optical Materials*, vol. 1, no. 11, p. 827–833, Aug. 2013.

[15] D. Bajoni, "Polariton lasers. hybrid light–matter lasers without inversion," *Journal of Physics D: Applied Physics*, vol. 45, no. 31, p. 313001, Jul. 2012.

[16] I. Carusotto and C. Ciuti, "Quantum fluids of light," *Reviews of Modern Physics*, vol. 85, pp. 299–366, 2 2013.

[17] T. Guillet and C. Brimont, "Polariton condensates at room temperature," *Comptes Rendus Physique*, vol. 17, no. 8, p. 946–956, Oct. 2016.

[18] T. Byrnes, N. Y. Kim, and Y. Yamamoto, "Exciton-polariton condensates," pp. 803–813, 11 2014.

[19] G. Lerario, A. Fieramosca, F. Barachati, D. Ballarini, K. S. Daskalakis, L. Dominici, M. De Giorgi, S. A. Maier, G. Gigli, S. Kéna-Cohen, and et al., "Room-temperature superfluidity in a polariton condensate," *Nature Physics*, vol. 13, no. 9, p. 837–841, Jun 2017.

[20] K. Peng, R. Tao, L. Haeberlé, Q. Li, D. Jin, G. R. Fleming, S. Kéna-Cohen, X. Zhang, and W. Bao, "Room-temperature polariton quantum fluids in halide perovskites," *Nature Communications*, vol. 13, no. 1, Nov 2022.

[21] K. G. Lagoudakis, M. Wouters, M. Richard, A. Baas, I. Carusotto, R. André, L. S. Dang, and B. Deveaud-Plédran, "Quantized vortices in an exciton–polariton condensate," *Nature Physics*, vol. 4, no. 9, p. 706–710, Aug. 2008.

[22] S. Kim, B. Zhang, Z. Wang, J. Fischer, S. Brodbeck, M. Kamp, C. Schneider, S. Höfling, and H. Deng, "Coherent polariton laser," *Physical Review X*, vol. 6, no. 1, Mar. 2016.

[23] C. Schneider, A. Rahimi-Iman, N. Y. Kim, J. Fischer, I. G. Savenko, M. Amthor, M. Lermer, A. Wolf, L. Worschech, V. D. Kulakovskii, I. A. Shelykh, M. Kamp, S. Reitzenstein, A. Forchel, Y. Yamamoto, and S. Höfling, "An electrically pumped polariton laser," *Nature*, vol. 497, no. 7449, p. 348–352, May 2013.

[24] M. D. Fraser, S. Höfling, and Y. Yamamoto, "Physics and applications of exciton–polariton lasers," *Nature Materials*, vol. 15, no. 10, p. 1049–1052, Sep 2016.

[25] J. Kasprzak, M. Richard, S. Kundermann, A. Baas, P. Jeambrun, J. M. Keeling, F. M. Marchetti, M. H. Szymańska, R. André, J. L. Staehli, and et al., "Bose–einstein condensation of exciton polaritons," *Nature*, vol. 443, no. 7110, p. 409–414, Sep 2006.

[26] J. Keeling and N. G. Berloff, "Exciton–polariton condensation," *Contemporary Physics*, vol. 52, no. 2, p. 131–151, Mar. 2011.

[27] M. Richard, J. Kasprzak, R. Romestain, R. André, and L. S. Dang, "Spontaneous coherent phase transition of polaritons in cdte microcavities," *Physical Review Letters*, vol. 94, no. 18, May 2005.

[28] M. Gomez-Dominguez, E. J. Kumar, K. A. Koch, A. R. Srimath Kandada, and J.-P. Correa-Baena, "Materials and cavity design principles for exciton-polariton condensates," *ACS Nano*, vol. 19, no. 11, p. 10579–10588, Mar. 2025.

[29] R. T. Grant, P. Michetti, A. J. Musser, P. Gregoire, T. Virgili, E. Vella, M. Cavazzini, K. Georgiou, F. Galeotti, C. Clark, J. Clark, C. Silva, and D. G. Lidzey, "Efficient radiative pumping of polaritons in a strongly coupled microcavity by a fluorescent molecular dye," *Advanced Optical Materials*, vol. 4, no. 10, p. 1615–1623, Jul. 2016.

[30] F. Tassone, C. Piermarocchi, V. Savona, A. Quattropani, and P. Schwendimann, "Bottleneck effects in the relaxation and photoluminescence of microcavity polaritons," *Physical Review B*, vol. 56, no. 12, p. 7554–7563, Sep. 1997.

[31] H. Deng, H. Haug, and Y. Yamamoto, "Exciton-polariton bose-einstein condensation," *Reviews of Modern Physics*, vol. 82, no. 2, p. 1489–1537, May 2010.

[32] O. Voronych, A. Buraczewski, M. Matuszewski, and M. Stobińska, "Numerical modeling of exciton–polariton bose–einstein condensate in a microcavity," *Computer Physics Communications*, vol. 215, p. 246–258, Jun. 2017.

[33] R. Zhang, Y. Zhang, and F. Wei, "Controlled synthesis of ultralong carbon nanotubes with perfect structures and extraordinary properties," *Accounts of Chemical Research*, vol. 50, no. 2, p. 179–189, Feb 2017.

[34] S. Iijima, "Helical microtubules of graphitic carbon," *Nature*, vol. 354, no. 6348, p. 56–58, Nov 1991.

[35] A. R. Amori, Z. Hou, and T. D. Krauss, "Excitons in single-walled carbon nanotubes and their dynamics," *Annual Review of Physical Chemistry*, vol. 69, no. 1, p. 81–99, Apr 2018.

[36] M. S. Arnold, J. L. Blackburn, J. J. Crochet, S. K. Doorn, J. G. Duque, A. Mohite, and H. Telg, "Recent developments in the photophysics of single-walled carbon nanotubes for their use as active and passive material elements in thin film photovoltaics," *Physical Chemistry Chemical Physics*, vol. 15, no. 36, p. 14896–14918, Jul 2013.

[37] V. Perebeinos, J. Tersoff, and P. Avouris, "Scaling of excitons in carbon nanotubes," *Physical Review Letters*, vol. 92, no. 25, Jun. 2004.

[38] S. Reich, C. Thomsen, and J. Maultzsch, *Carbon Nanotubes: Basic Concepts and Physical Properties*. Wiley, 2008.

[39] C. Mann and T. Hertel, "13 nm exciton size in (6,5) single-wall carbon nanotubes," *The Journal of Physical Chemistry Letters*, vol. 7, no. 12, p. 2276–2280, Jun 2016.

[40] L. Lüer, S. Hoseinkhani, D. Polli, J. Crochet, T. Hertel, and G. Lanzani, "Size and mobility of excitons in (6, 5) carbon nanotubes," *Nature Physics*, vol. 5, no. 1, p. 54–58, Nov. 2008.

[41] V. Perebeinos, J. Tersoff, and P. Avouris, "Radiative lifetime of excitons in carbon nanotubes," *Nano Letters*, vol. 5, no. 12, p. 2495–2499, Nov. 2005.

[42] O. N. Torrens, M. Zheng, and J. M. Kikkawa, "Energy of K-momentum dark excitons in carbon nanotubes by optical spectroscopy," *Physical Review Letters*, vol. 101, no. 15, Oct. 2008.

[43] V. Perebeinos, J. Tersoff, and P. Avouris, "Effect of exciton-phonon coupling in the calculated optical absorption of carbon nanotubes," *Physical Review Letters*, vol. 94, no. 2, Jan. 2005.

[44] J. L. Blackburn, J. M. Holt, V. M. Irurzun, D. E. Resasco, and G. Rumbles, "Confirmation of K-momentum dark exciton vibronic sidebands using ^{13}C-labeled, highly enriched (6,5) single-walled carbon nanotubes," *Nano Letters*, vol. 12, no. 3, p. 1398–1403, Feb 2012.

[45] A. Dhavamani, L. Haeberlé, J. Wang, S. Kéna-Cohen, and M. S. Arnold, "Cavity-mediated hybridization of bright and dark excitons in an ultrastrongly coupled carbon nanotube microcavity," *ACS Photonics*, vol. 8, no. 8, p. 2375–2383, Jul 2021.

[46] A. Graf, Y. Zakharko, S. P. Schießl, C. Backes, M. Pfohl, B. S. Flavel, and J. Zaumseil, "Large scale, selective dispersion of long single-walled carbon nanotubes with high photoluminescence quantum yield by shear force mixing," *Carbon*, vol. 105, pp. 593–599, 8 2016.

[47] A. Ishii, M. Yoshida, and Y. K. Kato, "Exciton diffusion, end quenching, and exciton-exciton annihilation in individual air-suspended carbon nanotubes," *Physical Review B - Condensed Matter and Materials Physics*, vol. 91, 3 2015.

[48] T. Hertel, S. Himmelein, T. Ackermann, D. Stich, and J. Crochet, "Diffusion limited photoluminescence quantum yields in 1-D semiconductors: Single-wall carbon nanotubes," *ACS Nano*, vol. 4, no. 12, p. 7161–7168, Nov. 2010.

[49] J. Zaumseil, "Luminescent defects in single-walled carbon nanotubes for applications," *Advanced Optical Materials*, vol. 10, no. 2, Nov. 2021.

[50] J. J. Crochet, J. G. Duque, J. H. Werner, and S. K. Doorn, "Photoluminescence imaging of electronic-impurity-induced exciton quenching in single-walled carbon nanotubes," *Nature Nanotechnology*, vol. 7, no. 2, p. 126–132, Jan. 2012.

[51] B. W. Larson, K. A. Thurman, H. S. Kang, A. J. Ferguson, J. L. Blackburn, and M. Steger, "Arresting photodegradation in semiconducting single-walled carbon nanotube thin films," *ACS Applied Nano Materials*, vol. 5, no. 3, p. 3502–3511, Feb. 2022.

[52] N. Danné, M. Kim, A. G. Godin, H. Kwon, Z. Gao, X. Wu, N. F. Hartmann, S. K. Doorn, B. Lounis, Y. Wang, and L. Cognet, "Ultrashort carbon nanotubes that fluoresce brightly in the near-infrared," *ACS Nano*, vol. 12, no. 6, p. 6059–6065, Jun. 2018.

[53] F. J. Berger, J. Lüttgens, T. Nowack, T. Kutsch, S. Lindenthal, L. Kistner, C. C. Müller, L. M. Bongartz, V. A. Lumsargis, Y. Zakharko, and J. Zaumseil, "Brightening of long, polymer-wrapped carbon nanotubes by sp^3 functionalization in organic solvents," *ACS Nano*, vol. 13, no. 8, p. 9259–9269, Aug. 2019.

[54] A. Graf, M. Held, Y. Zakharko, L. Tropf, M. C. Gather, and J. Zaumseil, "Electrical pumping and tuning of exciton-polaritons in carbon nanotube microcavities," *Nature Materials*, vol. 16, no. 9, p. 911–917, Jul. 2017.

[55] R. W. Boyd, *Nonlinear Optics*, 4th ed. Academic Press, 2020.

[56] G. New, *Introduction to nonlinear optics*. Cambridge University Press, 2011.

[57] J. Wang, B. Gu, H.-T. Wang, and X.-W. Ni, "Z-scan analytical theory for material with saturable absorption and two-photon absorption," *Optics Communications*, vol. 283, no. 18, p. 3525–3528, Sep. 2010.

[58] P.-L. Thériault, W. Jiang, A. Dhavamani, L. Haeberlé, M. S. Arnold, M. Kira, and S. Kéna-Cohen, "Non-perturbative optical nonlinearities near the exciton resonance of single-chirality (6,5) carbon nanotube thin films," *(In preparation)*, 2025.

[59] C. Möhl, A. Graf, F. J. Berger, J. Lüttgens, Y. Zakharko, V. Lumsargis, M. C. Gather, and J. Zaumseil, "Trion-polariton formation in single-walled carbon nanotube microcavities," *ACS Photonics*, vol. 5, no. 6, p. 2074–2080, May 2018.

[60] W. Gao, X. Li, M. Bamba, and J. Kono, "Continuous transition between weak and ultrastrong coupling through exceptional points in carbon nanotube microcavity exciton–polaritons," *Nature Photonics*, vol. 12, no. 6, p. 362–367, Apr. 2018.

[61] J. M. Lüttgens, F. J. Berger, and J. Zaumseil, "Population of exciton–polaritons via luminescent sp^3 defects in single-walled carbon nanotubes," *ACS Photonics*, vol. 8, no. 1, p. 182–193, Dec. 2020.

[62] A. Dhavamani, "Photo-physics and engineering of semiconducting carbon nanotube polaritons for advanced optoelectronic devices," PhD thesis, University of Wisconsin-Madison, 2024.

[63] H. Ozawa, N. Ide, T. Fujigaya, Y. Niidome, and N. Nakashima, "One-pot separation of highly enriched (6,5)-single-walled carbon nanotubes using a fluorene-based copolymer," *Chemistry Letters*, vol. 40, pp. 239–241, 2011.

[64] P. Yeh, *Optical waves in layered media*, ser. Wiley Series in Pure and Applied Optics. Wiley-Blackwell, 2005.

[65] S. J. Byrnes, "Multilayer optical calculations," 2016.

[66] A. Graf, L. Tropf, Y. Zakharko, J. Zaumseil, and M. C. Gather, "Near-infrared exciton-polaritons in strongly coupled single-walled carbon nanotube microcavities," *Nature Communications*, vol. 7, no. 1, Oct 2016.

[67] J. Doumani, K. Zahn, J. Li, S. Yu, G. M. R. Barrios, S. Sasmal, R. Kikuchi, T. E. Kritzell, H. Xu, A. Baydin, and J. Kono, "Macroscopically self-aligned and chiralized carbon nanotubes: From filtration to innovation," pp. 10 718–10 737, 3 2025.

[68] J. A. Woollam Co., *CompleteEASE 6 Software Manual*, 2020.

[69] A. Ajami, A. Ovsianikov, R. Liska, and S. Baudis, "Z-scan technique: a review from conventional Z-scan to white light Z-scan," *Applied Physics B: Lasers and Optics*, vol. 130, 8 2024.

[70] B. Gu, W. Ji, and X.-Q. Huang, "Analytical expression for femtosecond-pulsed Z scans on instantaneous nonlinearity," *Applied Optics*, vol. 47, pp. 1187–1192, 2008.

[71] A. Frisk Kockum, A. Miranowicz, S. De Liberato, S. Savasta, and F. Nori, "Ultrastrong coupling between light and matter," *Nature Reviews Physics*, vol. 1, no. 1, p. 19–40, Jan. 2019.

[72] L. Valkunas, Y.-Z. Ma, and G. R. Fleming, "Exciton-exciton annihilation in single-walled carbon nanotubes," *Physical Review B*, vol. 73, no. 11, Mar. 2006.

[73] J. T. Flach, J. Wang, M. S. Arnold, and M. T. Zanni, "Providing time to transfer: Longer lifetimes lead to improved energy transfer in films of semiconducting carbon nanotubes," *Journal of Physical Chemistry Letters*, vol. 11, pp. 6016–6024, 8 2020.

[74] G. Delport, G. Chehade, F. Lédée, H. Diab, C. Milesi-Brault, G. Trippé-Allard, J. Even, J.-S. Lauret, E. Deleporte, and D. Garrot, "Exciton–exciton annihilation in two-dimensional halide perovskites at room temperature," *The Journal of Physical Chemistry Letters*, vol. 10, no. 17, p. 5153–5159, Aug. 2019.

[75] R. Taylor, R. Adams, J. Ryan, and R. Park, "Exciton recombination dynamics in ZnCdSe/ZnSe quantum wells," *Journal of Crystal Growth*, vol. 159, no. 1, pp. 822–825, 1996, proceedings of the seventh international conference on II-VI compouds and devices.

[76] D. Sun, Y. Rao, G. A. Reider, G. Chen, Y. You, L. Brézin, A. R. Harutyunyan, and T. F. Heinz, "Observation of rapid exciton–exciton annihilation in monolayer molybdenum disulfide," *Nano Letters*, vol. 14, no. 10, p. 5625–5629, Sep. 2014.

[77] A. M. Weiner, *Ultrafast Optics*. Wiley, 2009.

[78] A. Dubietis and A. Couairon, *Ultrafast Supercontinuum Generation in Transparent Solid-State Media*. Springer, 2019.

[79] M. Bradler, P. Baum, and E. Riedle, "Femtosecond continuum generation in bulk laser host materials with sub-μJ pump pulses," *Applied Physics B: Lasers and Optics*, vol. 97, pp. 561–574, 11 2009.

[80] Thorlabs Inc., *S122C Compact Photodiode Power Head with Germanium Detector - Specification Sheet*, 2021.

[81] A. Fieramosca, L. Polimeno, V. Ardizzone, L. D. Marco, M. Pugliese, V. Maiorano, M. D. Giorgi, L. Dominici, G. Gigli, D. Gerace, D. Ballarini, and D. Sanvitto, "Two-dimensional hybrid perovskites sustaining strong polariton interactions at room temperature," *Science Advances*, vol. 5, 2019.

[82] C. A. Delpo, B. Kudisch, K. H. Park, S. U. Z. Khan, F. Fassioli, D. Fausti, B. P. Rand, and G. D. Scholes, "Polariton transitions in femtosecond transient absorption studies of ultrastrong light-molecule coupling," *Journal of Physical Chemistry Letters*, vol. 11, pp. 2667–2674, 4 2020.

[83] N. Wickremasinghe, X. Wang, H. Schmitzer, and H. P. Wagner, "Eliminating thermal effects in Z-scan measurements of thin PTCDA films," *Optics Express*, vol. 22, p. 23955, 10 2014.

[84] A. Gnoli, L. Razzari, and M. Righini, "Z-scan measurements using high repetition rate lasers: how to manage thermal effects," *Optics Express*, vol. 13, pp. 7976–7981, 2005.

[85] X. Tian, S. Xiong, Y. Zhang, and K. Zhang, "Simulation of thermal stress in ion beam sputtered Ta_2O_5/SiO_2 multilayer coatings on different substrates by finite element analysis," *Surface and Coatings Technology*, vol. 362, pp. 225–233, 3 2019.

[86] SCHOTT North America Inc., *SCHOTT Optical Glass Datasheets : N-BK7*, 517642.251, 2010. [Online]. Available: https://www.us.schott.com/shop/medias/schott-optical-glass-collection-datasheets-english-us-march2018.pdf

[87] EMD Chemicals Inc., *Product information : Magnesium fluoride Patinal*, 2008. [Online]. Available: https://www.sigmaaldrich.com/deepweb/assets/sigmaaldrich/product/documents/352/060/mgf2-us-105849-1-10261-105823-105845-105834-105846-ms.pdf

[88] J. Brandrup, E. H. Immergut, and E. A. Grulke, *Polymer Handbook*, 4th ed. Wiley, 1998.

[89] A. D. Avery, B. H. Zhou, J. Lee, E. S. Lee, E. M. Miller, R. Ihly, D. Wesenberg, K. S. Mistry, S. L. Guillot, B. L. Zink, Y. H. Kim, J. L. Blackburn, and A. J. Ferguson, "Tailored semiconducting carbon nanotube networks with enhanced thermoelectric properties," *Nature Energy*, vol. 1, 2016.

[90] X. Zhang, W. Tan, F. Smail, M. D. Volder, N. Fleck, and A. Boies, "High-fidelity characterization on anisotropic thermal conductivity of carbon nanotube sheets and on their effects of thermal enhancement of nanocomposites," *Nanotechnology*, vol. 29, 7 2018.

[91] K. Suemori and T. Kamata, "Thermoelectric characteristics in out-of plane direction of thick carbon nanotube-polystyrene composites fabricated by the solution process," *Synthetic Metals*, vol. 227, pp. 177–181, 5 2017.

[92] L. Qiu, X. Wang, G. Su, D. Tang, X. Zheng, J. Zhu, Z. Wang, P. M. Norris, P. D. Bradford, and Y. Zhu, "Remarkably enhanced thermal transport based on a flexible horizontally-aligned carbon nanotube array film," *Scientific Reports*, vol. 6, 2 2016.

[93] N. R. Pradhan, H. Duan, J. Liang, and G. S. Iannacchione, "The specific heat and effective thermal conductivity of composites containing single-wall and multi-wall carbon nanotubes," *Nanotechnology*, vol. 20, 2009.

[94] L. G and L. L, *Carbon Nanotubes : Electronic Structure and Spectroscopy*. Academic Press, 2011, vol. 1.

[95] S. R. Sanchez, S. M. Bachilo, Y. Kadria-Vili, C. W. Lin, and R. B. Weisman, "(n,m)-specific absorption cross sections of single-walled carbon nanotubes measured by variance spectroscopy," *Nano Letters*, vol. 16, pp. 6903–6909, 11 2016.

[96] P. O. Morawska, Y. Wang, A. Ruseckas, C. Orofino-Penia, A. L. Kanibolotsky, R. Santhanagopal, N. Fröhlich, M. Fritsch, S. Allard, U. Scherf, P. J. Skabara, I. D. Samuel, and G. A. Turnbull, "Side-chain influence on the mass density and refractive index of polyfluorenes and star-shaped oligofluorene truxenes," *Journal of Physical Chemistry C*, vol. 119, pp. 22 102–22 107, 9 2015.

[97] Z. Zhang, P. Zhao, P. Lin, and F. Sun, "Thermo-optic coefficients of polymers for optical waveguide applications," *Polymer*, vol. 47, pp. 4893–4896, 6 2006.

[98] C.-C. Jaing, "Thermal expansion coefficients of obliquely deposited MgF_2 thin films and their intrinsic stress," *Applied Optics*, vol. 50, no. 9, p. C159, Dec. 2010.

[99] Alamusi, N. Hu, B. Jia, M. Arai, C. Yan, J. Li, Y. Liu, S. Atobe, and H. Fukunaga, "Prediction of thermal expansion properties of carbon nanotubes using molecular dynamics simulations," *Computational Materials Science*, vol. 54, pp. 249–254, 3 2012.

[100] H. Guo, T. V. Sreekumar, T. Liu, M. Minus, and S. Kumar, "Structure and properties of polyacrylonitrile/single wall carbon nanotube composite films," *Polymer*, vol. 46, pp. 3001–3005, 4 2005.

[101] Y. Xu, G. Ray, and B. Abdel-Magid, "Thermal behavior of single-walled carbon nanotube polymer-matrix composites," *Composites Part A: Applied Science and Manufacturing*, vol. 37, pp. 114–121, 1 2006.

[102] C. Dong, "Coefficient of thermal expansion of single-wall carbon nanotube reinforced nanocomposites," *Journal of Composites Science*, vol. 5, 2021.

[103] J. E. Toney, "Incorporation of nonlinearity and dispersion into time-dependent optical propagation models," in *Proceedings of the COMSOL Conference*, 2008.

[104] D. S. Bethune, "Optical harmonic generation and mixing in multilayer media : analysis using optical transfer matrix techniques," *JOSA B*, vol. 6, no. 5, p. 910, 1989.

[105] K. Sajnok and M. Matuszewski, "Modeling nonlinear exciton-polariton microcavities using the transfer-matrix method: Spontaneous symmetry breaking and self-focusing," *Physical Review A*, vol. 111, 5 2025.

[106] L. J. Prokopeva, J. D. Borneman, and A. V. Kildishev, "Optical dispersion models for time-domain modeling of metal-dielectric nanostructures," *IEEE Transactions on Magnetics*, vol. 47, pp. 1150–1153, 2011.

[107] V. Janyani, A. Vukovic, J. D. Paul, P. Sewell, and T. M. Benson, "Time domain simulation in photonics: A comparison of nonlinear dispersive polarisation models," *Optical and Quantum Electronics*, vol. 37, no. 1–3, p. 3–24, Jan. 2005.

[108] ——, "The development of TLM models for nonlinear optics," *Microwave Review*, pp. 35–42, 2004.

[109] Light Conversion UAB, 2025, private email correspondence.

[110] Thorlabs, 2025, private email correspondence.

[111] SCHOTT North America Inc., *SCHOTT Optical Glass Datasheets : N-LAK22*, 651559.377, 2016. [Online]. Available: https://www.us.schott.com/shop/medias/schott-optical-glass-collection-datasheets-english-us-march2018.pdf

[112] ——, *SCHOTT Optical Glass Datasheets : N-SF6*, 805254.337, 2016. [Online]. Available: https://www.us.schott.com/shop/medias/schott-optical-glass-collection-datasheets-english-us-march2018.pdf

[113] S. Yefet and A. Pe'er, "A review of cavity design for Kerr lens mode-locked solid-state lasers," *Applied Sciences*, vol. 3, pp. 694–724, 12 2013.

[114] X. Lu, J. Y. Lee, S. Rogers, and Q. Lin, "Optical Kerr nonlinearity in a high-Q silicon carbide microresonator," *Optics Express*, vol. 22, p. 30826, 12 2014.

[115] I. S. Maksymov, A. A. Sukhorukov, A. V. Lavrinenko, and Y. S. Kivshar, "Comparative study of FDTD-adopted numerical algorithms for Kerr nonlinearities," *IEEE Antennas and Wireless Propagation Letters*, vol. 10, pp. 143–146, 2011.

[116] R. Tao, K. Peng, L. Haeberlé, Q. Li, D. Jin, G. R. Fleming, S. Kéna-Cohen, X. Zhang, and W. Bao, "Halide perovskites enable polaritonic XY spin hamiltonian at room temperature," *Nature Materials*, vol. 21, no. 7, p. 761–766, Jun 2022.

[117] Y. Fu, H. Zhu, J. Chen, M. P. Hautzinger, X. Y. Zhu, and S. Jin, "Metal halide perovskite nanostructures for optoelectronic applications and the study of physical properties," pp. 169–188, 3 2019.

[118] B. R. Sutherland and E. H. Sargent, "Perovskite photonic sources," pp. 295–302, 5 2016.

[119] R. Su, A. Fieramosca, Q. Zhang, H. S. Nguyen, E. Deleporte, Z. Chen, D. Sanvitto, T. C. Liew, and Q. Xiong, "Perovskite semiconductors for room-temperature exciton-polaritonics," pp. 1315–1324, 10 2021.

[120] T. Wang, Z. Zang, Y. Gao, C. Lyu, P. Gu, Y. Yao, K. Peng, K. Watanabe, T. Taniguchi, X. Liu, Y. Gao, W. Bao, and Y. Ye, "Electrically pumped polarized exciton-polaritons in a halide perovskite microcavity," *Nano Letters*, vol. 22, pp. 5175–5181, 7 2022.

[121] R. Su, J. Wang, J. Zhao, J. Xing, W. Zhao, C. Diederichs, T. C. H. Liew, and Q. Xiong, "Room temperature long-range coherent exciton polariton condensate flow in lead halide perovskites," *Science Advances*, vol. 4, no. 10, Oct. 2018.

[122] R. Su, C. Diederichs, J. Wang, T. C. Liew, J. Zhao, S. Liu, W. Xu, Z. Chen, and Q. Xiong, "Room-temperature polariton lasing in all-inorganic perovskite nanoplatelets," *Nano Letters*, vol. 17, pp. 3982–3988, 6 2017.

[123] M. Wouters and I. Carusotto, "Parametric oscillation threshold of semiconductor microcavities in the strong coupling regime," *Physical Review B*, vol. 75, no. 7, Feb 2007.

APPENDIX A ALIGNMENT AND CALIBRATION OF THE ANGLE-RESOLVED SPECTROSCOPY SETUP

This is intended as a reference for future users of the angle-resolved micro-spectroscopy setup.

Alignment and focusing

Focus and tilt of the camera

1. Select the correct grating on the spectrometer (the same that will be used in the measurement). Set the wavelength to 0nm.
2. Close the slit to 30um width.
3. Install a scattering target in the microscope sample holder (600 grit ground glass diffuser, piece of Teflon sheet, white paper, etc).
4. Switch the microscope imaging path to the eyepiece.
5. Using grazing angle illumination from below (ex. OSL2 halogen lamp), focus on the target surface with a low-magnification objective.
6. Illuminate the target from above with OSL2 lamp or other bright white light source.
7. Switch the microscope imaging path to the side port.
8. Now, the field of view of the objective (containing a flat uniform bright field) should be focused on the spectrometer entrance slit by the L1/L3 relay.
9. Looking at the live feed from the camera, adjust the focus to get the sharpest possible image of the slit, and the tilt to align the slit image on the vertical axis.
10. Lock the camera in place. The alignment will shift a bit when tightening the screw, you will need to adjust the initial position so the tilt and focus are good once locked.
11. Note the slit position X_0 on the sensor. The field on view of the microscope will be aligned to center on this position. Note : this will not be the same as the center of the sensor (i.e. $X_0 = 320$ for a 640px wide sensor) because of the camera mount mechanical tolerances.

Alignment and focus of L3 ($f = 300$ mm achromatic doublet)

Focus

Using a ruler, make sure the distance between the lens back flange and the plane of the spectrometer slit (at the center of the micrometer screw) corresponds to the back focal length of the AC508-300-C-ML lens ($f_b = 291.3$ mm). See the reference drawing on the Thorlabs website for the correct measurement location on the lens. Make sure to use a spacer or other means to keep the ruler horizontal and avoid parallax error. Aim for an accuracy of 1mm or better.

Alignment, XY position

1. Remove lens L1 from the path.
2. Place a reticle alignment target (ex. R1DS2P) in the microscope sample holder and illuminate from above.
3. Switch the microscope imaging path to the eyepiece.
4. Center the target reticle on the eyepiece reticle and focus the image.
5. Switch the microscope imaging path to the side port.
6. Place a LMR2AP alignment plate on L3. Adjust the lens XY position to center the projected reticle image on the center of the alignment plate.

Alignment, tilt

1. Install a beam block before the spectrometer.
2. Set up an alignment laser collinear with the microscope optical axis.
3. Install a SM1-threaded iris on the microscope side port.
4. Adjust the tilt of L3 to align the back-reflected spot from L3 on the iris.

During normal operation, L3 is never moved, and minor adjustments in the image position or focus are done with L1.

Alignment and focus of L1 ($f = 100$ mm biconvex)

Coarse alignment, XY position

Follow the same procedure as for XY alignment of L3, using the LMR2AP alignment plate of L1.

Coarse focusing

1. Follow steps 1-5 of the XY focusing of the L3 lens.
2. Looking at the live image on the camera, adjust the Z-position of L1 until the image of the alignment target reticle is sharp.

Alignment, tilt

Follow the same procedure as for tilt alignment of L3, using the back-reflected spot from L1.

Any polarizers or filters between L1 and L3 can slightly shift the image position or focus. The fine alignment should be performed with the same optics in the path as what will be used in the measurement.

Fine alignment, X

1. Set up the alignment reticle in the microscope sample holder.
2. Looking at the live feed from the camera, adjust the L1 X-position until the reticle is centered on the position of the slit (position recorded during initial camera alignment).

L1 is not an achromatic lens. To ensure correct focus, the L1 Z-position must be adjusted while illuminated with approximately the same wavelength range as what will be used during the experiment.

Fine focusing

1. Insert the appropriate bandpass filters in the illumination light path.
2. Looking at the live field from the camera, adjust L1 Z position until the image of the target reticle is sharp.
3. Note the Y_0 position of the center of the alignment target reticle.

While the X-center of the camera field of view can be accurately defined (at the slit X-position), there is no similar obvious feature to locate the Y-center of the field of view. It is not coincident with the Y-center of the sensor (i.e. Y=256 for a 512px-height sensor), because of the mechanical tolerances of the camera spectrometer mount. From experience, when trying to align the center of the field of view with the sensor Y-center, the L1 lens becomes significantly offset from the microscope field of view, and the image is distorted. The coarse Y-alignment using the LMR2AP alignment plate is sufficient to obtain a real-space image free of distortions.

Alignment and focus of L2 ($f = 100$ mm achromatic doublet)

Coarse alignment, XY position and tilt

1. Follow steps 1-3 of the tilt alignment of L1 and L3.
2. Place a LMR2AP alignment plate on L2. Adjust L2 XY position until the alignment laser spot is centered on the plate.
3. Remove the alignment plate and adjust the tilt of L2 to center the back-reflected spot on the iris.
4. Repeat the previous two steps until both position and tilt are correct.

Fine alignment and focusing

1. Mount a sample that emits approximately isotropic light at the measurement wavelength (for example, a fluorescent thin film) and set up the appropriate optical pump.

2. Looking at the live field from the camera, adjust L2 Z position until the image of the Fourier plane (which should be a uniform filled circle) is sharp.

3. Adjust L2 XY position until the Fourier plane is centered on the same X_0, Y_0 position as the real-space image.

Calibration

Wavelength calibration

Wavelength calibration is performed using a standard procedure, measuring the spectrum from a spectral calibration source (Oriel 6031 Kr lamp, Oriel 6032 Ne lamp) at different grating positions and fitting the measured peak position to reference spectral lines from the NIST database. For optimal resolution of the spectral lines, the lamp is placed at the Fourier plane between L1 and L2, such that a sharp image of the lamp is projected on the spectrometer entrance slit.

Fourier plane scale calibration

The position $\mathbf{r}_F$ on the Fourier plane is proportional to the in-plane wavevector scaled by a magnification factor M_k depending of the focal lengths of the microscope objective, microscope tube lens, and L1, L2, L3 :

$$\mathbf{r}_F = M_k \mathbf{k}_{\|}$$

In practice, due to the cropping of the Fourier plane by the spectrometer entrance slit (oriented along the y direction), only the k_y component is measured.

$$y_F = M_k k_y = M_k sin\theta_y$$

Calibration of the Fourier plane magnification measures $M_k(\mathbf{r}_F)$ in order to correct for any aberrations in Fourier imaging.

1. Set up an alignment laser collinear with the microscope optical axis. The power should be suitably attenuated to avoid damaging the camera, and the wavelength should be close to the wavelength used in actual measurements to avoid errors in magnification from chromatic aberration.

2. Mount a low-period transmission grating in the microscope sample holder (150 lines/mm works well).

3. Looking at the live field from the camera, rotate the grating until the line of bright spots from the different diffraction orders is vertical (aligned with a column of pixels on the camera).

4. Record the measured diffraction pattern.

The θ_y of the diffraction orders for a given wavelength is easily calculated from the grating equation, and the measured y_F position can be fitted to the calculated k_y with a polynomial function for M_k. in practice, a second-order polynomial is sufficient for a perfect fit, with the quadratic coefficient being a small correction three orders of magnitude smaller than the dominant linear coefficient.

APPENDIX B LIST OF EQUIPMENT AND INSTRUMENTS

Instruments

- First Light Imaging CRED-2 InGaAs Cooled-sensor SWIR camera
- Princeton Instruments ISOPLANE 160 imaging spectrometer
- Thorlabs PM100D power meter
- Thorlabs S120C power sensor (Si photodiode)
- Thorlabs S122C power sensor (Ge photodiode)
- Thorlabs S401C power sensor (Thermopile)

Equipment

- Olympus IX81 Inverted Microscope
- Thorlabs OSL2 fiber-coupled halogen light source (illumination for BF/DF imaging)
- Thorlabs SLS201L stabilized fiber-coupled light source (CW reflectance measurements)
- Thorlabs CPS532 (532nm, 5mW laser diode, pump for CW PL measurements)
- Thorlabs L808P200 (808nm, 200mW laser diode, pump for CW PL measurements)
- Thorlabs SH1/KSC101 (Solenoid beam shutter and controller)
- Light Conversion PHAROS (femtosecond laser, 100kHz, 290fs, 1030nm)
- Light Conversion ORPHEUS-F (tunable optical parametric amplifier)
- Advanced Research Systems DE-204S closed-cycle helium cryostat

Optics

Optics are from Thorlabs unless indicated otherwise.

- Olympus LCPlan N 50X/0.65IR (Infrared objective)
- BSW26R (beamsplitter for reflectance measurements)
- Edmund optics 69-901 (600nm dichroic longpass for PL measurements)
- FELH0850 (longpass in Fourier optics)
- LB1630 bi-convex lens f=100mm (L1 in Fourier optics)
- AC508-150-C-ML infrared achromatic doublet f=150mm (L2 in Fourier optics)
- AC503-300-C-ML infrared achromatic doublet f=300mm (L3 in Fourier optics)
- LPNIR100-MP2 (linear polarizer in detection optics)
- NDC-50C-4 (Variable reflective neutral-density filter, SC pump attenuation)
- NDC-50C-4 (Variable reflective neutral-density filter, SC attenuation. Mounted on servo rotation stage.)
- AC254-100-B-ML (pump focusing into YAG crystal)
- Light Conversion NM1b (5mm YAG crystal for supercontinuum generation)
- AC254-035-C-ML (supercontinuum collimation)
- BSW29 (600-1700nm 50:50 beampsplitter, separates the SC probe/reference beams)
- FELH1050 (1050nm longpass)
- Edmund Optics 89-669 (1150nm shortpass)
- Edmund Optics 39-051 (achromatic half waveplate)
- Olympus LUCPlanFL N 20X/0.45 (objective for focusing SC probe on sample)